TESLA 2001-33
September 2001

Monopole, Dipole and Quadrupole Passbands of the TESLA 9-cell Cavity

R. Wanzenberg

DESY, Notkestr. 85, 22603 Hamburg, Germany

September 14, 2001

Abstract

The passband structure of the TESLA 1.3 GHz cavity is investigated for monopole, dipole and quadrupole modes. The dispersion curves are obtained for one cavity mid-cell using periodic boundary conditions. The basic rf-parameters of the higher order modes (HOMs) are calculated for several 9-cell cavity structures. The modes in 9-cell structures are related to the passband structure of a cavity mid-cell. In particular, the properties of dipole modes above the cut-off frequency of the beam pipe are discussed. Extensive graphical representations of the HOMs are provided. All numerical calculations are performed with the computer code MAFIA. The data obtained are intended to be used in further beam dynamics studies in the TESLA linac and in the interpretation of HOM measurements at the TESLA Test Facility.

Contents

1 Introduction

Long range wakefields are important for the beam dynamics of a long train of bunches in the TESLA main linear accelerator since these wakefields can cause multibunch instabilities. The long range wakepotential can be represented as a sum over contributions from Higher Order Modes (HOMs). This report will summarize the properties of the lowest monopole, dipole and quadrupole HOM passbands of the TESLA 9-cell cavity. Field plots of several modes are provided to visualize the properties of the different types of modes. Fig. 1 shows one 9-cell superconducting cavity of the TESLA Test Facility (TTF). The fundamental mode is a 1.3 GHz π-mode, which is used to accelerate the beam. A detailed review of the TESLA cavity design is presented in [1].

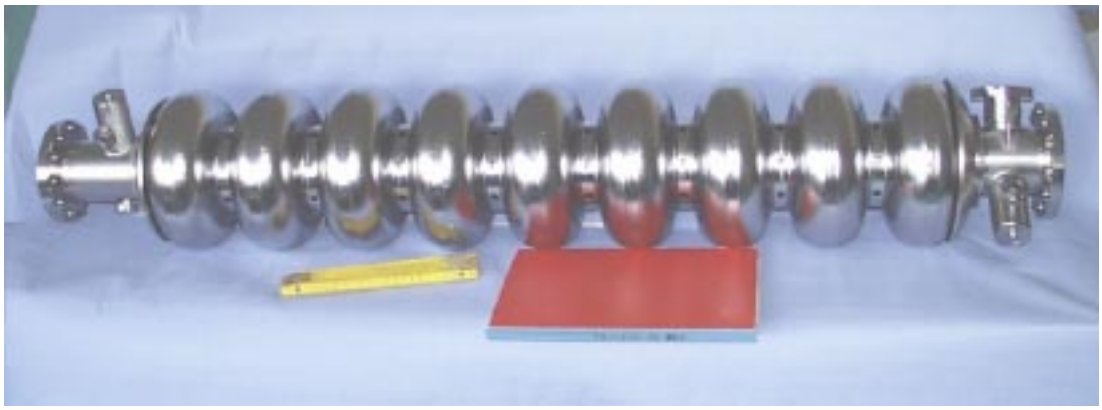

Figure 1: Superconducting TESLA 9-cell cavity.

At the TESLA Test Facility eight cavities are grouped together in one cryostat. The distance between the cavities is $3\,\lambda/2$ or 346.2 mm, where the wave length λ of the fundamental 1.3 GHz mode is 230.8 mm. The Technical Design Report (TDR) [2] of a 2×250 GeV linear accelerator is based on a slightly different design with a shorter spacing (283 mm) between cavities in order to increase the fill factor, i.e. the ratio of active length to total length of the linac. Furthermore two types of superstructures with further reduced cavity spacing are discussed as options in [2, p. II-47]. The superstructure II is a combination of two 9-cell resonators joined by a 114 mm diameter beam pipe with a length of 115.3 mm. Two TESLA 9-cell cavity-halves separated by a distance of $2\,\lambda/2 + 30\,\mathrm{mm} = 260.8\,\mathrm{mm}$, which differs by about 20 mm from the TDR design baseline, are shown in Fig. 2. This cavity arrangement is the standard configuration for the calculation of monopole, dipole and quadrupole mode used throughout this report and is referred to as the TESLA TDR-like 9-cell cavity. Additionally the TTF cavity configuration with a $3\,\lambda/2$ spacing is considered in the section covering dipole modes since several measurements have recently been performed with this cavity arrangement at the test facility [3, 4]. The cavity arrangement at the test facility will be called the

TESLA TTF 9-cell cavity. The shapes of individual cells are the same for the TDR-like and TTF 9-cell cavities. A schematic sketch of a cavity cell is shown in Fig. 3. Each cell is rotationally symmetric around the z-axis. The iris has an elliptical shape, and the equator a circular shape in the r, z-plane.

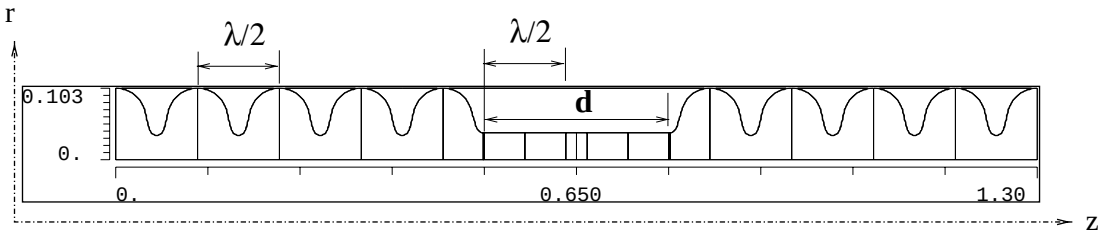

Figure 2: Two halves of a TESLA cavity. The distance d between the cavities is $\lambda + 30$ mm or 260.8 mm corresponding to the TDR-like version of the cavity.

There are three different half cell shapes: a mid-cell and two end-cup geometries. The parameters are listed in table 1. The end-cups are slightly shorter

	midcup	end-cup 1	end-cup 2
iris radius a /mm	35.0	39.0	39.0
equator radius b /mm	103.3	103.3	103.3
half cell length h /mm	57.7	56.0	57.0
curvature at			
equator r_e/mm	42.0	40.3	42.0
iris - horz. axis r_{iz}/mm	12.0	10.0	9.0
- vert. axis r_{ir}/mm	19.0	13.5	12.8

Table 1: Geometric parameters of three cup shapes of a TESLA cavity.

than the mid-cup. Please note that the distance d in Fig. 2 is the distance between cells with a cell lengths of $\lambda/2 = 115.4$ mm, i.e. the end-cell consists of an end-cup and a very short beam pipe such that the length of the end-cell is equal to that of one mid-cell. Only symmetric cavities (with end-cup 1) are considered in this report.

The computer code MAFIA [5, 6] is used to calculate the electric and magnetic fields in the frequency domain. Fig. 4 shows the electric field of the 1.3 GHz accelerating mode in the TESLA cavity. The cavity has been modeled in an $r\varphi z$-grid to provide a 3-dimensional visualization of the electric field. A 2-dimensional model of the cavity is used in most of this report since it is sufficient to model a cylindrically symmetric cavity on a rz-grid to obtain the important rf-parameters. Nevertheless it is informative to visualize the electric field on a 3-dimensional grid. This is done in Fig. 5, 6, and 7 for the monopole, dipole and quadrupole π-modes of the lowest frequency. The electric field of the accelerating mode in a one cavity cell is shown in Fig. 5. Electric (E) boundary conditions are used at both ends

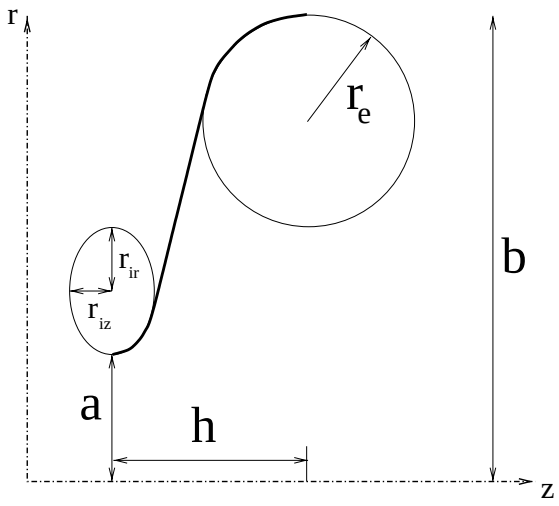

Figure 3: Schematic sketch of the geometry of a cell of a TESLA cavity.

of the modeled structure. The electric field is therefore perpendicular to the cell mid-plane as shown in the left graph of Fig. 5. The phase advance form the right to the left cell mid-plane is π.

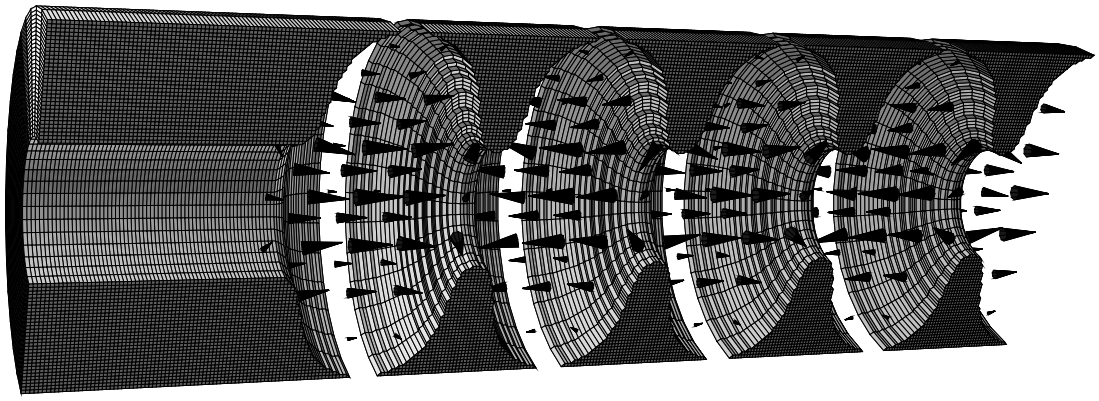

Figure 4: One half of a TESLA TDR-like 9-cell cavity. The electric field of the 1.3 GHz accelerating π-mode is shown. See also Fig. 5.

The electric field of the π-mode of the lowest dipole passband (with frequency 1.79 GHz) is shown in Fig. 6. Again electric boundary conditions are used at the left and right cell mid-planes. The $\cos(\phi)$-dependence of the electric field is clearly visualized with the help of the left graph of Fig. 6. The electric field is zero on the cavity axis. A particle beam can only interact with this mode if the beam transverses the structure off-axis.

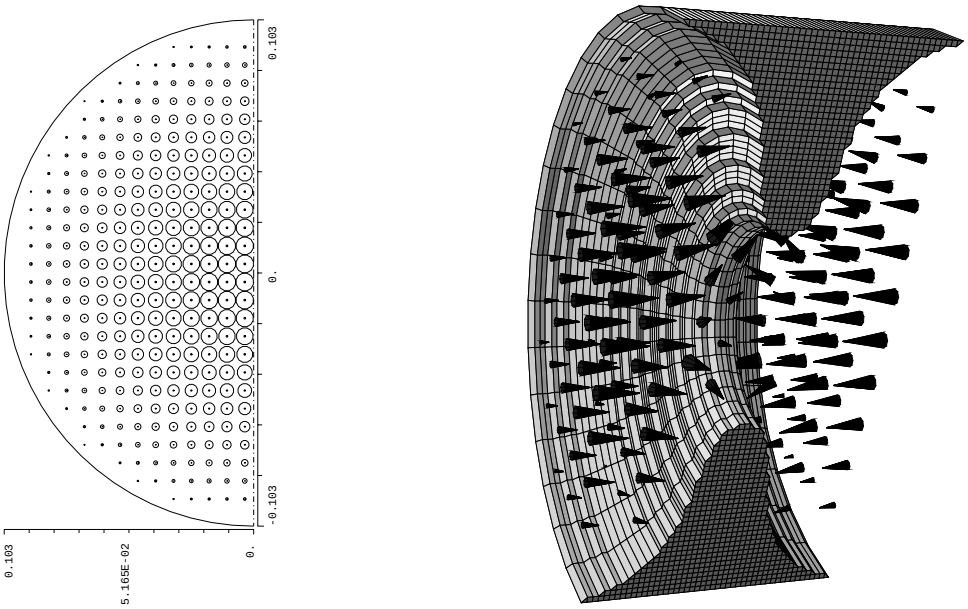

Figure 5: One mid-cell of a TESLA cavity. The electric field of the 1.3 GHz accelerating π-mode is shown. The left graph shows the electric field in a plane perpendicular to the cavity axis.

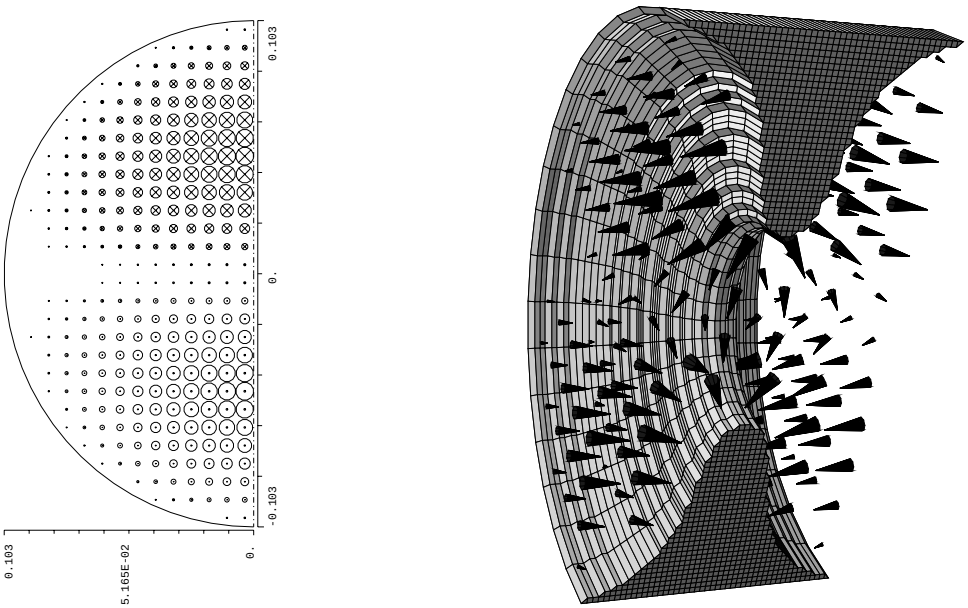

Figure 6: One mid-cell of a TESLA cavity. The electric field of the 1.79 GHz π-mode of the first dipole passband is shown. The left graph shows the electric field in a plane perpendicular to the cavity axis.

This is also true for quadrupole modes. The π-mode (with frequency 2.32 GHz) of the lowest quadrupole passband is shown in Fig. 7. This mode is obtained if magnetic boundary (M) conditions are used at the left and right cell mid-planes, i.e. there are only transverse electric field components in the left and right cell mid-planes. The left graph of Fig. 7 shows these field components. The azimuthal $\cos(2\,\phi)$-dependence of the quadrupole mode can also be seen in that graph.

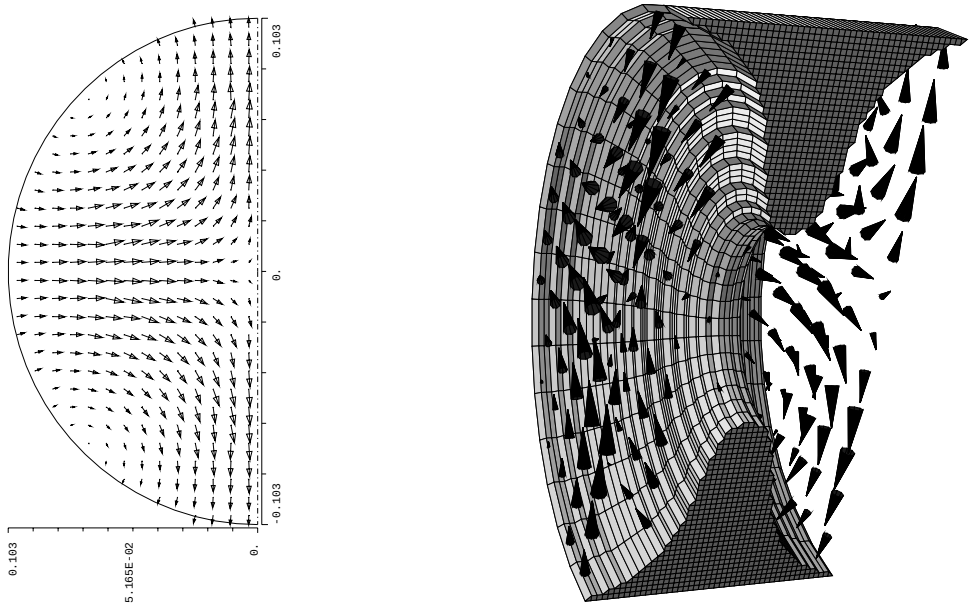

Figure 7: One mid-cell of a TESLA cavity. The electric field of the 2.32 GHz π-mode of the first quadrupole passband is shown. The left graph shows the electric field in a plane perpendicular to the cavity axis.

The definitions of the rf-parameters of the modes which are used within this report are explained in the next section. It is also described how the effect on the beam can be calculated from these parameters. The dispersion curves of monopole, dipole and quadrupole modes are investigated in section 3. In the following three sections the monopole, dipole and quadrupole modes in 9-cell cavities are covered separately. Most attention is paid to the dipole modes where several different cavity configurations are considered. Extensive graphical representation of the HOMs can be found in the appendices.

2 Basic Definitions of RF-parameters

The purpose of this section is to define the parameters including R/Q and G_1, which are used in the next sections. For dipole and quadrupole modes it is important to clarify the definitions used since there exist no unified standard in the literature. First it is explained which parameters can be obtained from the eigenmodes calculated by the computer code MAFIA [5, 6]. Then it is explained how effects on the beam can be calculated from these parameters.

2.1 Modes in a cavity

Consider any mode in a cavity with the frequency $f = \omega/(2\,\pi)$. One obtains in complex notation for the electric and magnetic field:

$$\begin{aligned} \boldsymbol{E}\,(r,\phi,z,t) &= \widetilde{\boldsymbol{E}}\,(r,\phi,z)\,\exp(-i\,\omega\,t) \\ \boldsymbol{B}\,(r,\phi,z,t) &= \widetilde{\boldsymbol{B}}\,(r,\phi,z)\,\exp(-i\,\omega\,t). \end{aligned} \tag{1}$$

Generally the fields $\widetilde{\boldsymbol{E}}\,(r,\phi,z)$ and $\widetilde{\boldsymbol{B}}\,(r,\phi,z)$ in geometries with cylindrical symmetry can be written as (in a multi-pole expansion) [7] :

$$\begin{aligned} \widetilde{\boldsymbol{E}}\,(r,\phi,z) &= \sum_m \Big(\widetilde{E_r^{(m)}}(r,z)\,\cos(m\,\phi) \quad \boldsymbol{e_r} \\ &\quad + \widetilde{E_\phi^{(m)}}(r,z)\,\sin(m\,\phi) \quad \boldsymbol{e_\phi} \\ &\quad + \widetilde{E_z^{(m)}}(r,z)\,\cos(m\,\phi) \quad \boldsymbol{e_z} \Big) \\ \widetilde{\boldsymbol{B}}\,(r,\phi,z) &= \sum_m \Big(\widetilde{B_r^{(m)}}(r,z)\,\sin(m\,\phi) \quad \boldsymbol{e_r} \\ &\quad + \widetilde{B_\phi^{(m)}}(r,z)\,\cos(m\,\phi) \quad \boldsymbol{e_\phi} \\ &\quad + \widetilde{B_z^{(m)}}(r,z)\,\sin(m\,\phi) \quad \boldsymbol{e_z} \Big). \end{aligned} \tag{2}$$

For the TESLA cavity the computer code MAFIA [5, 6] has been used to calculate the field components $\widetilde{E_r^{(m)}}$, $\widetilde{E_\phi^{(m)}}$, etc. The results are presented in the next sections for $m = 0, 1$ and 2 (the monopole, dipole, quadrupole modes).

In the plane $\phi = 0$ only longitudinal and radial electric field and azimuthal magnetic field components are present:

$$\begin{aligned} \widetilde{\boldsymbol{E}}\,(r,0,z) &= \sum_m \Big(\widetilde{E_r^{(m)}}(r,z) \quad \boldsymbol{e_r} \\ &\quad + \widetilde{E_z^{(m)}}(r,z) \quad \boldsymbol{e_z} \Big) \\ \widetilde{\boldsymbol{B}}\,(r,0,z) &= \sum_m \Big(\widetilde{B_\phi^{(m)}}(r,z) \quad \boldsymbol{e_\phi} \Big). \end{aligned} \tag{3}$$

The magnetic field can be calculated from the electric one according to the Maxwell equation:

$$\boldsymbol{\nabla} \times \widetilde{\boldsymbol{E}}(r,\phi,z) = i\,\omega\,\widetilde{\boldsymbol{B}}(r,\phi,z).$$

The azimuthal magnetic field component is given simply by:

$$\widetilde{B_\phi^{(m)}}(r,z) = \frac{-i}{\omega}\left(\frac{\partial}{\partial z}\widetilde{E_r^{(m)}}(r,z) - \frac{\partial}{\partial r}\widetilde{E_z^{(m)}}(r,z)\right). \tag{4}$$

The azimuthal component of the electric field is also related to the radial and longitudinal components of the electric field since the Maxwell equation $\boldsymbol{\nabla} \cdot \widetilde{\boldsymbol{E}}(r,\phi,z) = 0$ holds for all modes. For $m = 0$ the azimuthal component of the electric field is identical to zero, while for $m > 0$ one obtains:

$$\widetilde{E_\phi^{(m)}}(r,z) = -\frac{1}{m}\left[\widetilde{E_r^{(m)}}(r,z) + r\,\left(\frac{\partial}{\partial r}\widetilde{E_r^{(m)}}(r,z) + \frac{\partial}{\partial z}\widetilde{E_z^{(m)}}(r,z)\right)\right]. \tag{5}$$

Therefore it is sufficient to know the electric field in the plane $\phi = 0$, i.e. once the components $\widetilde{E_r^{(m)}}(r,z)$ and $\widetilde{E_z^{(m)}}(r,z)$ are know it is possible to reconstruct the complete electric and magnetic field pattern of the considered mode. The next sections contain Figures which show arrow-plots of the electric field always in the plane $\phi = 0$. These plots contain the complete information of the electric and magnetic field of the mode since all other field components provide only redundant information. Plots of the radial and longitudinal fields $\widetilde{E_r^{(m)}}(r_0,z)$ and $\widetilde{E_z^{(m)}}(r_0,z)$ for a fixed radius $r = r_0$ as a function of z are also shown.

2.1.1 The loss parameter and R/Q

The interaction of the beam with a cavity mode is characterized by the loss parameter $k_\parallel^{(m)}$ or by the quantity R/Q [8]. These parameters can be determinated from the numerically calculated fields using the MAFIA post-processor [5, 6]. The longitudinal voltage at a fixed radius r is defined as

$$V_\parallel^{(m)}(r) = \int_0^L dz\; \widetilde{E_z^{(m)}}(r,z)\exp(-i\,\omega\,z/c), \tag{6}$$

while the total stored energy of the considered mode is given by:

$$U^{(m)} = \frac{\epsilon_0}{2}\int d^3r\;\left|\widetilde{\boldsymbol{E}^{(m)}}\right|^2. \tag{7}$$

From the voltage and stored energy the loss parameter and R/Q can be calculated:

$$k^{(m)}(r) \;=\; \frac{\left|V_L^{(m)}(r)\right|^2}{4\,U^{(m)}}$$

(8)

$$\frac{R^{(m)}}{Q} = \frac{1}{r^{2\,m}} \frac{2\; k^{(m)}(r)}{\omega}.$$

For monopole modes the superscript (0) is usually omitted $R/Q = R^{(0)}/Q$. $R^{(m)}/Q$ is independent of the radius r since it can be shown (see [8, 9]) that $V^{(m)}(r) \sim r^m$ and therefore $k^{(m)}(r) \sim r^{2\,m}$.

2.1.2 The geometry parameter G_1 and the Q-value

The power P_{sur} dissipated into the cavity wall due to the surface resistivity R_{sur} can be calculated from the tangential magnetic field:

$$P_{sur} = \frac{1}{2}\; R_{sur} \int dA\, |H_\phi|^2\,. \tag{9}$$

For a superconducting cavity the surface resistance is the sum of the BCS (Bardeen, Cooper, Schrieffer) resistance R_{BCS}, which depends on the frequency and the temperature, and a residual resistivity R_{res}.

The power dissipated into the cavity surface can also be characterized by the quality factor Q_0 or the geometry parameter G_1 [11], which are defined as:

$$Q_0 = \frac{\omega\; U}{P_{sur}} \tag{10}$$

$$G_1 = R_{sur}\; Q_0, \tag{11}$$

where U is the total field energy and $\omega = 2\pi\, f$ is the frequency of the mode. G_1 is a purely geometric quantity which is independent of the cavity material. Therefore G_1 will be quoted throughout this report for the different cavity modes.

In the MAFIA post-processor the dissipated power P_{sur} is calculated by default for a copper cavity with the surface resistivity:

$$R_{Cu} = \sqrt{\frac{\omega\; \mu_0}{2\; \sigma_{Cu}}}, \qquad \sigma_{Cu} = 5.8 \cdot 10^7\; (\Omega\,\mathrm{m})^{-1}. \tag{12}$$

From the quality factor for copper and R_{Cu} the parameter G_1 can be obtained.

The BCS resistance R_{BCS} scales with the frequency f and temperature T as:

$$R_{BCS}(f,T) \sim \frac{f^2}{T}\; \exp(-1.76\, T_c/T). \tag{13}$$

Let $Q_{0,FM}$,$G_{1,FM}$ and f_{FM} be the Q-value, geometry parameter and the frequency of the fundamental (accelerating) mode of the cavity. Assuming that the wall

losses are dominated by the BCS resistance R_{BCS} the Q-value of any other mode with geometry parameter G_1 and frequency f is given by:

$$Q_0 = \frac{G_1}{G_{1,FM}} \left(\frac{f_{FM}}{f} \right)^2 Q_{0,FM}. \tag{14}$$

Therefore the scaling factor for Q_0-values is $(G_1/G_{1,FM})\ (f_{FM}/f)^2$.

The total damping of a cavity mode is not only determined by the surface losses but also by coupling to external waveguides (HOM-dampers). Therefore one has to distinguish the Q-value Q_0 which is defined above and the external Q-value Q_{ext} which characterizes the coupling to external waveguides.

2.2 Long Range Wakefields

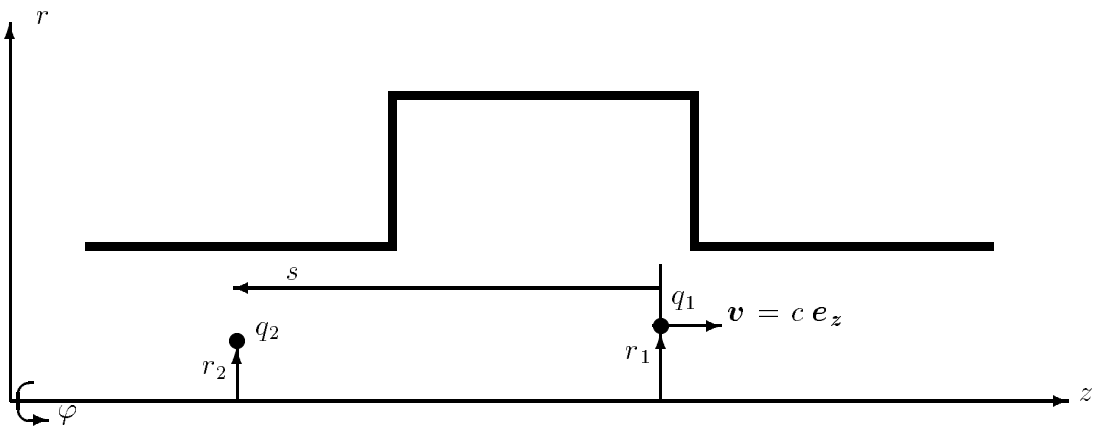

Figure 8: A point charge q_1 traversing a cavity with an offset r_1 followed by a test charge q_2 with offset r_2 .

Consider the situation shown in Fig. 8. A test charge q_2 follows a point charge q_1 at a distant s. It is assumed that both charges are relativistic ($v \approx c$). The Lorentz force on the test charge due to the fields generated by the point charge q_1 is

$$\boldsymbol{F} = \frac{d\boldsymbol{p}}{dt} = q_2\,(\boldsymbol{E} + c\,\boldsymbol{e_z} \times \boldsymbol{B}). \tag{15}$$

The **wake potential** of the point charge q_1 is defined as:

$$\boldsymbol{W}(x_2, y_2, x_1, y_1, s) = \frac{1}{q_1} \int_0^L dz (\boldsymbol{E} + c\,\boldsymbol{e_z} \times \boldsymbol{B})_{t=(z+s)/c}. \tag{16}$$

The wake potential may be regarded as an average of the Lorentz force on a test charge. Causality requires $\boldsymbol{W}(s) = 0$ for $s < 0$. The distant s is positive in the direction opposite to the motion of the point charge q_1.

The longitudinal and transverse components of the wake potential are connected by the Panofsky–Wenzel theorem [10]

$$\frac{\partial}{\partial s}\boldsymbol{W}_{\perp}(x_2, y_2, x_1, y_1, s) = -\boldsymbol{\nabla}_{\perp_2} W_{\parallel}(x_2, y_2, x_1, y_1, s). \tag{17}$$

Integration of the transverse gradient (applied to the transverse coordinates of the test charge) of the longitudinal wake potential yields the transverse wake potential.

2.2.1 Multipole expansion of the wake potential

If the structure traversed by the bunch is cylindrically symmetric then a multipole expansion can be used to describe the wake potential. Consider again the situation shown in Fig. 8. Assume that the point charge q_1 traverses the cavity at position (r_1, φ_1), while the test charge follows at position (r_2, φ_2). The longitudinal wake potential is given by:

$$W_{\parallel}(r_1, r_2, \varphi_1, \varphi_2, s) = \sum_{m=0}^{\infty} {r_1}^m \, {r_2}^m \; W_{\parallel}^{(m)}(s) \; \cos m\,(\varphi_2 - \varphi_1). \tag{18}$$

There is no a priori relation between the wake potentials of different azimuthal order m. The functions $W_{\parallel}^{(m)}(s)$ are the longitudinal m-pole wake potentials. It is often sufficient to consider only the leading terms of the series in equation (18), neglecting contributions from sextupole and higher multipole components. In Cartesian coordinates the longitudinal wake potential is approximately:

$$\begin{aligned} W_{\parallel}(x_1, y_1, x_2, y_2, s) \;\approx\; & W_{\parallel}^{(0)}(s) \\ & + (x_2\; x_1 + y_2\; y_1)\; W_{\parallel}^{(1)}(s) \\ & + \left((x_2{}^2 - y_2{}^2)\,(x_1{}^2 - y_1{}^2) + 2\,x_2\,y_2\;2\,x_1\,y_1\right)\; W_{\parallel}^{(2)}(s). \end{aligned} \tag{19}$$

The transverse wake potential can be calculated using the Panofsky–Wenzel theorem:

$$\begin{aligned} \boldsymbol{W}_{\perp}(x_1, y_1, x_2, y_2, s) \;\approx\; & (x_1\; \boldsymbol{e_x} + y_1\; \boldsymbol{e_y})\; W_{\parallel}^{(1)}(s) \\ & + (x_2\; \boldsymbol{e_x} - y_2\; \boldsymbol{e_y})\; 2\; (x_1{}^2 - y_1{}^2)\; W_{\parallel}^{(2)}(s) \\ & + (y_2\; \boldsymbol{e_x} + x_2\; \boldsymbol{e_y}) 2\; (2\,x_1\,y_1)\; W_{\parallel}^{(2)}(s). \end{aligned} \tag{20}$$

The transverse m-pole wake potentials are defined as:

$$W_{\perp}^{(m)}(s) = -\int_{-\infty}^{s} ds'\, W_{\parallel}^{(m)}(s'), \tag{21}$$

for $m > 0$. There is no transverse monopole wake potential. The dipole wake potential does not depend on the position of the test charge q_2. The kick on

the test charge is linear in the offset of the point charge q_1. The quadrupole wake potential depends linearly on the position of the test charge q_2 and on the quadrupole and skew quadrupole moment of the charge q_1, which generates the fields.

2.2.2 Wakefields due to HOMs

If only the long range wake fields are considered then it is possible to calculate the m-pole wake potentials $W_{\parallel}^{(m)}(s)$ as a sum over all modes. The longitudinal m-pole wake potential is:

$$W_{\parallel}^{(m)}(s) = -\sum_n \; 2\,\frac{1}{a^{2\,m}}\,k_{\parallel n}^{(m)}(a)\cos(\omega_n\,s/c), \qquad s>0, \tag{22}$$

where ω_n are the frequencies of the m-pole modes, and $k_{\parallel n}^{(m)}(a)$ are the loss parameters. The transverse m-pole wake potential ($m>1$) according to equation (22) and (21) is:

$$W_{\perp}^{(m)}(s) = \sum_n \; 2\,\frac{k_{\parallel n}^{(m)}(a)}{\omega_n\,a^{2m}/c}\;\sin(\omega_n\,s/c), \qquad s>0. \tag{23}$$

For dipole modes it is common to define a kick parameter $k_{\perp n}$:

$$k_{\perp n} = \frac{k_{\parallel n}^{(1)}(a)}{\omega_n\,a^2/c}. \tag{24}$$

It is possible to rewrite the above equations in terms of $R^{(m)}/Q$:

$$\begin{aligned} W_{\parallel}^{(m)}(s) &= -\sum_n \; \omega_n \left(\frac{R^{(m)}}{Q}\right)_n \cos(\omega_n\,s/c)\;\exp(-1/\tau_n\;s/c) \\ W_{\perp}^{(m)}(s) &= c\sum_n \; \left(\frac{R^{(m)}}{Q}\right)_n \sin(\omega_n\,s/c)\;\exp(-1/\tau_n\;s/c). \end{aligned} \tag{25}$$

A damping term has been included with the damping time τ_n for mode n. For superconducting cavities the damping time τ_n is usually dominated by the external Q-value. The damping time is therefore:

$$\tau_n \approx \frac{2\,(Q_{ext})_n}{\omega_n}. \tag{26}$$

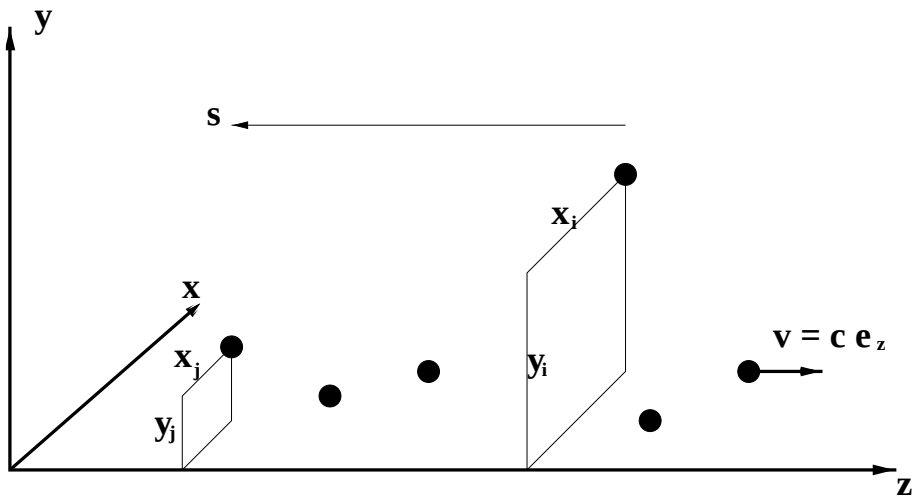

Figure 9: Schematic representation of a train of bunches with offsets x_i and y_i with respect to the reference axis of the accelerator.

2.2.3 Effects of long range wakefields on a bunch train

The long range wakes due to HOMs can cause energy deviations and kicks on the bunches, which can result in a cumulative beam-breakup instability. Longitudinal and transverse effects are considered up-to second order, i.e. energy deviations due to monopole and dipole wakefields and kicks due to dipole and quadrupole wakefields are taken into account. A bunch train of I bunches is schematically shown in Fig. 9 to clarify the notation for the offsets x_i and y_i with respect to the reference axis of the accelerator and the direction of the longitudinal coordinate s ($s = 0$ at the first bunch of the train). It is assumed that all bunches have the same bunch charge q.

The energy deviation of bunch j due to HOMs is a sum over all HOMs produced by all preceding bunches in the train. The self-wake due to HOMs is regarded as a single bunch effect, which is not considered here.

$$\begin{aligned} \Delta E(s_j) &= -e\,q \sum_{i<j} W_{\parallel}^{(0)}(s_j - s_i) \\ &\quad -e\,q \sum_{i<j} \left(x_j\,x_i + y_j\,y_i\right)\, W_{\parallel}^{(1)}(s_j - s_i) \\ &\quad + \ldots \end{aligned} \tag{27}$$

As an example the energy deviation due to a mode with a frequency of $f = 2$ GHz excited by a bunch with a population of $N = 2 \cdot 10^9$ electrons is given by:

$$\Delta E = e\,3.2\,\mathrm{nC}\;\; 2\,\pi\;\, 2\,\mathrm{GHz}\;\frac{R}{Q}. \tag{28}$$

An energy deviation of 1 keV corresponds to impedance of about 25 Ω and a

loss parameter of $k_{\|}^{(0)} = 0.156$ V/pC. It has been assumed that the full wake amplitude acts on the test bunch ($\cos(\omega s/c) = 1$, no damping).

Now consider the bunch train. The kick on bunch j due to the dipole wake field is:

$$\boldsymbol{\theta}_j = \frac{e\,q}{E_j} \sum_{i<j} (x_i\ \boldsymbol{e_x} + y_i\ \boldsymbol{e_y}) W_{\perp}^{(1)}(s_j - s_i), \tag{29}$$

where E_j is the energy of bunch j. As an example consider again a mode with frequency $f = 2$ GHz, excited by a bunch transversing the cavity with an offset x_1. The kick on a trailing bunch of energy 5 GeV is:

$$\begin{aligned} \theta_{x,2} &= \frac{e\,3.2\mathrm{nC}}{5\mathrm{GeV/c}} \frac{R^{(1)}}{Q}\ x_1 \\ &= 1.921 \cdot 10^{-8}\,\frac{\mathrm{cm}}{\Omega}\,\frac{R^{(1)}}{Q}\ x_1. \end{aligned} \tag{30}$$

A kick of 0.1 μrad (for an offset of $x_1 = 1$ cm of the leading bunch) corresponds to a impedance of $(R/Q)^{(1)} = 5.2\,\Omega/\mathrm{cm}^2$. The longitudinal dipole loss parameter $k_{\|}^{(1)}(1\,\mathrm{cm})$ is 0.033 V/pC. If the leading *and* the trailing charges transverse the structure with an offset of 1 cm then the energy deviation due to the dipole wake will be 0.21 keV.

The effect of the quadrupole wake is best represented by the following matrix:

$$\begin{pmatrix} x_{j,a} \\ x'_{j,a} \\ y_{j,a} \\ y'_{j,a} \end{pmatrix} = \begin{pmatrix} 1 & 0 & 0 & 0 \\ {f_{q,j}}^{-1} & 1 & {f_{sq,j}}^{-1} & 0 \\ 0 & 0 & 1 & 0 \\ {f_{sq,j}}^{-1} & 1 & -{f_{q,j}}^{-1} & 0 \end{pmatrix} \begin{pmatrix} x_{j,b} \\ x'_{j,b} \\ y_{j,b} \\ y'_{j,b} \end{pmatrix}. \tag{31}$$

The index a indicates the phase space coordinates of the bunch j **a**fter the quadruple wakefield kicks has been applied, while the index b indicates the coordinates **b**efore the wakefield kicks have been applied. The focal length of the normal ($f_{q,j}$) and skew ($f_{sq,j}$) quadrupole wakes are:

$$\begin{aligned} \frac{1}{f_{q,j}} &= \frac{e\,q}{E_j}\ 2\ \sum_{i<j} ({x_i}^2 + {y_i}^2)\ W_{\perp}^{(2)}(s_j - s_i) \\ \frac{1}{f_{sq,j}} &= \frac{e\,q}{E_j}\ 2\ \sum_{i<j}\ 2\ (x_i\ y_i)\ W_{\perp}^{(2)}(s_j - s_i), \end{aligned} \tag{32}$$

where E_j is the energy of bunch j.

3 Dispersion curves for monopole, dipole and quadrupole modes

3.1 The TESLA cavity as a periodic transmission line

In this section results for single cell cavities are presented, which have been obtained from numerical calculations with the computer code MAFIA [5, 6] using periodic boundary conditions. In Fig. 10 the shape of a TESLA center cell is shown together with the MAFIA grid (about 12000 grid points, 1 mm step size), and the electric field of the π-mode. All modes of an infinite periodic chain of cavities can be obtained from single cell calculations using periodic boundary conditions:

$$\widetilde{\boldsymbol{E}}^{(m)}(r, z+g) = \widetilde{\boldsymbol{E}}^{(m)}(r, z)\ \exp(i\varphi), \tag{33}$$

where φ is the phase advance per cell, and g the cell length. A phase advance of 180° (or π) corresponds to the case shown in Fig. 10. The frequencies of the lowest pass-bands (see [12]) are graphically represented in the form of dispersion curves in Fig. 11, 12, and 13 for monopole, dipole and quadrupole modes of the TESLA cavity. There are dispersion curves with positive slopes corresponding to forward traveling waves (positive group velocity) and some with negative slopes corresponding to backward traveling wave (negative group velocity).

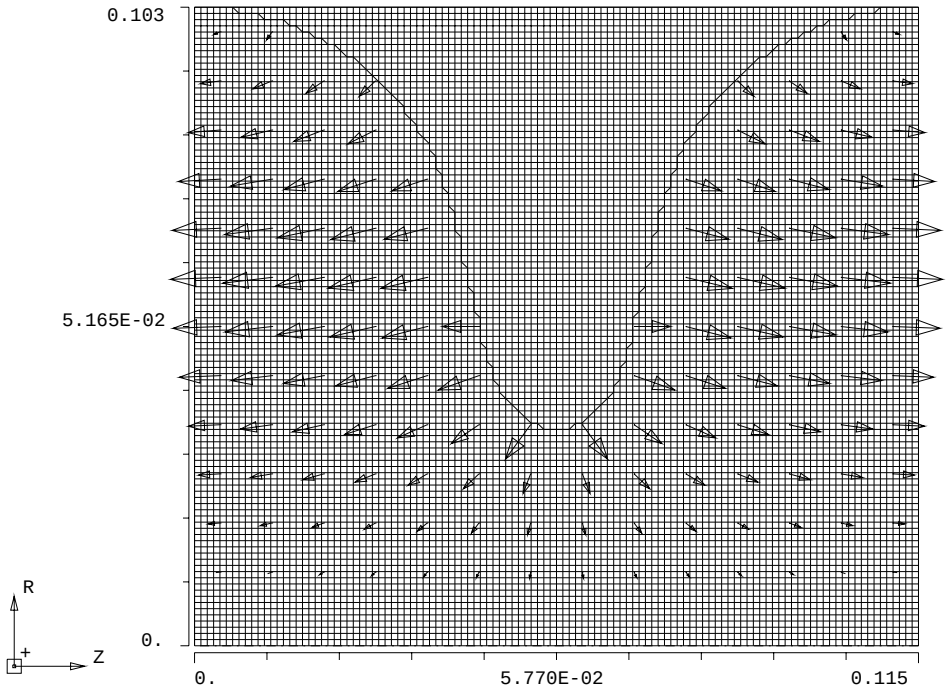

Figure 10: Center cell of a TESLA cavity approximated with a mesh. The arrows represent the electric field of the π-mode (phase advance of 180° per cell).

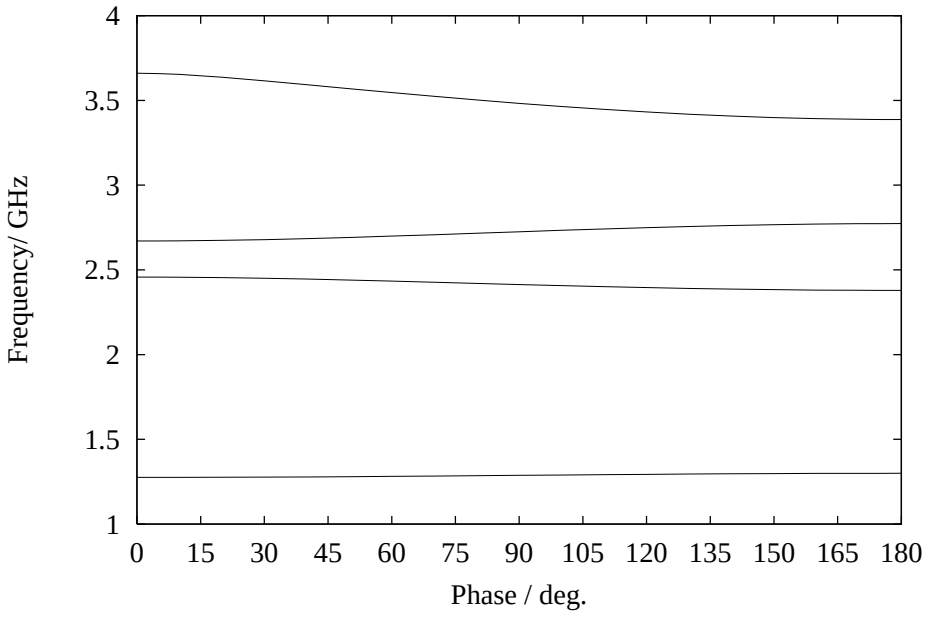

Figure 11: Dispersion curves for monopole modes.

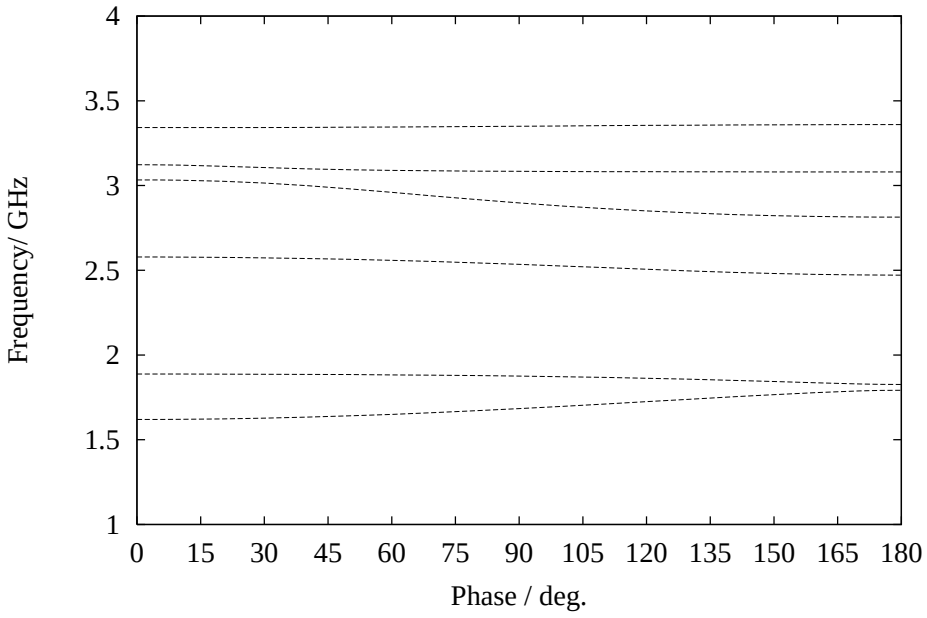

Figure 12: Dispersion curves for dipole modes.

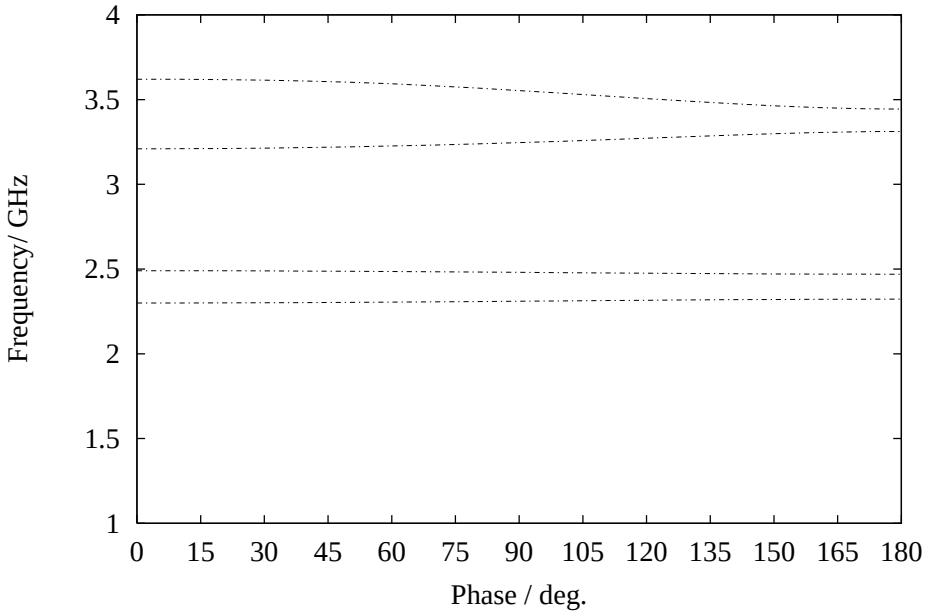

Figure 13: Dispersion curves for quadrupole modes.

The frequencies of the 0- and π-modes of each passband, shown in Fig. 11, 12, and 13, are listed in table 2:

type	band #	f_0 / GHz	f_π / GHz
M	1	1.2755	1.2996
D	1	1.6197	1.7920
D	2	1.8877	1.8261
Q	1	2.2996	2.3223
M	2	2.4576	2.3789
Q	2	2.4903	2.4699
D	3	2.5782	2.4713
M	3	2.6704	2.7730
D	4	3.0333	2.8134
D	5	3.1231	3.0802
Q	3	3.2096	3.3119
D	6	3.3419	3.3595
Q	4	3.6204	3.4443
M	4	3.6603	3.3871

Table 2: Passband limits of the lowest monopole (M), dipole (D), and quadrupole (Q) modes. The bands are sorted with respect to the 0-mode frequency and labeled by their type and the band number within each type.

The dispersion curves for all bands in table 2 are plotted in (Fig. 14) together

with the "light cone".

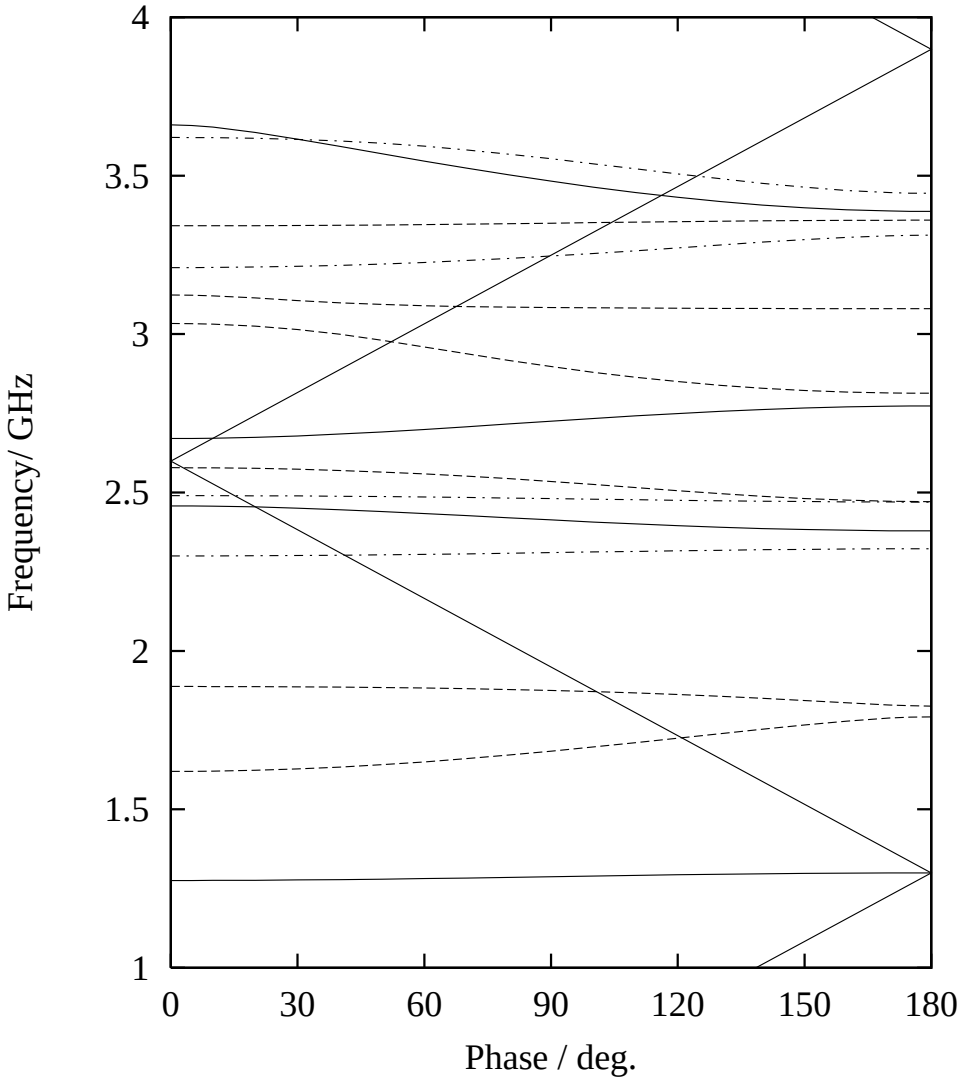

Figure 14: Dispersion curves for monopole (solid line), dipole (dashed line) and quadrupole (dash-dotted line) modes.

A beam excites most strongly those modes which are synchronous to the beam, i.e. modes with a phase velocity equal to the speed of light:

$$c = v_{ph} = \frac{\omega}{k_z} = 2\,\pi\ g\ \frac{f}{\varphi}, \tag{34}$$

where k_z is the longitudinal wave number (sometimes also denoted as β), g the cavity gap length and $\varphi = k_z\ g$ is the phase advance per cell, which is used as an abscissa in the plots of the dispersion curves. The light cone is the straight

line $f(\varphi) = \varphi\, c/(2\,\pi\, g)$, which is folded into the phase range from 0 to 180° in Fig. 14 using the periodicity of the structure. The TESLA cavity is designed such that the light cone intersects the π-mode of the first monopole passband ($f \approx 1.3$ GHz). The time-average power flow in the passbands is equal to the group velocity, defined as

$$v_g = \frac{d\omega}{dk_z} = 2\,\pi\; g\; \frac{df}{d\varphi}, \tag{35}$$

times the time-average stored energy per period divided by the period [12]. The group velocity in units of c has been calculated for all passbands shown in Fig. 14. Fig. 15 shows v_g/c for the lowest monopole passbands. The accelerating mode is a standing wave with phase advance $\varphi = \pi$ and $v_g = 0$. The group velocities of the lowest six dipole passbands are shown in Fig. 16 and Fig. 17. The third and sixth bands have rather low group velocities for all phase advances per cell: $|v_g| \leq 0.14$ for the third band and $|v_g| \leq 0.025$ for the sixth band. Such low group velocities for a periodic transmission line indicate that in a cavity with a finite number cells modes are present which are trapped or only weakly coupled to the beam pipe. The group velocities of the lowest four quadruple modes are shown in Fig. 18.

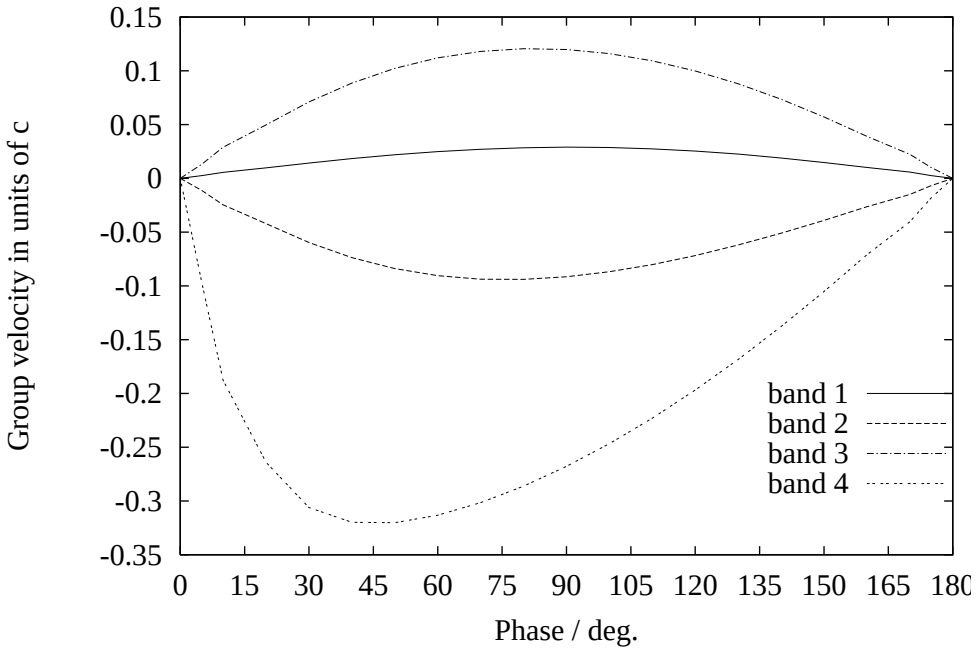

Figure 15: Group velocities of the lowest four monopole bands.

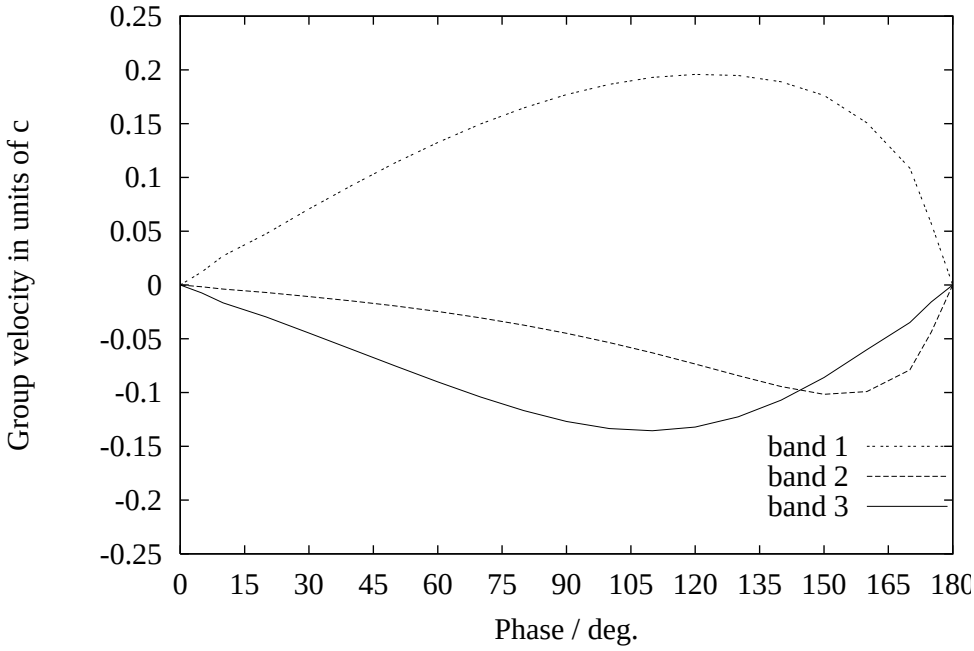

Figure 16: Group velocities of the lowest three dipole bands.

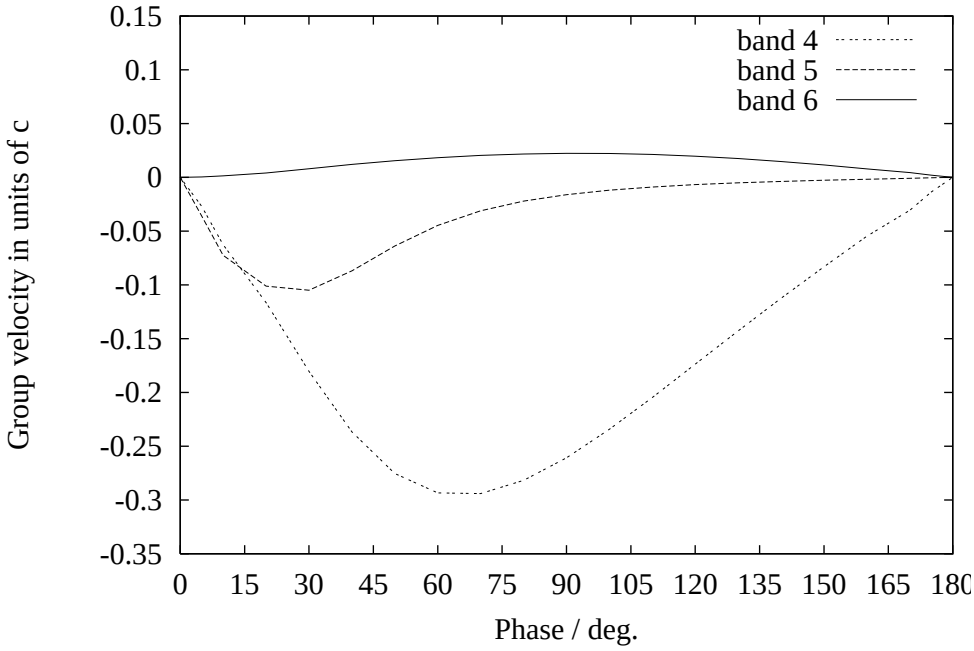

Figure 17: Group velocities of the dipole bands four, five and six.

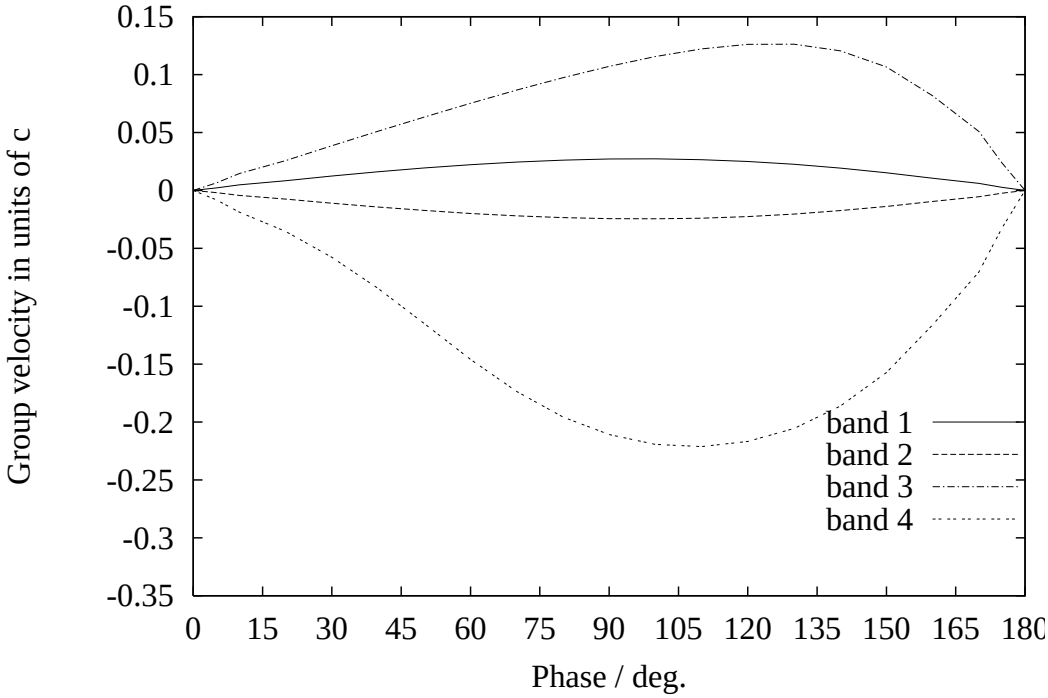

Figure 18: Group velocities of the lowest four quadruple bands.

3.2 Circular waveguides

A beam pipe is connected to each end of the 9-cell TESLA cavity. Therefore the properties of the modes which can propagate in a simple circular waveguide [14] are summarized. In general one can distinguish TM- and TE-modes, which are characterized by the properties of the electric and magnetic field components.

For **TM-modes** the longitudinal magnetic field vanishes everywhere, and the longitudinal electric field is a solution of the differential equation:

$$\left[{\boldsymbol{\nabla}_\perp}^2 + \left(\left(\frac{\omega}{c} \right)^2 - {k_z}^2 \right) \right] E_z = 0, \qquad B_z \equiv 0. \tag{36}$$

In the case of a circular waveguide (beam pipe) the solution is

$$E_z \sim J_m(j_{n,m}\, r/r_0)\, \exp(i\, m\, \phi), \tag{37}$$

where $j_{n,m}$ is the n-th zero of the Bessel-function J_m, and r_0 is the radius of the beam pipe. This solution is required by the boundary condition $E_z(r_0) = 0$ at the inner surface of the pipe. The mode is called a $\mathrm{TM}_{m,n}$ mode. All transverse fields are determined by the longitudinal ones:

$$\boldsymbol{E}_\perp = i\, \frac{k_z}{\sqrt{(\omega/c)^2 - {k_z}^2}}\, \boldsymbol{\nabla}_\perp E_z, \qquad \boldsymbol{B}_\perp = \frac{1}{c}\, \frac{\omega/c}{k_z}\, \boldsymbol{e_z} \times \boldsymbol{E}_\perp, \tag{38}$$

with e_z the unit vector in the z-direction. From equations (36) and (37) the following dispersion relation is obtained:

$$f = \frac{c}{2\,\pi}\sqrt{\left(\frac{j_{n,m}}{r_0}\right)^2 + {k_z}^2}, \tag{39}$$

where k_z is the propagation constant in the longitudinal direction. Only modes with frequencies f above the cutoff frequency

$$f_{cTM} = c\,\frac{j_{n,m}}{2\,\pi}\,\frac{1}{r_0} \tag{40}$$

can propagate in the beam pipe (i.e. real k_z).

For **TE-modes** the longitudinal electric field vanishes everywhere, and the longitudinal magnetic field is a solution of the differential equation:

$$\left[{\boldsymbol{\nabla}_\perp}^2 + \left(\left(\frac{\omega}{c}\right)^2 - {k_z}^2\right)\right] B_z = 0, \qquad E_z \equiv 0. \tag{41}$$

The transverse fields are determined by the longitudinal ones:

$$\boldsymbol{B}_\perp = i\,\frac{k_z}{\sqrt{(\omega/c)^2 - {k_z}^2}}\,\boldsymbol{\nabla}_\perp B_z, \qquad \boldsymbol{E}_\perp = c\,\frac{\omega/c}{k_z}\,\boldsymbol{B}_\perp \times \boldsymbol{e_z}. \tag{42}$$

In the case of a circular waveguide (beam pipe) the solution of equation (41) must fulfill the boundary condition B_r=0 or $\partial B_z/\partial r = 0$ at the inner surface of the pipe. The following solution

$$B_z \sim J_m(j'_{n,m}\,r/r_0)\,\exp(i\,m\,\phi), \tag{43}$$

meets the requirement where $j'_{n,m}$ is the n-th zero of the derivative of the m-th Bessel-function. The mode is called a $\mathrm{TE}_{m,n}$ mode. The derivatives of the Bessel-functions can be written in terms of Bessel-functions. For $m = 0, 1,$ and 2 one obtains:

$$\begin{aligned}
\frac{d}{dx}J_0(x) &= -J_1(x) \\
\frac{d}{dx}J_1(x) &= J_0(x) - \frac{1}{x}\,J_1(x) \\
\frac{d}{dx}J_2(x) &= J_1(x) - \frac{2}{x}\,J_2(x).
\end{aligned} \tag{44}$$

From equations (41) and (43) the following dispersion relation is obtained:

$$f = \frac{c}{2\,\pi}\sqrt{\left(\frac{j'_{n,m}}{r_0}\right)^2 + {k_z}^2}. \tag{45}$$

The cutoff frequency for TE-modes is:

$$f_{cTE} = c\,\frac{j'_{n,m}}{2\,\pi}\,\frac{1}{r_0}. \tag{46}$$

The first seven zeros of the Bessel-functions and their derivatives of order $m = 0, 1$, and 2 multiplied by the factor $c/(2\,\pi)$ are listed in table 3. The cutoff frequencies for the TM- and TE-modes are listed in table 4 for a circular wave guide with a radius of 35 mm and of 39 mm corresponding to the iris radius of a center cell and an end cell of a TESLA cavity, respectively.

	$c\,j_{n,m}/(2\,\pi)$ / (GHz cm)			$c\,j'_{n,m}/(2\,\pi)$ / (GHz cm)		
n	m=0	m=1	m=2	m=0	m=1	m=2
1	11.4743	0	0	0	8.7849	0
2	26.3382	18.2824	24.5038	18.2824	25.4382	14.5728
3	41.2899	33.4738	40.1616	33.4738	40.7297	31.9973
4	56.2615	48.5411	55.4423	48.5411	55.8534	47.5678
5	71.2406	63.5719	70.5966	63.5719	70.9193	62.8404
6	86.2233	78.5871	85.6925	78.5871	85.9583	77.9997
7	101.2080	93.5940	100.7565	93.5940	100.9825	93.1028

Table 3: Zeros of Bessel-functions and their derivatives multiplied by the factor $c/(2\,\pi)$.

	Circular waveguide with a radius of 35 mm					
	f_{cTM} / GHz			f_{cTE} / GHz		
n	m=0	m=1	m=2	m=0	m=1	m=2
1	3.2784	0	0	0	2.5099	0
2	7.5252	5.2235	7.0011	5.2235	7.2680	4.1637
3	11.7971	9.5639	11.4747	9.5639	11.6371	9.1421
4	16.0747	13.8689	15.8406	13.8689	15.9581	13.5907

	Circular waveguide with a radius of 39 mm					
	f_{cTM} / GHz			f_{cTE} / GHz		
n	m=0	m=1	m=2	m=0	m=1	m=2
1	2.9421	0	0	0	2.2525	0
2	6.7534	4.6878	6.2830	4.6878	6.5226	3.7366
3	10.5872	8.5830	10.2978	8.5830	10.444	8.2044
4	14.4260	12.4464	14.2160	12.4464	14.321	12.1969

Table 4: Cutoff frequencies for TM- and TE-modes in a circular waveguide with a radius of 35 mm and of 39 mm.

4 Monopole modes in a TESLA 9-cell cavity

The passband structure of one cavity has been studied in the previous section. The goal of this section is to relate the results for a periodic structure to a TESLA TDR-like 9-cell cavity. Fig. 19 shows the considered 9-cell cavity with symmetric end-cells (cup 1) and the electric field of the accelerating mode (π-mode) calculated with the MAFIA code [5, 6]. The cavity is approximated on a

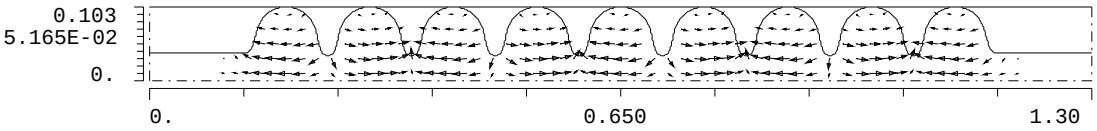

Figure 19: Electric field of the accelerating mode (π-mode) of a TESLA TDR-like 9-cell cavity.

grid with a step size of 2 mm corresponding to about 33000 mesh points for the 9-cell structure shown in Fig. 19. A detailed view of the first cell together with the MAFIA mesh is shown in Fig. 20. A mesh with this step size is used for all two dimensional MAFIA calculations of 9-cell cavities presented in this report. The mesh lines are chosen such that the iris radius of the cell and the equator radius of the mid cell and the end-cell are exactly matched by a mesh line. The

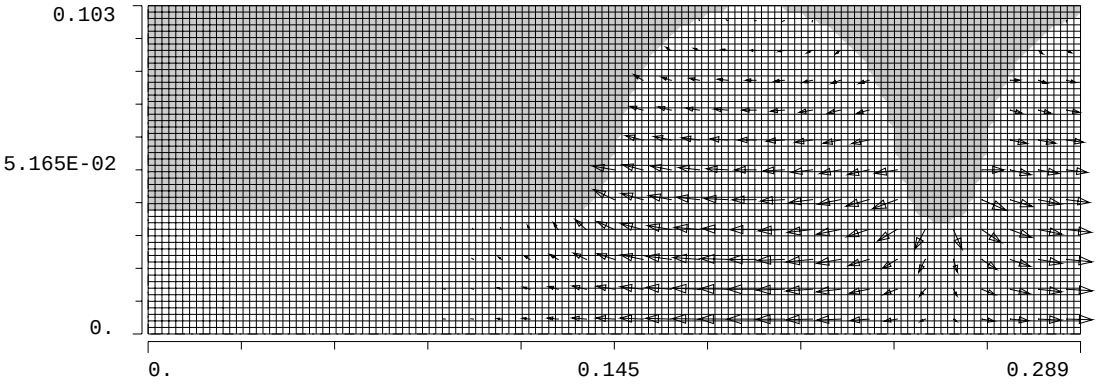

Figure 20: First cell of a TESLA TDR-like 9-cell cavity approximated on the mesh. The arrows represent the electric field of the accelerating mode (π-mode).

longitudinal component of the electric field of the accelerating mode on the axis of a TESLA TDR-like 9-cell cavity is show in Fig. 21 for an accelerating gradient of 25 MV/m. A good field flatness is achieved although the cell geometry is approximated on a mesh as described above.

In general one has to distinguish between TM- and TE-monopole modes. The beam can only interact with TM-modes and not with TE-modes since $E_z \equiv 0$ for TE-modes, i.e. the loss parameter is identically zero. Therefore the following investigation of monopole modes is focused on TM-modes. For the sake of

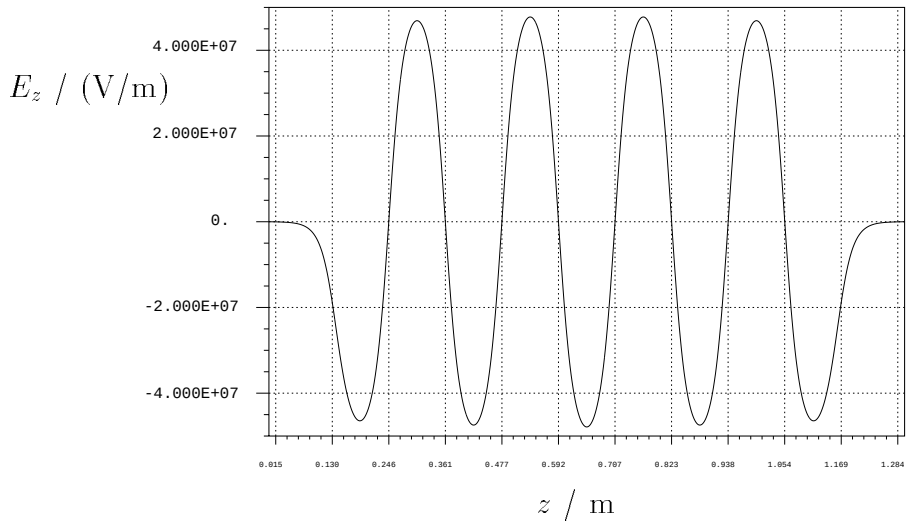

Figure 21: Longitudinal electric field (E_z) of the accelerating mode (π-mode) on the axis of a TESLA TDR-like 9-cell cavity. This field corresponds to an accelerating gradient of 25 MV/m

completeness a list of the frequencies of the lowest monopole TE-passbands will be included in a short subsection since these modes may be observed in bench measurements where modes are excited by an antenna. Please note that this distinction is only necessary for monopole modes; dipole and quadrupole modes in a multi-cell cavity are in any case of hybrid character.

4.1 TM-monopole modes

The modes in a 9-cell cavity may also be labeled by their phase advance per cell. If the structure is tuned for a flat π-mode the phase advance of the nine modes per band are $\pi/9$, $2\pi/9$, ..., and $9\pi/9$ based on an equivalent circuit model [15, p.131]. The electric field of the $\pi/9$-modes of the first and second passbands are shown in Fig. 22 and Fig. 23. In addition to this equivalent circuit approach

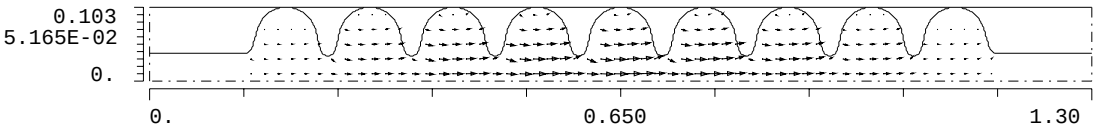

Figure 22: Electric field of the $\pi/9$-mode ($f = 1.2756$ GHz) of the first monopole passband of a TESLA TDR-like 9-cell cavity.

the phase advance per cell can be calculated directly using the electric field as determined with the MAFIA code to obtain the phase advance per cell. Based

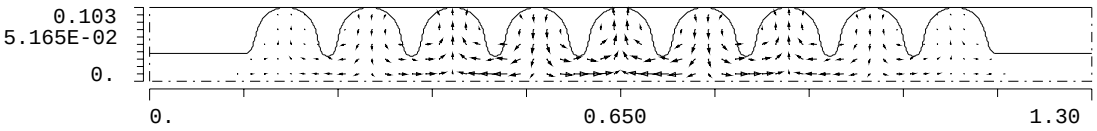

Figure 23: Electric field of the $\pi/9$-mode ($f = 2.38$ GHz) of the second monopole passband of a TESLA TDR-like 9-cell cavity.

on equation (33) for periodic structures one may use the following relations

$$\begin{aligned} E_z(r,z)\ \exp(i\varphi) &= E_z(r, z + L_{cell}) \\ E_z(r,z)\ \exp(-i\varphi) &= E_z(r, z - L_{cell}) \\ 2\ E_z(r,z)\ \cos(\varphi) &= E_z(r, z + L_{cell}) + E_z(r, z - L_{cell}), \end{aligned} \tag{47}$$

which are strictly valid for a periodic structure, to define a phase advance per cell at position z [16] as

$$\varphi(z) = \arccos\left(\frac{E_z(r, z + L_{cell}) + E_z(r, z - L_{cell})}{2\ E_z(r,z)}\right), \tag{48}$$

where $E_z(r,z)$ is the longitudinal electric field as calculated by MAFIA [5]. In the center cells of the cavities the above defined phase advance $\varphi(z)$ is approximately independent of the longitudinal position z, which is demonstrated for the accelerating mode in Fig. 24. The phase advance per cell is constant (about 176°) in the region of the center cells of the cavity. Equation (48) has been used to calculate

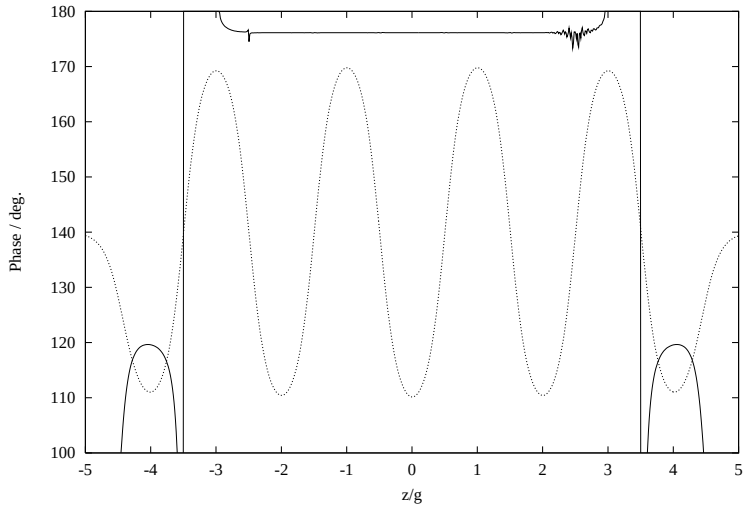

Figure 24: Phase advance per cell versus position for the accelerating mode (solid line) according to equation (48) and the electric field E_z of the mode (dotted line).

the phase advance per cell (in the center cell) for the lowest 45 TM-monopole

modes of the 9-cell TESLA TDR-like cavity. The result is displayed in Fig. 25 together with dispersion curves for the lowest 4 passbands previously presented in section 3. Magnetic (M) boundary conditions have been used at both ends

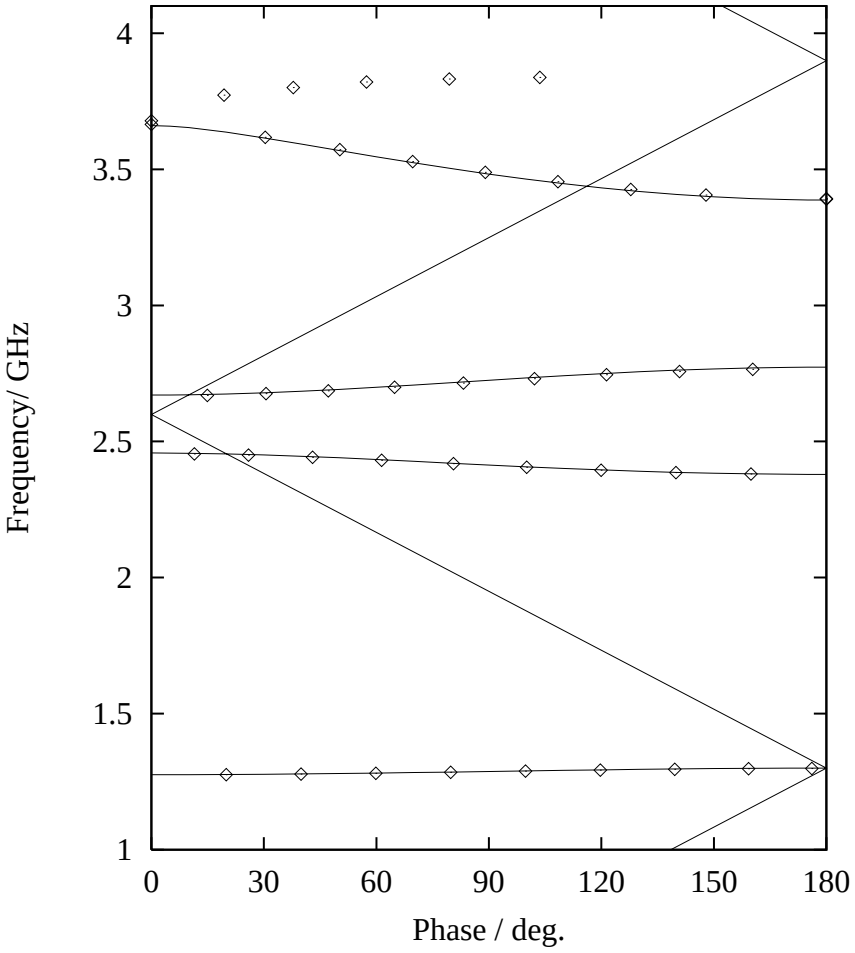

Figure 25: Dispersion curves for monopole modes (lowest 4 bands) and the monopole modes in a 9-cell TESLA TDR-like cavity (diamonds, boundary condition MM).

of the 9-cell cavity, i.e. the longitudinal electric field E_z is zero at both ends of the cavity. The modes are labeled MM-1 to MM-45, where the mode MM-1 is the TM-monopole mode with the lowest frequency. The frequencies of the lowest 3 passbands do essentially not depend on the boundary conditions since these modes are below the cut-off frequency of the beam pipe. The basic rf-parameters (described in 2) for modes MM-1 to MM-45 are listed in tables 5 and 6.

A graphical representation of the longitudinal electric field on the cavity axis and the radial electric field at a offset of 1 cm from the cavity axis are given in

mode	f /GHz	$k^{(0)}$/ V/(pC)	G_1 /Ω	$(R/Q)^{(0)}$ / Ω	$Q_0/Q_{0\,FM}$	φ /°
Band 1						
MM- 1	1.2756	$0.848\ 10^{-06}$	252.7	0.0002	1.027	20.0
MM- 2	1.2776	$0.239\ 10^{-06}$	252.9	0.0001	1.025	39.9
MM- 3	1.2807	$0.523\ 10^{-05}$	253.2	0.0013	1.021	59.9
MM- 4	1.2845	$0.187\ 10^{-05}$	253.5	0.0005	1.017	79.8
MM- 5	1.2885	$0.217\ 10^{-05}$	253.9	0.0005	1.012	99.8
MM- 6	1.2924	$0.776\ 10^{-05}$	254.2	0.0019	1.007	119.7
MM- 7	1.2955	$0.138\ 10^{-03}$	254.5	0.0339	1.003	139.6
MM- 8	1.2976	$0.662\ 10^{-04}$	254.7	0.0163	1.001	159.2
MM- 9	1.2983	2.08	254.8	511.0652	1.000	176.1
Band 2						
MM-10	2.3800	$0.746\ 10^{-05}$	370.6	0.0010	0.433	159.9
MM-11	2.3856	$0.147\ 10^{-03}$	370.7	0.0196	0.431	139.9
MM-12	2.3943	$0.248\ 10^{-03}$	370.9	0.0329	0.428	119.9
MM-13	2.4055	$0.414\ 10^{-03}$	371.2	0.0547	0.424	100.1
MM-14	2.4181	$0.376\ 10^{-02}$	371.3	0.4943	0.420	80.6
MM-15	2.4308	$0.573\ 10^{-04}$	371.2	0.0075	0.416	61.4
MM-16	2.4419	0.08	370.6	10.2352	0.411	43.0
MM-17	2.4499	0.60	369.0	77.6533	0.407	25.9
MM-18	2.4539	0.57	365.9	73.8717	0.402	11.5
Band 3						
MM-19	2.6695	$0.363\ 10^{-03}$	546.8	0.0433	0.508	14.9
MM-20	2.6756	$0.291\ 10^{-02}$	548.7	0.3465	0.507	30.6
MM-21	2.6858	$0.118\ 10^{-02}$	550.9	0.1395	0.505	47.2
MM-22	2.6993	$0.141\ 10^{-02}$	554.2	0.1659	0.503	64.8
MM-23	2.7148	$0.166\ 10^{-02}$	559.7	0.1948	0.502	83.2
MM-24	2.7307	$0.198\ 10^{-03}$	567.6	0.0231	0.504	102.1
MM-25	2.7453	$0.825\ 10^{-03}$	577.1	0.0957	0.507	121.4
MM-26	2.7571	$0.236\ 10^{-05}$	586.4	0.0003	0.510	140.8
MM-27	2.7648	$0.965\ 10^{-04}$	593.3	0.0111	0.513	160.4

Table 5: A list of monopole modes in a 9-cell TESLA TDR-like cavity for the 1st, 2nd and 3rd passbands.

Appendix A.

4.2 TE-monopole modes

The beam cannot excite TE-modes since all monopole TE-modes are characterized by the condition $E_z \equiv 0$. The mode with the lowest frequency (f = 2.5047 GHz) is shown in Fig. 26. A list of the first 30 monopole TE-modes found

mode	f /GHz	$k^{(0)}$/ V/(pC)	G_1 /Ω	$(R/Q)^{(0)}$ / Ω	$Q_0/Q_{0\,FM}$	φ /°
MM-28	3.0971	0.02	464.6	1.8325	0.320	—
MM-29	3.0971	$0.377\ 10^{-04}$	464.6	0.0039	0.320	—
Band 4						
MM-30	3.3898	$0.981\ 10^{-02}$	542.9	0.9210	0.313	180.0
MM-31	3.3921	$0.388\ 10^{-02}$	541.8	0.3638	0.311	180.0
MM-32	3.4055	$0.592\ 10^{-02}$	553.4	0.5537	0.316	147.9
MM-33	3.4261	$0.977\ 10^{-02}$	565.7	0.9075	0.319	127.8
MM-34	3.4541	$0.144\ 10^{-02}$	580.9	0.1327	0.322	108.4
MM-35	3.4885	$0.689\ 10^{-02}$	597.6	0.6283	0.325	89.1
MM-36	3.5283	$0.538\ 10^{-02}$	614.1	0.4851	0.326	69.7
MM-37	3.5719	$0.163\ 10^{-05}$	627.8	0.0001	0.326	50.2
MM-38	3.6174	$0.954\ 10^{-02}$	633.8	0.8397	0.320	30.4
MM-39	3.6650	0.03	623.6	2.8606	0.307	0.0
MM-40	3.6783	$0.455\ 10^{-03}$	596.0	0.0394	0.291	0.0
MM-41	3.7727	$0.152\ 10^{-02}$	816.4	0.1286	0.379	19.4
MM-42	3.8005	0.01	730.7	1.0079	0.335	37.8
MM-43	3.8206	$0.180\ 10^{-02}$	661.5	0.1501	0.300	57.4
MM-44	3.8319	$0.858\ 10^{-02}$	615.5	0.7127	0.277	79.5
MM-45	3.8376	0.02	591.9	1.5472	0.266	103.6

Table 6: A list of monopole modes in a 9-cell TDR-like TESLA cavity for the higher passbands.

with the MAFIA eigenvalue solver using magnetic boundary conditions (MM) at both cavity ends are given in table 7. The geometry parameter and the phase advance per cell have been calculated. The loss parameter and R/Q are zero for all monopole TE-modes. Nevertheless these modes may be excited by an antenna in bench measurements.

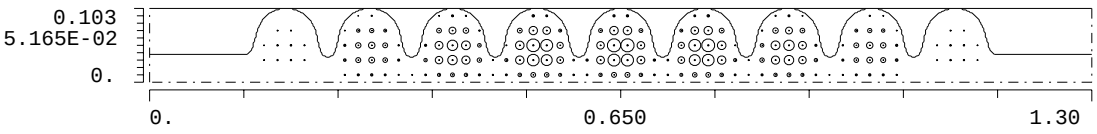

Figure 26: Electric field of the $\pi/9$-mode ($f = 2.5047$ GHz) of the first TE-monopole passband of a TESLA TDR-like 9-cell cavity.

mode	f /GHz	G_1 /Ω	φ /°	
MM- 1	2.5047	798.1	20.9	
MM- 2	2.5052	800.1	41.7	
MM- 3	2.5060	803.3	62.9	
MM- 4	2.5070	807.2	84.2	
MM- 5	2.5080	811.5	105.9	
MM- 6	2.5089	815.6	128.4	
MM- 7	2.5096	819.2	152.7	
MM- 8	2.5108	818.6	—	
MM- 9	2.5108	818.7	—	
MM-10	3.7292	1301.9	—	
MM-11	3.7292	1301.9	—	
MM-12	3.7324	1353.1	23.4	
MM-13	3.7333	1343.2	46.6	
MM-14	3.7348	1328.3	69.6	
MM-15	3.7370	1309.8	92.4	
MM-16	3.7399	1288.8	114.9	
MM-17	3.7436	1266.5	137.3	
MM-18	3.7483	1243.7	159.4	
MM-19	3.7533	1052.8	180.0	
MM-20	3.7601	1222.5	157.5	
MM-21	3.7670	1208.1	136.3	
MM-22	3.7742	1199.3	115.5	
MM-23	3.7812	1193.4	95.0	
MM-24	3.7876	1188.6	75.0	
MM-25	3.7929	1183.8	55.5	
MM-26	3.7969	1178.6	36.6	
MM-27	3.7994	1174.0	18.1	
MM-28	4.6552	978.9	—	
MM-29	4.6552	978.9	—	
MM-30	4.6977	1378.6	158.2	

Table 7: List of TE-monopole modes in a 9-cell TESLA TDR-like cavity. The loss parameter is zero for all monopole TE-modes.

5 Dipole modes in a TESLA 9-cell cavity

The dipole modes have been studied for several configurations of the TESLA 9-cell cavities, which differ in the length of the beam pipe between the cavities. Furthermore different boundary conditions have been used (electric E and magnetic M). The goal is to relate the modes of a nine cell structure to the dispersion curves obtained for a single cavity cell using periodic boundary conditions. Equation (48) is used to calculate the phase advance per cell for each mode in a nine cell cavity as discussed in the section 4.1 covering monopole modes. The properties of the modes including frequency, loss parameter and geometry parameter are presented in tables for the six lowest passbands. Furthermore graphical representations of the electric fields are given in appendix B for all modes of the TDR-like cavity with magnetic boundary conditions and for the other configurations if there are significant differences of the results from those of the TDR-like cavity.

For dipole modes several configurations are discussed in more detail than were made in the case of the monopole modes since dipole modes are the modes which drive the cumulative multibunch beam break-up instability which can cause problems for transverse beam dynamics. There are no pure TM- or TE-modes as in the case of monopole modes since dipole modes in a multicell cavity are of hybrid character. Nevertheless the modes are called TM-like or TE-like modes depending on their field pattern. In any case, also for TE-like dipole modes, the longitudinal electric field (E_z) determines the R/Q of a mode.

5.1 The TESLA 9-cell cavity with TDR-like beam pipes

The modes of the first two passbands are below the cutoff frequencies of the beam pipe. Fig. 27 shows the dipole mode with the lowest frequncy ($f = 1.629$ GHz) of a TDR-like TESLA 9-cell cavity. Magnetic boundary conditions have been applied at both ends of the cavity. The mode is labeled MM-1 since it is the first mode found with the MAFIA [6] eigenvalue solver with magnetic (MM) boundary conditions. Based on the field pattern this mode is clearly clssified as a TE-like mode. The electric field of mode MM-7 ($f = 1.739$ GHz) is show in Fig. 28, which is the mode with the largest R/Q of those in the first dipole passband. This mode is clearly of hybrid character, in some cells looking like a TE-like mode while in other cells a more TM-like field pattern is present. Mode MM-14 ($f = 1.873$ GHz) is the mode with the largest R/Q of those in the second passband. The electric field is shown in Fig. 29.

Finally the mode with the highest frequency in the second passband (MM-18, $f = 1.887$ GHz) is shown in Fig. 30.

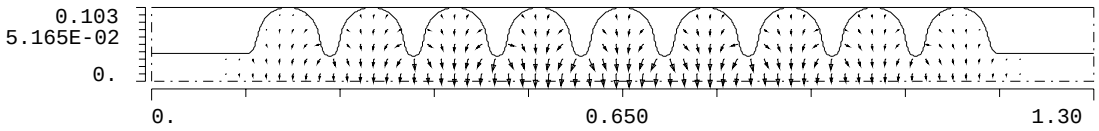

Figure 27: Electric field of the dipole mode MM-1 of a TESLA TDR-like 9-cell cavity. This is the dipole mode with the lowest frequency from the first passband of a 9-cell cavity.

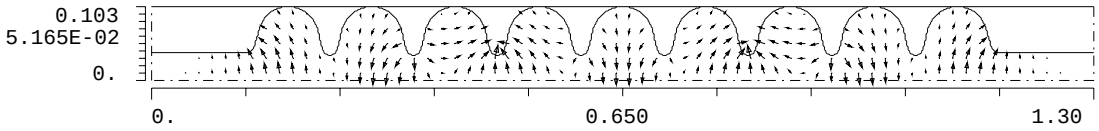

Figure 28: Electric field of the dipole mode MM-7 of a TESLA TDR-like 9-cell cavity. This mode has the largest R/Q in the first passband.

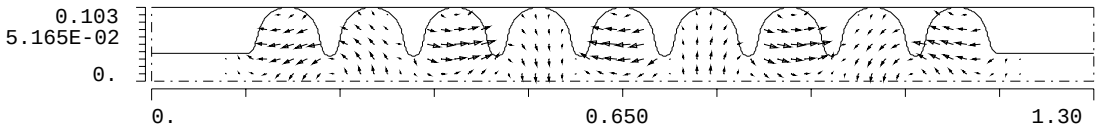

Figure 29: Electric field of the dipole mode MM-14 of a TESLA TDR-like 9-cell cavity. This mode is the mode with the largest R/Q from the second passband.

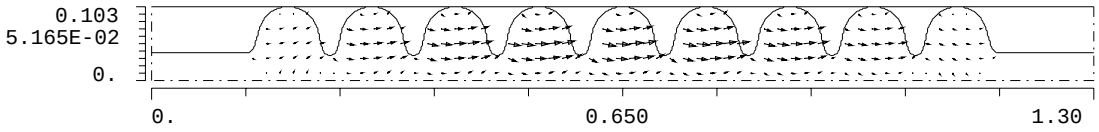

Figure 30: Electric field of the dipole mode MM-18 of a TESLA TDR-like 9-cell cavity. This is the mode with the highes frequency from the second passband.

Modes with frequencies above the beam pipe cutoff frequency are shown in Fig. 31, Fig. 33 and Fig. 34. The mode MM-30, shown in Fig. 31, belongs to the third passband. It is the mode with the largest R/Q not only of the modes of passband three but also of all calculated modes, i.e. all modes from passbands one to seven. The modes MM-42 and MM-46 belong to the fifth passband. These modes are potentially trapped in the cavity mid cells, i.e. although their frequency is above the cutoff frequency of the beam pipe they do not couple well to the beam pipe. This is obvious from Fig. 33 for mode MM-42 since there is almost no field in the cavity end-cells, but is also true for mode MM-46 which is shown in Fig. 34. The mode MM-46 is the mode with the largest R/Q from the fifth passband.

The modes may also be labeled by their phase advance per cell. The local phase advance according to equation (48) of mode MM-30 is shown in Fig. 32 as a function of the longitudinal position measured in units of the cell length g. The phase advance per cell is nearly constant (11.6°) within the center cell and is used to characterize this mode.

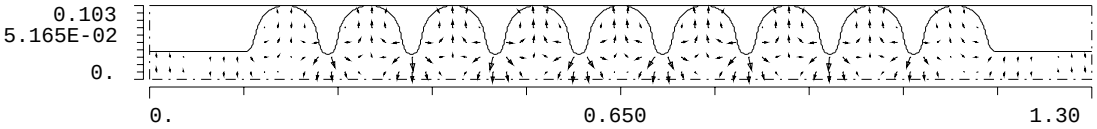

Figure 31: Electric field of the dipole mode MM-30 of a TESLA TDR-like 9-cell cavity.

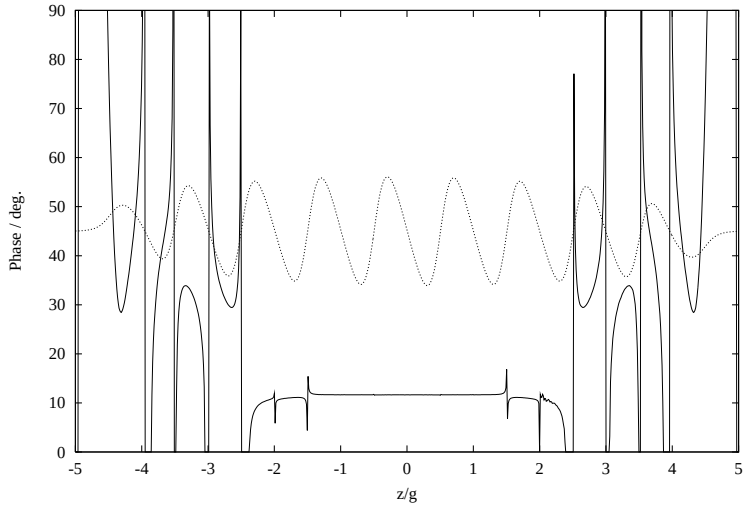

Figure 32: Phase advance per cell versus position for the mode MM-30 from the third passband (solid line) according to equation 48 and the electric field E_z of the mode (dotted line).

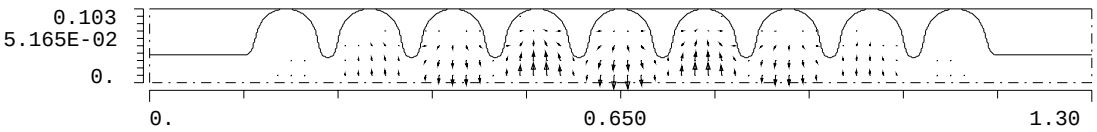

Figure 33: Electric field of the dipole mode MM-42 of a TESLA TDR-like 9-cell cavity.

Each of the modes from passbands one to seven calculated for a TDR-like TESLA 9-cell cavity with magnetic boundary conditions are represented by a diamond in the dispersion diagramm shown in Fig. 35. The modes calculated

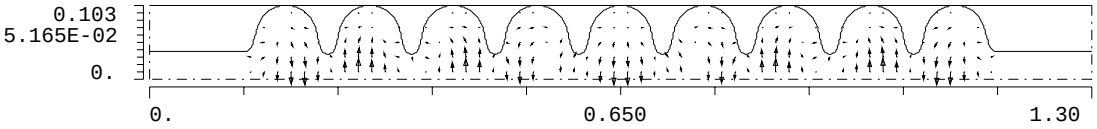

Figure 34: Electric field of the dipole mode MM-46 of a TESLA TDR-like 9-cell cavity.

with electric boundary conditions are represented by a cross. The electric field pattern is nearly independent from the boundary conditions if the diamonds and

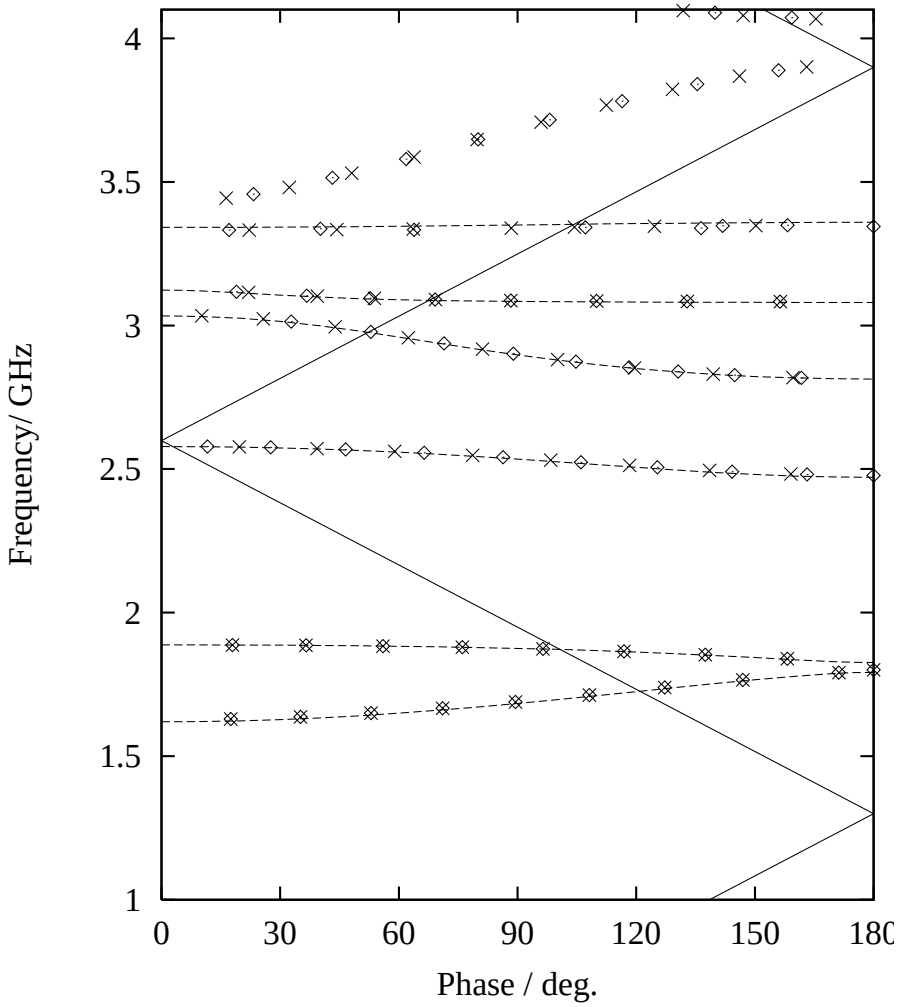

Figure 35: Dispersion curves for dipole (dashed line, lowest 6 bands) and the dipole modes in a 9-cell cavity. The diamonds represent the modes calculated with magnetic (MM) boundary conditions and the crosses represent the modes calculated with electric (EE) boundary conditions.

the crosses coincidence. This is the case for the modes in the frist two passbands with frequencies below the cutoff frequency of the beam pipe and several trapped modes of the fith passband. A complete list of all modes and their basic rf-parameters is compiled in tables 8, 9, 10, 11, 12 and 13.

mode	f /GHz	$k^{(1)}(r)/r^2/$ V/(pC m^2)	G_1 /Ω	$(R/Q)^{(1)}$ / Ω/cm^2	$Q_0/Q_{0\,FM}$	φ /°
Band 1						
MM- 1	1.6291	0.1	286.7	0.0014	0.715	17.5
MM- 2	1.6369	3.3	290.5	0.0636	0.717	35.1
MM- 3	1.6497	0.1	296.6	0.0015	0.721	53.0
MM- 4	1.6671	19.7	304.4	0.3767	0.725	71.1
MM- 5	1.6885	3.6	313.2	0.0684	0.727	89.4
MM- 6	1.7129	297.8	322.1	**5.5335**	0.726	108.1
MM- 7	1.7391	425.4	329.5	**7.7852**	0.721	127.2
MM- 8	1.7656	58.2	332.7	1.0492	0.706	146.9
MM- 9	1.7912	45.3	332.4	0.8045	0.685	171.2
MM-10	1.8004	20.0	299.0	0.3542	0.610	180.0
Band 2						
MM-11	1.8391	14.1	433.0	0.2433	0.847	158.2
MM-12	1.8535	7.7	409.5	0.1327	0.789	137.5
MM-13	1.8650	186.5	401.4	**3.1825**	0.763	116.9
MM-14	1.8736	264.2	397.3	**4.4887**	0.749	96.4
MM-15	1.8795	62.0	394.7	1.0501	0.739	76.0
MM-16	1.8834	1.2	392.9	0.0210	0.733	56.0
MM-17	1.8858	4.8	391.8	0.0808	0.729	36.5
MM-18	1.8871	0.1	391.2	0.0015	0.727	18.0
MM-19	2.2884	4.8	265.1	0.0664	0.335	—
MM-20	2.2884	0.7	265.1	0.0104	0.335	—
Band 3						
MM-21	2.4778	1.5	484.0	0.0190	0.522	180.0
MM-22	2.4810	5.2	452.4	0.0664	0.486	163.2
MM-23	2.4911	2.8	453.3	0.0353	0.483	144.2
MM-24	2.5062	2.2	446.6	0.0278	0.470	125.3
MM-25	2.5239	1.7	433.7	0.0220	0.450	106.0
MM-26	2.5415	1.2	417.3	0.0156	0.427	86.4
MM-27	2.5568	0.1	401.3	0.0017	0.406	66.4
MM-28	2.5682	10.2	388.6	0.1263	0.390	46.5
MM-29	2.5753	8.5	380.4	0.1045	0.379	27.6
MM-30	2.5785	1066.0	376.5	**13.1601**	0.375	11.6

Table 8: List of dipole modes in a 9-cell TDR-like TESLA cavity, 1st, 2nd and 3rd passbands.

mode	f /GHz	$k^{(1)}(r)/r^2/$ V/(pC m^2)	G_1 /Ω	$(R/Q)^{(1)}$ / Ω/cm^2	$Q_0/Q_{0\,FM}$	φ /°	
Band 4							
MM-31	2.8177	1.4	427.8	0.0161	0.356	161.7	
MM-32	2.8269	5.1	434.0	0.0577	0.359	144.9	
MM-33	2.8394	26.2	442.6	0.2939	0.363	130.6	
MM-34	2.8540	5.1	461.9	0.0566	0.375	118.2	
MM-35	2.8737	41.2	499.2	0.4568	0.400	104.8	
MM-36	2.9019	0.7	550.3	0.0078	0.432	88.9	
MM-37	2.9378	29.3	609.8	0.3170	0.467	71.4	
MM-38	2.9774	33.7	674.5	0.3603	0.503	52.9	
MM-39	3.0137	49.3	738.9	0.5210	0.538	32.8	
MM-40	3.0395	0.4	790.2	0.0041	0.566	—	
MM-41	3.0427	32.9	805.7	0.3446	0.576	—	
Band 5							
MM-42	3.0833	0.0	1068.3	0.0003	0.743	156.4	t
MM-43	3.0838	0.2	1070.4	0.0025	0.745	132.8	t
MM-44	3.0849	0.4	1074.7	0.0039	0.747	109.9	t
MM-45	3.0868	12.7	1082.0	0.1313	0.751	88.3	t
MM-46	3.0900	55.0	1093.6	0.5661	0.758	69.1	t
MM-47	3.0950	56.9	1115.2	0.5849	0.770	52.8	
MM-48	3.1038	1.8	1156.9	0.0180	0.794	36.7	
MM-49	3.1174	1.4	1217.8	0.0141	0.829	18.9	
Band 6							
MM-50	3.3321	0.1	582.3	0.0007	0.347	17.1	
MM-51	3.3333	0.0	583.7	0.0000	0.348	63.9	
MM-52	3.3366	0.6	587.5	0.0054	0.349	40.2	
MM-53	3.3386	2.1	585.2	0.0198	0.347	136.4	
MM-54	3.3418	8.4	588.2	0.0796	0.348	107.2	
MM-55	3.3447	11.1	588.7	0.1060	0.348	180.0	
MM-56	3.3472	0.9	589.1	0.0088	0.348	141.8	
MM-57	3.3488	3.9	595.7	0.0368	0.351	158.2	

Table 9: List of dipole modes in a 9-cell TDR-like TESLA cavity, 4th, 5th and 6th passbands. Some modes of this passband, marked by a t, are potentially trapped.

mode	f /GHz	$k^{(1)}(r)/r^2/$ V/(pC m^2)	G_1 /Ω	$(R/Q)^{(1)}$ / Ω/cm^2	Q_0/Q_{0FM}	φ /°
MM-58	3.3624	0.0	753.0	0.0004	0.441	—
MM-59	3.3641	9.9	755.9	0.0941	0.442	—
Band 7						
MM-60	3.4572	0.8	941.3	0.0072	0.521	23.2
MM-61	3.5140	0.0	983.9	0.0002	0.527	43.2
MM-62	3.5797	0.2	1023.9	0.0020	0.529	61.8
MM-63	3.6482	0.3	1055.8	0.0024	0.525	80.0
MM-64	3.7163	0.1	1079.2	0.0007	0.517	98.1
MM-65	3.7813	0.2	1095.8	0.0017	0.507	116.4
MM-66	3.8405	3.3	1112.2	0.0275	0.499	135.4
MM-67	3.8890	33.5	1151.4	0.2739	0.504	155.9
MM-68	3.9643	18.5	985.2	0.1485	0.415	—
MM-69	3.9658	18.9	1002.5	0.1517	0.422	—
MM-70	4.0720	33.1	653.3	0.2586	0.261	159.3
MM-71	4.0891	47.1	671.9	0.3665	0.266	139.9
MM-72	4.1075	8.8	681.5	0.0685	0.267	121.5
MM-73	4.1269	0.8	689.9	0.0061	0.268	106.3
MM-74	4.1447	4.5	698.2	0.0349	0.269	87.1
MM-75	4.1709	23.0	820.4	0.1755	0.312	76.5

Table 10: List of dipole modes in a 9-cell TDR-like TESLA cavity, 7th passbands and modes above the 7th passband.

mode	f /GHz	$k^{(1)}(r)/r^2/$ V/(pC m^2)	G_1 /Ω	$(R/Q)^{(1)}$ / Ω/cm^2	$Q_0/Q_{0\,FM}$	φ /°
Band 1						
EE- 1	1.6291	0.1	286.7	0.0014	0.715	17.5
EE- 2	1.6369	3.3	290.5	0.0636	0.717	35.2
EE- 3	1.6497	0.1	296.6	0.0014	0.721	53.0
EE- 4	1.6671	19.7	304.4	0.3767	0.725	71.1
EE- 5	1.6885	3.7	313.3	0.0689	0.727	89.5
EE- 6	1.7129	298.1	322.1	**5.5392**	0.726	108.1
EE- 7	1.7392	425.2	329.5	**7.7817**	0.721	127.2
EE- 8	1.7656	58.0	332.8	1.0453	0.706	146.9
EE- 9	1.7912	45.4	332.6	0.8059	0.686	171.2
EE-10	1.8005	20.0	299.1	0.3536	0.610	180.0
Band 2						
EE-11	1.8391	14.1	433.0	0.2434	0.847	158.2
EE-12	1.8535	7.7	409.5	0.1328	0.789	137.5
EE-13	1.8650	186.6	401.4	**3.1840**	0.763	116.9
EE-14	1.8736	264.2	397.3	**4.4893**	0.749	96.4
EE-15	1.8795	61.9	394.7	1.0492	0.739	76.0
EE-16	1.8834	1.2	392.9	0.0211	0.733	56.0
EE-17	1.8858	4.8	391.8	0.0808	0.729	36.5
EE-18	1.8871	0.1	391.2	0.0015	0.727	18.0
EE-19	2.3771	12.9	316.2	0.1728	0.370	—
EE-20	2.3771	3.3	316.2	0.0448	0.370	—
Band 3						
EE-21	2.4826	0.3	515.9	0.0035	0.554	159.1
EE-22	2.4952	0.4	496.2	0.0047	0.527	138.5
EE-23	2.5125	2.9	471.1	0.0368	0.494	118.3
EE-24	2.5309	6.0	444.9	0.0753	0.459	98.4
EE-25	2.5478	8.5	420.8	0.1063	0.429	78.6
EE-26	2.5615	58.1	401.1	0.7225	0.404	59.0
EE-27	2.5714	18.3	386.8	0.2264	0.387	39.3
EE-28	2.5772	913.5	378.3	**11.2826**	0.377	19.7
EE-29	2.6793	103.9	388.6	**1.2349**	0.358	—
EE-30	2.6793	81.7	388.6	0.9707	0.358	—

Table 11: List of dipole modes in a 9-cell TDR-like TESLA cavity, 1st and 2nd passbands, electric boundary conditions at both ends.

mode	f /GHz	$k^{(1)}(r)/r^2/$ V/(pC m^2)	G_1 /Ω	$(R/Q)^{(1)}$ / Ω/cm^2	$Q_0/Q_{0\,FM}$	φ /°	
Band 4							
EE-31	2.8185	0.0	430.6	0.0000	0.359	159.6	
EE-32	2.8311	0.2	447.2	0.0017	0.369	139.4	
EE-33	2.8522	0.2	475.4	0.0022	0.387	119.6	
EE-34	2.8814	0.0	514.3	0.0003	0.410	100.2	
EE-35	2.9174	1.3	561.2	0.0145	0.436	81.1	
EE-36	2.9572	41.3	611.1	0.4446	0.462	62.4	
EE-37	2.9953	115.3	660.0	1.2251	0.487	43.9	
EE-38	3.0227	0.3	712.4	0.0028	0.516	25.7	
EE-39	3.0343	10.0	771.4	0.1053	0.554	10.2	
Band 5							
EE-40	3.0833	0.0	1068.3	0.0002	0.743	156.4	t
EE-41	3.0838	0.3	1070.4	0.0029	0.745	132.9	t
EE-42	3.0849	0.3	1074.7	0.0032	0.747	110.0	t
EE-43	3.0868	13.0	1082.1	0.1336	0.751	88.3	t
EE-44	3.0900	52.9	1092.4	0.5451	0.757	69.3	t
EE-45	3.0946	56.9	1104.6	0.5848	0.763	53.8	
EE-46	3.1020	5.6	1119.4	0.0571	0.770	39.4	
EE-47	3.1150	0.5	1151.2	0.0050	0.785	22.0	
EE-48	3.1559	15.2	664.8	0.1537	0.442	—	
EE-49	3.1570	0.3	677.5	0.0031	0.450	—	
Band 6							
EE-50	3.3325	0.0	580.3	0.0000	0.346	22.2	
EE-51	3.3338	0.1	580.8	0.0009	0.346	44.3	
EE-52	3.3361	0.0	581.7	0.0003	0.346	63.6	
EE-53	3.3390	4.1	582.8	0.0390	0.346	88.4	
EE-54	3.3422	12.6	583.9	0.1196	0.346	104.4	
EE-55	3.3452	6.9	584.9	0.0656	0.346	124.6	
EE-56	3.3477	0.0	585.1	0.0000	0.345	150.2	
EE-57	3.3499	4.3	593.5	0.0406	0.350	—	
EE-58	3.3501	0.0	592.0	0.0004	0.349	—	

Table 12: List of dipole modes in a 9-cell TDR-like TESLA cavity, 3rd and 4th passbands.

mode	f /GHz	$k^{(1)}(r)/r^2/$ V/(pC m^2)	G_1 /Ω	$(R/Q)^{(1)}$ / Ω/cm^2	Q_0/Q_{0FM}	φ /°
Band 7						
EE-59	3.4435	0.2	910.0	0.0022	0.508	16.3
EE-60	3.4806	1.8	893.8	0.0160	0.488	32.3
EE-61	3.5304	1.1	891.6	0.0102	0.473	48.1
EE-62	3.5871	0.0	908.2	0.0003	0.467	63.8
EE-63	3.6472	2.3	939.1	0.0202	0.467	79.7
EE-64	3.7083	3.1	977.2	0.0262	0.470	96.0
EE-65	3.7677	0.3	1018.1	0.0021	0.474	112.4
EE-66	3.8223	1.0	1062.8	0.0080	0.481	129.2
EE-67	3.8682	0.1	1117.5	0.0008	0.494	146.1
EE-68	3.9004	59.3	1183.6	0.4841	0.515	163.1
EE-69	4.0681	16.2	641.1	0.1270	0.256	165.4
EE-70	4.0799	33.5	652.6	0.2614	0.259	147.0
EE-71	4.0967	27.0	669.8	0.2099	0.264	131.9
EE-72	4.1159	3.6	686.0	0.0276	0.268	115.3
EE-73	4.1371	6.0	710.2	0.0460	0.275	96.1
EE-74	4.1583	0.0	721.5	0.0002	0.276	68.8
EE-75	4.1848	13.9	760.2	0.1055	0.287	42.3
EE-76	4.1968	1.5	722.9	0.0117	0.272	21.7
EE-77	4.2111	8.7	829.6	0.0654	0.309	37.2
EE-78	4.2436	1.0	808.9	0.0077	0.297	59.5
EE-79	4.2856	2.8	811.3	0.0207	0.292	64.1
EE-80	4.3197	6.6	990.0	0.0485	0.351	NaN

Table 13: List of dipole modes in a 9-cell TDR-like TESLA cavity, 7th passbands.

5.2 The TESLA 9-cell cavity with TTF-like beam pipes

In this subsection the dipole modes of a TTF 9-cell cavity (shown in Fig. 36) are discussed. The distance d between two TESLA TTF-cavities is $3\,\lambda/2$. For the MAFIA calculations a 9-cell cavity with a beam pipe length $d/2 = 3\,\lambda/4$ at both ends has been simulated (see Fig. 36). Electric (EE) and magnetic (MM) boundary conditions,at both ends of the cavity, have been used. A complete list of all dipole modes of the first 6 passbands can be found in tables 14, 15, 16, 17, 18 and 19. The phase advance per cell has been calculated for most of the modes using equation (48) for z near the center of the cavity. The results are graphically presented in Fig. 42 for both choices of boundary conditions. A

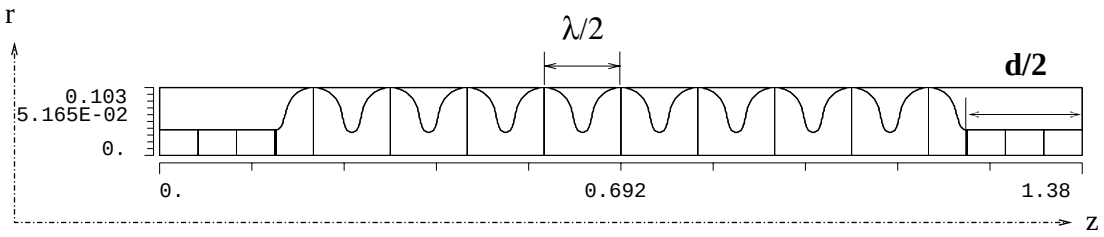

Figure 36: TESLA 9-cell TTF cavity. The distance d between the cavities is $3\,\lambda/2$ or 346.2 mm.

graphical representation of the parameter R/Q for all calculated dipole modes, using the 9-cell TESLA TDR-like and the TTF cavity, is given in Fig. 41. The modes of the TESLA TTF cavity below the cutoff frequency of the beam pipe are identical to those of the TDR-like cavity. The same is true for most of the trapped modes and many modes of the higher passbands are similar to the modes of the TDR-like TESLA cavity with respect to their field distribution and their R/Q. An important exception is found in the third dipole passband: For each choice of boundary conditions (MM and EE) there is a mode with a large R/Q in the third passband (MM-30 in table 14, EE-28 in table 17) with a frequency of about 2.58 GHz. But the R/Q of this mode in a 9-cell TESLA TTF cavity is about 15 % smaller (for magnetic boundary conditions) than that in a 9-cell TESLA TDR-like cavity. But there are two additional beam pipe modes (MM-32 in table 14 and EE-30 in table 17) with large R/Q. From the field pattern the occurrence of these modes can be interpreted as a 'longitudinal splitting' of the electric field into a mode with a large field amplitude in the center cells of the cavity and another mode with a large field amplitude in the beam pipe between the cavities. The electric field of the modes EE-28, EE-29 and EE-30 are shown in Fig. 37, 38 and 39 respectively (see also the plots of the electric field components in appendix B). These plots may be compared to the corresponding mode EE-28 of a TESLA TDR-like cavity (see Fig.40).

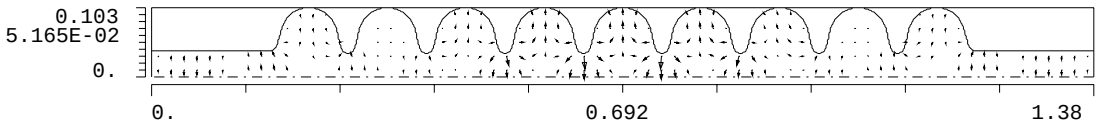

Figure 37: Electric field of the dipole mode EE-28 of a 9-cell TESLA TTF cavity ($f = 2.5745$, $(R/Q)^{(1)} = 3.64\ \Omega/\mathrm{cm}^2$).

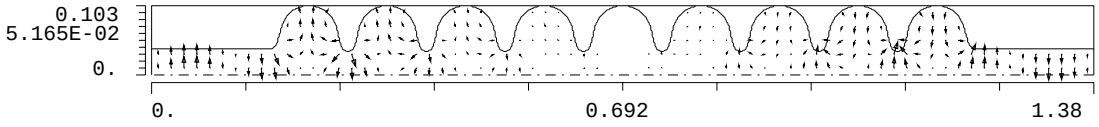

Figure 38: Electric field of the dipole mode EE-29 of a 9-cell TESLA TTF cavity ($f = 2.5832$, $(R/Q)^{(1)} \approx 0\ \Omega/\mathrm{cm}^2$).

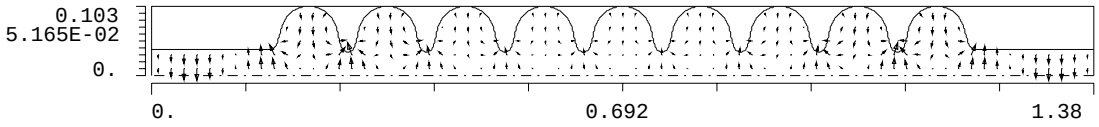

Figure 39: Electric field of the dipole mode EE-30 of a 9-cell TESLA TTF cavity ($f = 2.5836$, $(R/Q)^{(1)} = 9.3\ \Omega/\mathrm{cm}^2$).

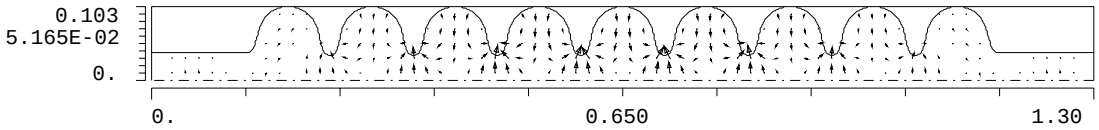

Figure 40: Electric field of the dipole mode EE-28 of a 9-cell TESLA **TDR-like** cavity ($f = 2.5772$, $(R/Q)^{(1)} = 11.28\ \Omega/\mathrm{cm}^2$).

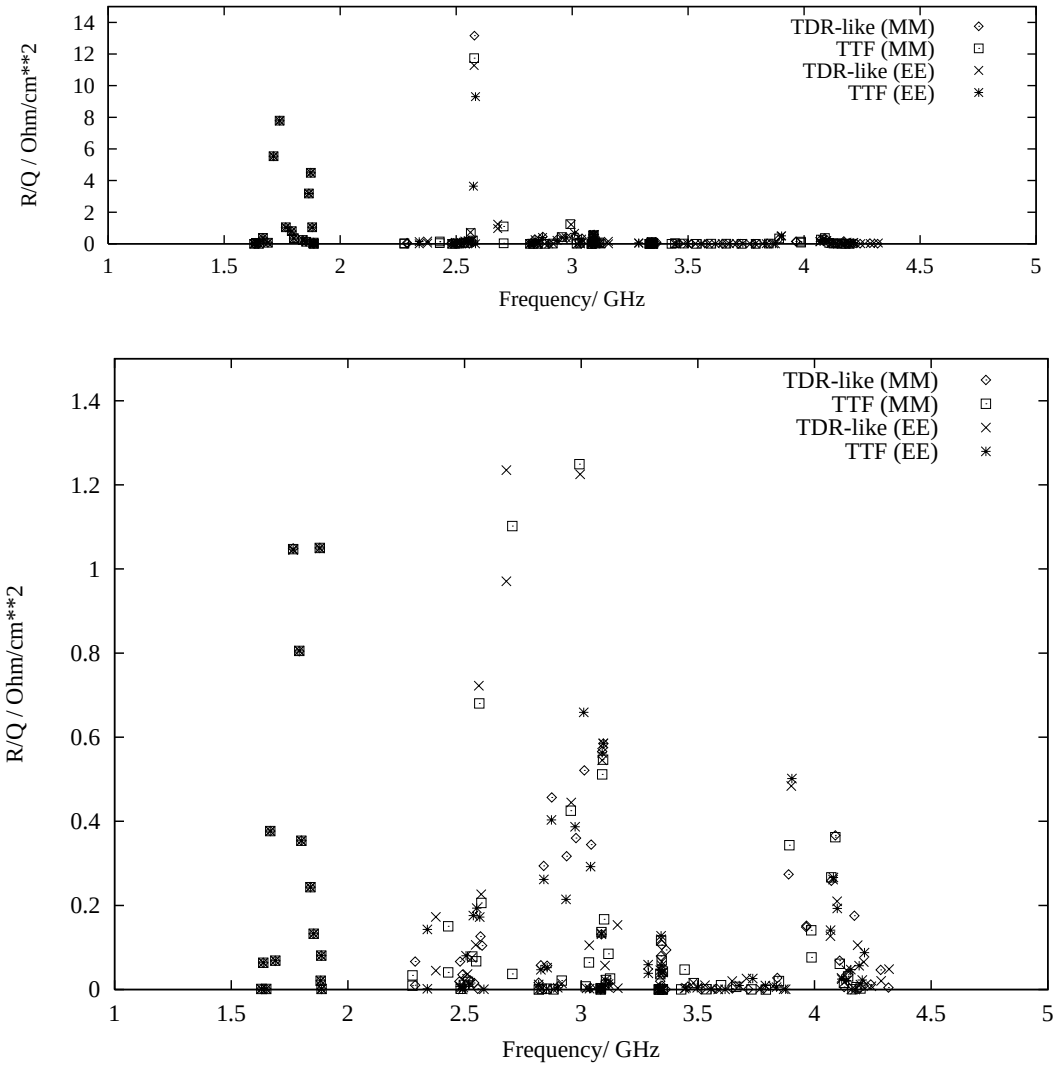

Figure 41: The parameter $(R/Q)^{(1)}$ of the dipole modes which have been calculated for the 9-cell TESLA TDR-like and the TTF cavities plotted versus the frequency of the modes. The upper plot shows all data and the lower plot only modes with an R/Q below 1.5 Ω/cm^2. The diamonds denote the dipole modes of 9-cell TESLA TDR-like cavity obtained with MM boundary conditions while the crosses correspond to EE boundary conditions. The results for a 9-cell TESLA TTF cavity with MM boundary conditions are marked by squares while the stars mark the results for EE boundary conditions.

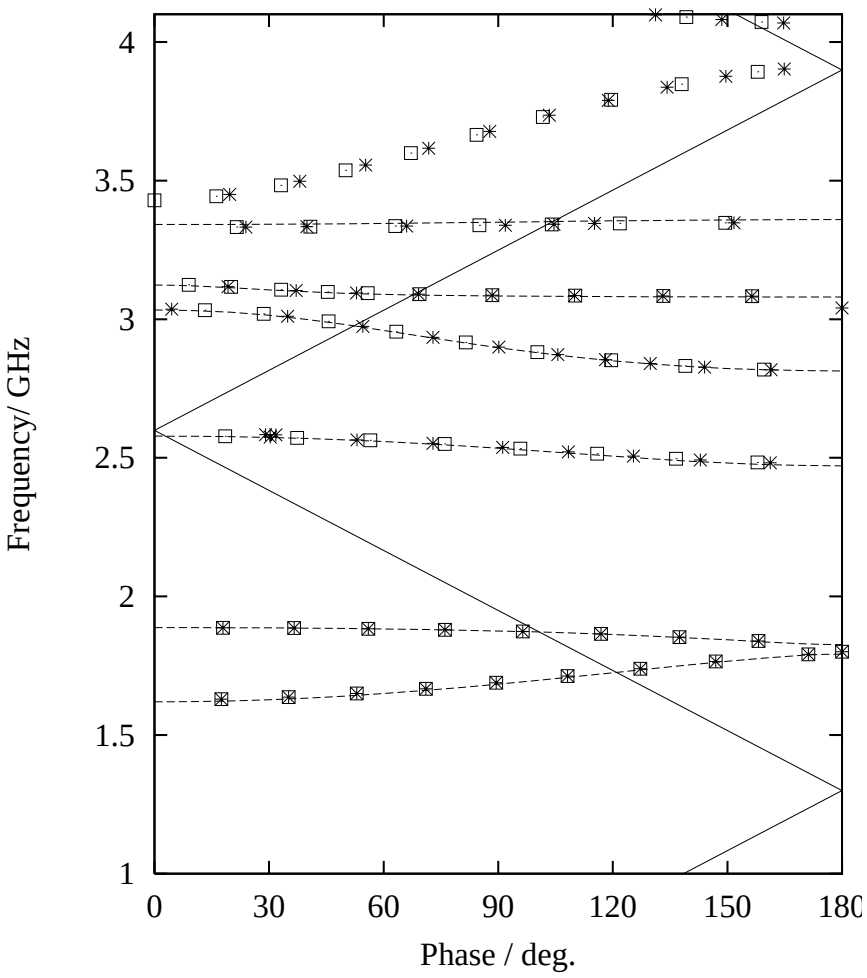

Figure 42: Dispersion curves for dipole modes (dashed line) and the dipole modes in a 9-cell TESLA TTF-cavity. The squares mark the modes obtained with MM boundary conditions while the stars correspond to those with EE boundary conditions.

mode	f /GHz	$k^{(1)}(r)/r^2/$ V/(pC m^2)	G_1 /Ω	$(R/Q)^{(1)}$ / Ω/cm^2	$Q_0/Q_{0\,FM}$	φ /°
Band 1						
MM- 1	1.6291	0.1	286.7	0.0014	0.715	17.5
MM- 2	1.6369	3.3	290.5	0.0636	0.717	35.1
MM- 3	1.6497	0.1	296.6	0.0015	0.721	53.0
MM- 4	1.6671	19.7	304.4	0.3767	0.725	71.1
MM- 5	1.6885	3.6	313.3	0.0686	0.727	89.4
MM- 6	1.7129	297.9	322.1	**5.5361**	0.726	108.1
MM- 7	1.7391	425.3	329.5	**7.7836**	0.721	127.2
MM- 8	1.7656	58.1	332.7	1.0474	0.706	146.9
MM- 9	1.7912	45.3	332.5	0.8051	0.686	171.2
MM-10	1.8004	20.0	299.0	0.3539	0.610	180.0
Band 2						
MM-11	1.8391	14.1	433.0	0.2433	0.847	158.2
MM-12	1.8535	7.7	409.5	0.1327	0.789	137.5
MM-13	1.8650	186.5	401.4	3.1832	0.763	116.9
MM-14	1.8736	264.2	397.3	**4.4889**	0.749	96.4
MM-15	1.8795	62.0	394.7	**1.0497**	0.739	76.0
MM-16	1.8834	1.2	392.9	0.0210	0.733	56.0
MM-17	1.8858	4.8	391.8	0.0808	0.729	36.6
MM-18	1.8871	0.1	391.2	0.0015	0.727	18.0
MM-19	2.2767	2.4	256.9	0.0335	0.328	—
MM-20	2.2767	0.7	256.9	0.0091	0.328	—
MM-21	2.4297	3.1	348.7	0.0407	0.391	—
MM-22	2.4297	11.5	348.6	0.1503	0.391	—
Band 3						
MM-23	2.4832	0.1	512.3	0.0017	0.550	157.9
MM-24	2.4968	0.9	488.8	0.0108	0.519	136.5
MM-25	2.5147	1.5	463.3	0.0184	0.485	115.9
MM-26	2.5333	6.2	438.5	0.0784	0.452	95.8
MM-27	2.5499	5.4	416.3	0.0673	0.424	76.0
MM-28	2.5630	54.8	398.4	0.6802	0.401	56.5
MM-29	2.5721	16.6	385.6	0.2059	0.386	37.3
MM-30	2.5774	950.7	378.0	**11.7410**	0.376	18.5
MM-31	2.7049	3.1	407.1	0.0370	0.368	—
MM-32	2.7049	93.6	407.1	**1.1019**	0.368	—

Table 14: List of dipole modes in a 9-cell TTF TESLA cavity, 1st, 2nd and 3rd passbands.

mode	f /GHz	$k^{(1)}(r)/r^2/$ V/(pC m^2)	G_1 /Ω	$(R/Q)^{(1)}$ / Ω/cm^2	$Q_0/Q_{0\,FM}$	φ /°	
Band 4							
MM-33	2.8185	0.0	430.7	0.0000	0.359	159.6	
MM-34	2.8311	0.1	447.6	0.0016	0.369	139.0	
MM-35	2.8522	0.2	475.9	0.0022	0.387	119.6	
MM-36	2.8812	0.0	514.4	0.0003	0.410	100.3	
MM-37	2.9166	2.0	559.6	0.0213	0.435	81.5	
MM-38	2.9553	39.5	605.2	0.4253	0.458	63.3	
MM-39	2.9921	117.4	647.7	1.2488	0.479	45.6	
MM-40	3.0193	0.7	698.0	0.0074	0.507	28.6	
MM-41	3.0329	6.1	765.2	0.0644	0.550	13.2	
Band 5							
MM-42	3.0833	0.0	1068.3	0.0002	0.743	156.5	t
MM-43	3.0838	0.3	1070.3	0.0032	0.745	133.3	t
MM-44	3.0849	0.3	1074.6	0.0026	0.747	110.2	t
MM-45	3.0868	13.2	1082.2	0.1365	0.751	88.5	t
MM-46	3.0900	49.7	1089.1	0.5115	0.755	69.4	
MM-47	3.0939	53.1	1055.7	0.5467	0.730	55.8	
MM-48	3.0985	16.2	957.0	0.1669	0.659	45.4	
MM-49	3.1063	2.2	841.5	0.0225	0.577	33.2	
MM-50	3.1166	8.3	799.3	0.0851	0.544	20.0	
MM-51	3.1236	2.6	985.1	0.0261	0.668	9.0	
Band 6							
MM-52	3.3325	0.0	580.3	0.0000	0.346	21.6	
MM-53	3.3338	0.1	580.9	0.0008	0.346	40.8	
MM-54	3.3360	0.0	581.7	0.0004	0.346	63.0	
MM-55	3.3390	3.8	582.8	0.0365	0.346	85.1	
MM-56	3.3422	12.2	583.9	0.1164	0.346	104.0	
MM-57	3.3452	7.3	584.9	0.0692	0.346	121.9	
MM-58	3.3476	0.0	585.3	0.0001	0.345	149.4	
MM-59	3.3498	4.5	592.9	0.0429	0.350	—	
MM-60	3.3500	0.1	591.7	0.0005	0.349	—	

Table 15: List of dipole modes in a 9-cell TTF TESLA cavity, 4th, 5th and 6th passbands.

mode	f /GHz	$k^{(1)}(r)/r^2/$ V/(pC m^2)	G_1 /Ω	$(R/Q)^{(1)}$ / Ω/cm^2	Q_0/Q_{0FM}	φ /°
Band 7						
MM-61	3.4287	0.0	849.4	0.0004	0.478	0.0
MM-62	3.4433	5.1	817.5	0.0476	0.456	16.2
MM-63	3.4828	1.6	882.2	0.0151	0.481	33.1
MM-64	3.5373	0.1	948.9	0.0006	0.502	50.1
MM-65	3.5994	1.1	1004.1	0.0101	0.513	67.1
MM-66	3.6646	0.7	1045.5	0.0064	0.515	84.3
MM-67	3.7296	0.0	1075.0	0.0002	0.511	101.7
MM-68	3.7917	0.0	1096.6	0.0000	0.505	119.5
MM-69	3.8478	2.4	1119.1	0.0202	0.500	138.0
MM-70	3.8925	42.0	1164.5	0.3432	0.508	157.9
MM-71	3.9861	17.6	935.9	0.1407	0.390	—
MM-72	3.9870	9.6	947.7	0.0764	0.394	—
MM-73	4.0723	34.1	655.6	0.2669	0.262	158.9
MM-74	4.0896	46.5	675.2	0.3621	0.267	139.2
MM-75	4.1082	7.9	684.4	0.0612	0.268	121.0
MM-76	4.1264	2.0	689.3	0.0157	0.268	103.6
MM-77	4.1444	4.0	694.9	0.0310	0.268	86.4
MM-78	4.1624	0.1	702.0	0.0006	0.268	68.6
MM-79	4.1801	0.7	708.2	0.0055	0.268	50.0
MM-80	4.1969	0.3	707.9	0.0026	0.266	30.7

Table 16: List of dipole modes in a 9-cell TTF TESLA cavity, 7th and higher passbands.

mode	f /GHz	$k^{(1)}(r)/r^2/$ V/(pC m^2)	G_1 /Ω	$(R/Q)^{(1)}$ / Ω/cm^2	$Q_0/Q_{0\,FM}$	φ /°
Band 1						
EE- 1	1.6291	0.1	286.7	0.0014	0.715	17.5
EE- 2	1.6369	3.3	290.5	0.0636	0.717	35.1
EE- 3	1.6497	0.1	296.6	0.0015	0.721	53.0
EE- 4	1.6671	19.7	304.4	0.3767	0.725	71.1
EE- 5	1.6885	3.6	313.3	0.0686	0.727	89.4
EE- 6	1.7129	297.9	322.1	**5.5366**	0.726	108.1
EE- 7	1.7391	425.3	329.5	**7.7833**	0.721	127.2
EE- 8	1.7656	58.1	332.7	1.0471	0.706	146.9
EE- 9	1.7912	45.3	332.5	0.8053	0.686	171.2
EE-10	1.8004	20.0	299.0	0.3539	0.610	180.0
Band 2						
EE-11	1.8391	14.1	433.0	0.2433	0.847	158.2
EE-12	1.8535	7.7	409.5	0.1327	0.789	137.5
EE-13	1.8650	186.5	401.4	**3.1833**	0.763	116.9
EE-14	1.8736	264.2	397.3	**4.4890**	0.749	96.4
EE-15	1.8795	62.0	394.7	1.0496	0.739	76.0
EE-16	1.8834	1.2	392.9	0.0210	0.733	56.0
EE-17	1.8858	4.8	391.8	0.0808	0.729	36.6
EE-18	1.8871	0.1	391.2	0.0015	0.727	18.0
EE-19	2.3408	10.5	289.3	0.1429	0.349	—
EE-20	2.3408	0.1	289.3	0.0017	0.349	—
Band 3						
EE-21	2.4818	0.5	515.5	0.0069	0.554	161.2
EE-22	2.4920	0.0	494.1	0.0003	0.526	142.9
EE-23	2.5061	6.3	466.6	0.0804	0.491	125.4
EE-24	2.5217	1.0	440.1	0.0127	0.458	108.3
EE-25	2.5374	14.0	418.4	0.1760	0.430	91.1
EE-26	2.5522	15.5	401.5	0.1935	0.408	72.9
EE-27	2.5649	13.9	388.3	0.1722	0.390	53.0
EE-28	2.5745	294.7	378.9	**3.6442**	0.378	30.3
EE-29	2.5832	0.1	367.1	0.0008	0.364	—
EE-30	2.5836	755.0	367.2	**9.3025**	0.364	—

Table 17: List of dipole modes in a 9-cell TTF TESLA cavity, 1st, 2nd and 3rd passbands.

mode	f /GHz	$k^{(1)}(r)/r^2/$ V/(pC m^2)	G_1 /Ω	$(R/Q)^{(1)}$ / Ω/cm^2	$Q_0/Q_{0\,FM}$	φ /°	
Band 4							
EE-31	2.8178	1.1	427.8	0.0121	0.356	161.4	
EE-32	2.8274	4.2	432.6	0.0472	0.358	144.0	
EE-33	2.8402	23.4	435.1	0.2618	0.357	129.8	
EE-34	2.8541	4.7	446.1	0.0519	0.362	118.1	
EE-35	2.8724	36.4	479.8	0.4034	0.385	105.6	
EE-36	2.8994	0.4	531.4	0.0043	0.418	90.2	
EE-37	2.9346	19.8	590.5	0.2144	0.454	72.9	
EE-38	2.9740	36.2	653.7	0.3871	0.489	54.5	
EE-39	3.0107	62.3	716.7	0.6592	0.523	34.9	
EE-40	3.0359	0.2	763.0	0.0022	0.548	4.5	
EE-41	3.0404	27.9	789.5	0.2922	0.565	0.0	
Band 5							
EE-42	3.0833	0.0	1068.3	0.0003	0.743	156.4	t
EE-43	3.0838	0.2	1070.4	0.0026	0.745	133.1	t
EE-44	3.0849	0.4	1074.7	0.0038	0.747	110.0	t
EE-45	3.0868	12.8	1082.0	0.1317	0.751	88.4	t
EE-46	3.0900	54.6	1093.4	0.5629	0.758	69.2	t
EE-47	3.0950	56.9	1113.9	0.5856	0.769	52.9	
EE-48	3.1035	2.2	1153.0	0.0223	0.792	37.1	
EE-49	3.1172	1.3	1213.2	0.0130	0.826	19.3	
EE-50	3.2870	6.1	647.6	0.0590	0.397	—	
EE-51	3.2874	4.0	648.4	0.0387	0.397	—	
Band 6							
EE-52	3.3326	0.0	580.4	0.0000	0.346	23.9	
EE-53	3.3340	0.2	581.2	0.0015	0.346	39.9	
EE-54	3.3363	0.0	582.0	0.0001	0.346	66.0	
EE-55	3.3392	4.8	583.1	0.0461	0.346	91.9	
EE-56	3.3424	13.4	584.2	0.1276	0.346	104.6	
EE-57	3.3453	6.1	585.0	0.0576	0.346	115.2	
EE-58	3.3477	0.0	585.0	0.0002	0.345	151.7	

Table 18: List of dipole modes in a 9-cell TTF TESLA cavity, 4th, 5th and 6th passbands.

mode	f /GHz	$k^{(1)}(r)/r^2/$ V/(pC m^2)	G_1 /Ω	$(R/Q)^{(1)}$ / Ω/cm^2	Q_0/Q_{0FM}	φ /°
EE-59	3.3502	4.3	595.1	0.0413	0.351	—
EE-60	3.3503	0.0	594.1	0.0001	0.350	—
Band 7						
EE-61	3.4498	0.4	925.1	0.0041	0.514	19.7
EE-62	3.4976	0.5	935.2	0.0044	0.506	38.1
EE-63	3.5559	0.1	942.3	0.0013	0.493	55.3
EE-64	3.6170	0.0	944.7	0.0002	0.478	71.8
EE-65	3.6776	1.1	946.2	0.0096	0.463	87.8
EE-66	3.7356	3.1	953.0	0.0262	0.452	103.4
EE-67	3.7894	1.1	972.4	0.0095	0.448	118.8
EE-68	3.8371	0.7	1013.1	0.0057	0.455	134.2
EE-69	3.8762	0.1	1082.6	0.0006	0.477	149.6
EE-70	3.9028	61.5	1172.3	0.5018	0.509	164.9
EE-71	4.0686	18.0	642.1	0.1412	0.257	164.7
EE-72	4.0808	34.1	653.8	0.2663	0.260	148.5
EE-73	4.0977	24.8	670.1	0.1928	0.264	131.2
EE-74	4.1166	3.2	686.4	0.0247	0.268	113.0
EE-75	4.1362	2.8	700.8	0.0214	0.271	94.3
EE-76	4.1557	6.2	713.3	0.0473	0.273	75.3
EE-77	4.1744	0.0	725.0	0.0001	0.275	56.2
EE-78	4.1912	7.5	738.7	0.0566	0.278	37.6
EE-79	4.2046	3.0	765.4	0.0226	0.286	21.1
EE-80	4.2140	11.6	831.5	0.0876	0.310	7.5

Table 19: List of dipole modes in a 9-cell TTF TESLA cavity, 7th and higher passbands.

5.3 Estimation of external Q-values

In this section a 9-cell TDR-like TESLA cavity with one coaxial HOM-coupler is considered. The goal is to estimate the external damping of a few selected dipole modes which can be achieved with the TESLA HOM coupler. A more detailed study of the TESLA HOM couplers can be found in [18] and a general review of HOM couplers in [19].

The cavity and the coaxial coupler are modeled on a 3-dimensional (xyz) MAFIA grid with $15 \times 27 \times 189 = 76545$ mesh points. Fig. 43 shows the electric field of a dipole mode ($f = 1.73$ GHz) from the first dipole mode passband in the plane $x = 0$ of the cavity. The center of the coaxial coupler is located 45 mm from the end-cell of the cavity. The outer conductor of the coupler has a radius of 20 mm, while the radius of the inner conductor is about 4 mm.

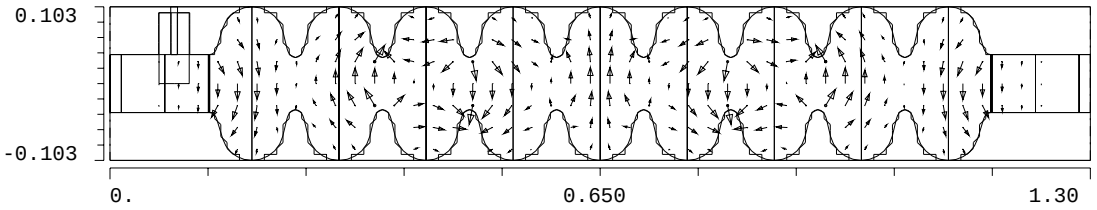

Figure 43: Electric field of a dipole mode of a 9-cell TESLA TDR-like cavity with frequency $f = 1.731$ GHz.

The method from Kroll and Yu [17] has been applied to determine the external Q-value. Several simulations with different plunger positions were performed, recording the frequency as a function of the plunger position. One cavity cell together with the coaxial coupler and the plunger is shown in Fig. 44. The beam pipe radius is chosen as a reference plane. The frequency of three dipole modes as a function of the plunger position ($L - L_{ref}$) is shown in Fig. 45. These

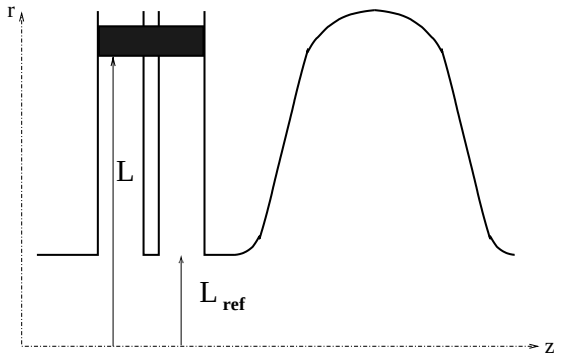

Figure 44: Schematic sketch of a coaxial coupler with a plunger and one cavity end-cell. The Kroll-Yu method is based on recording the resonance frequency as a function of the position of the plunger.

three modes are the dipole modes with the largest R/Q from the first, second and third passbands (frequencies 1.73 GHz, 1.87 GHz and 2.53 GHz). The frequencies determined in the 3D-calculations differ from those found in the 2D-calculations due to the coarser mesh in the 3D-model. The raw results shown in graphs (a)

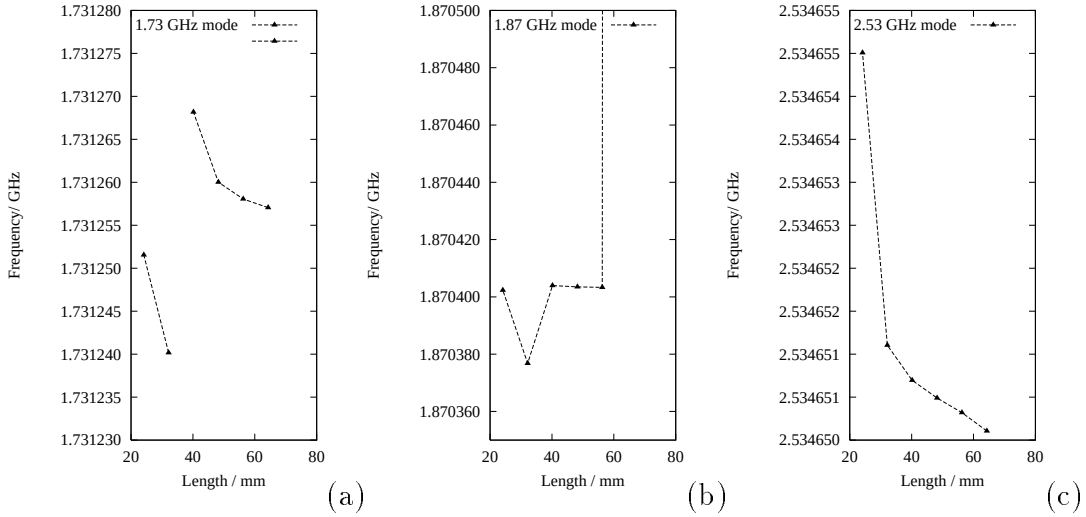

Figure 45: Variation of the mode frequency with respect to the plunger position.

and (c) of Fig. 45 appear qualitatively correct and thus can be used to compute an external Q-value while the data in graph (b) show some irregularities which make it useless for evaluations.

The phase change along the coaxial coupler can be calculated from the plunger position and the mode frequency using the following formula:

$$\psi_0(\omega) = 2\,\frac{\omega}{c}\,(L - L_{ref}) - \pi, \tag{49}$$

with $\omega = 2\,\pi\,f$. In [17] the relation between $\psi(\omega)$ and the resonance parameters Q_r, ω_r and ϕ_r is shown:

$$\psi(\omega) = -2\,\arctan\left(\frac{2\,Q_r}{\omega_r}\,(\omega - \omega_r)\right) + \phi_r. \tag{50}$$

The function $\psi(\omega)$ has been fitted through the data points $\psi_0(\omega)$ and $\omega = 2\,\pi\,f$ obtained from the MAFIA calculations. A fit through four data points from the 1.73 GHz dipole mode is shown in Fig. 46. The four squares mark the MAFIA data points which correspond to the right-most 4 data points [1] in graph (a) of Fig. 45. An external Q-value of $4.2 \cdot 10^5$ is obtained from the fit. The results are

[1] The left-most 2 data points in graph (a) belong to another branch of the curve, look also at Fig. 1a of reference [17].

summarized in table 20. The field distribution of the 2.53 GHz mode is found to be asymmetric with respect to the cavity center, with less field in the cavity cells near the coupler. This is probably due to a numerical problem and not due to the influence of the coupler. As a result an unexpectedly large external Q-value ($> 10^6$) is found.

band	f /GHz	Q_{ext}	
1	1.73	$4.2 \cdot 10^5$	
3	2.53	$3.2 \cdot 10^6$	mode is asymmetric

Table 20: External Q-values of selected dipole modes obtained using the Kroll-Yu method.

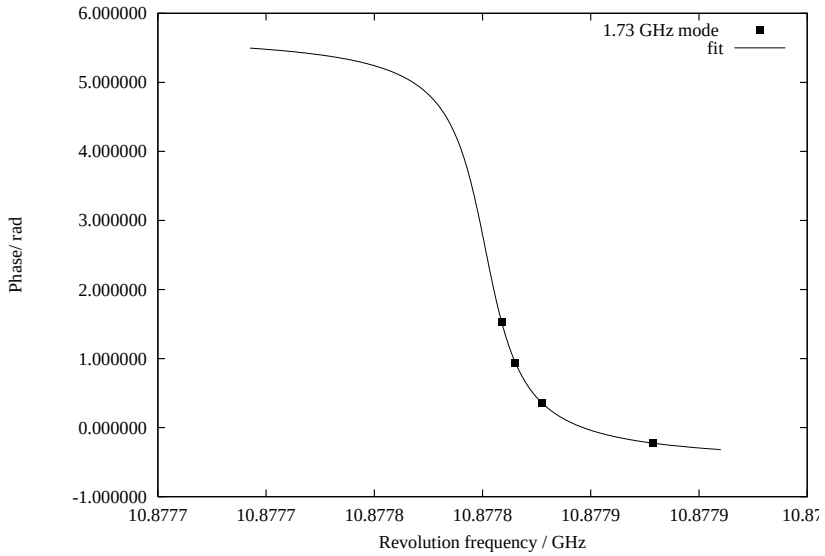

Figure 46: Application of the Kroll-Yu method to determine the external Q-value for the 1.73 GHz dipole mode. The squares mark the phase versus revolution frequency $\omega = 2\,\pi\,f$ for 4 different plunger positions, while the solid line is a fit through this data to equation (50).

6 Quadrupole modes in a TESLA 9-cell cavity

The dispersion curves of the quadrupole mode passbands one to four have been studied in section 3. This section reports the results of calculations of quadrupole modes in the 9-cell TESLA TDR-like cavity. All modes of the 1st to 4th passbands are below the cutoff frequency of TE-quadrupole modes of a beam pipe with 39 mm radius which is 3.7300 GHz. The electric field of the lowest frequency quadrupole mode is shown in Fig. 47. The mode is labeled MM-1 since magnetic (M) boundary conditions have been used. The modes in the passbands one to

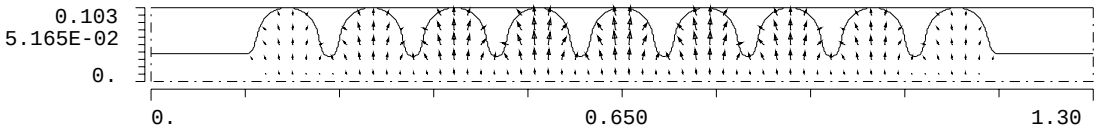

Figure 47: Electric field of the quadrupole mode MM-1 of a TESLA TDR-like 9-cell cavity. This is the quadrupole mode with the lowest frequency from the first passband of a 9-cell cavity.

four of a 9-cell TESLA TTF cavity do not differ from the modes calculated for the TDR-like cavity since the mode frequencies and the electric fields do not depend on the beam pipe.

The phase advance per cell has been calculated according to equation (48) in the center cell of the 9-cell cavity. The dispersion curves of passbands one to four and the modes of a 9-cell TESLA TDR-like cavity are shown in Fig. 49. The pentagons mark the modes calculated with magnetic (MM) boundary conditions and the crosses mark the modes calculated with electric (EE) boundary conditions. Only modes from the sixth passband (modes above the cut-off frequency of the beam pipe) are dependent on the boundary conditions . A complete list of all modes and their basic rf-parameters as calculated with magnetic (MM) boundary conditions are given in tables 21 and 22. The properties of modes EE-29 to EE-54 are given in table 23. The frequencies and rf-parameters of modes EE-1 to EE-28 are identical with the corresponding modes MM-1 to MM-28 in table 21.

The modes in each passband with the largest R/Q are those with a phase advance close to the intersection of the light cone (also shown in Fig. 49) with the dispersion curve of the corresponding mode. The mode with largest R/Q of all considered passbands is mode MM-23 (or EE-23) from the third passband ($f = 3.2532$ GHz). The electric field of this mode is shown in Fig. 48

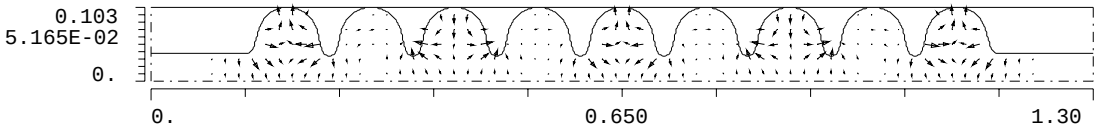

Figure 48: Electric field of the quadrupole mode MM-23 of a TESLA TDR-like 9-cell cavity.

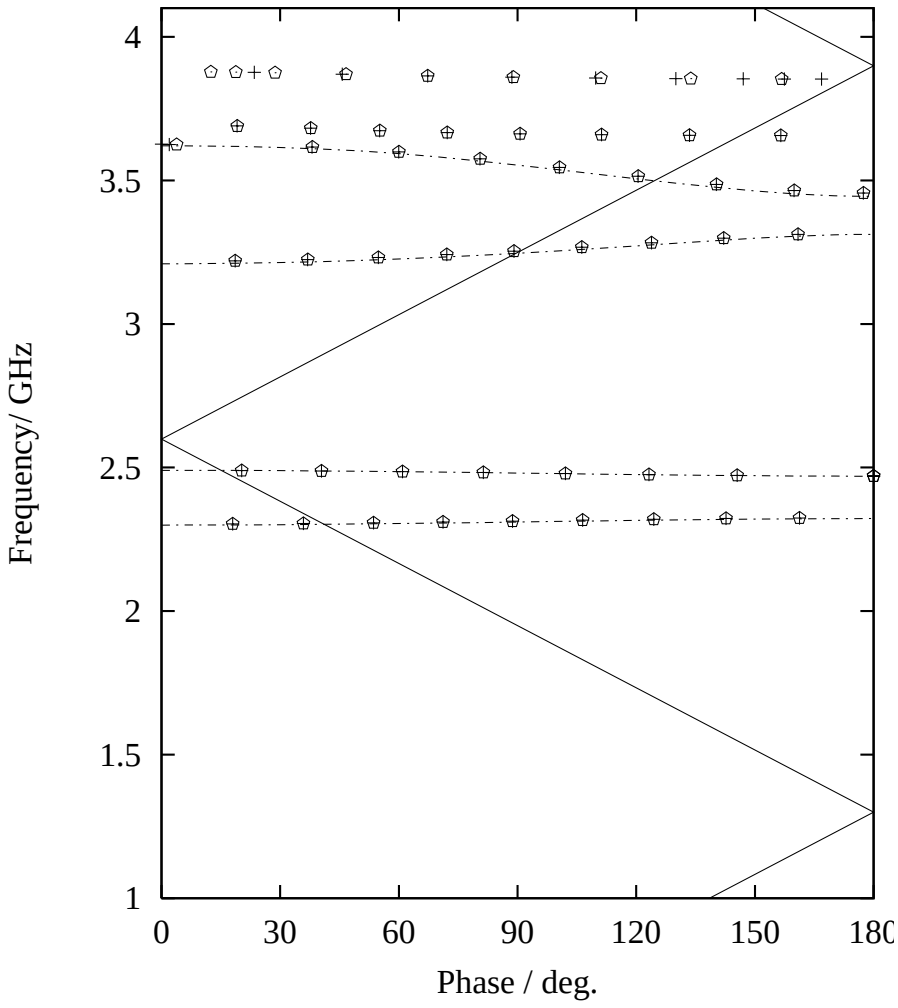

Figure 49: Dispersion curves for quadrupole modes (dash-dotted line, lowest 4 bands) and the quadrupole modes in a 9-cell cavity. The pentagons show the modes calculated with magnetic (MM) boundary conditions and the crosses show the modes calculated with electric (EE) boundary conditions.

mode	f /GHz	$k^{(2)}(r)/r^4/$ V/(pC m^4)	G_1 /Ω	$(R/Q)^{(2)}$ / Ω/cm^4	Q_0/Q_{0FM}	φ /°
Band 1						
MM- 1	2.3039	4946.0	455.6	0.0068	0.568	18.0
MM- 2	2.3052	48631.7	457.5	**0.0672**	0.570	35.9
MM- 3	2.3074	42191.1	460.5	**0.0582**	0.572	53.6
MM- 4	2.3101	1438.9	464.4	0.0020	0.576	71.2
MM- 5	2.3133	2776.0	468.9	0.0038	0.580	88.7
MM- 6	2.3166	207.5	473.7	0.0003	0.584	106.4
MM- 7	2.3197	420.9	478.6	0.0006	0.588	124.4
MM- 8	2.3224	30.8	483.0	0.0000	0.592	142.7
MM- 9	2.3242	29.1	486.1	0.0000	0.595	161.3
Band 2						
MM-10	2.4702	2.6	447.2	0.0000	0.485	180.0
MM-11	2.4706	3819.9	448.5	0.0049	0.486	180.0
MM-12	2.4727	1.2	451.5	0.0000	0.488	145.5
MM-13	2.4757	2932.4	457.0	0.0038	0.493	123.2
MM-14	2.4791	99.8	463.5	0.0001	0.499	102.1
MM-15	2.4825	5532.6	470.0	0.0071	0.505	81.3
MM-16	2.4856	979.7	476.0	0.0013	0.510	60.9
MM-17	2.4881	23777.3	480.7	0.0304	0.514	40.5
MM-18	2.4896	60355.0	483.7	**0.0772**	0.516	20.3
Band 3						
MM-19	3.2195	845.5	395.1	0.0008	0.252	18.6
MM-20	3.2242	8108.9	397.4	0.0080	0.253	37.0
MM-21	3.2316	6016.5	401.2	0.0059	0.254	54.8
MM-22	3.2414	201688.8	406.9	**0.1981**	0.256	72.1
MM-23	3.2532	453226.2	414.8	**0.4435**	0.259	89.1
MM-24	3.2670	286421.0	425.1	**0.2791**	0.263	106.2
MM-25	3.2825	35929.7	437.3	0.0348	0.269	123.8
MM-26	3.2985	4175.8	450.4	0.0040	0.274	142.1
MM-27	3.3120	4955.2	461.9	0.0048	0.279	160.9
MM-28	3.4561	32706.0	547.5	0.0301	0.303	177.5

Table 21: List of quadrupole modes in a 9-cell TDR-like TESLA cavity, 1st, 2nd and 3rd passbands, (magnetic boundaries). The parameters of the modes EE-1 to EE-28 (electric boundaries) are identical with the modes MM-1 to MM-28 of this table.

mode	f /GHz	$k^{(2)}(r)/r^4/$ V/(pC m^4)	G_1 /Ω	$(R/Q)^{(2)}$ / Ω/cm^4	Q_0/Q_{0FM}	φ /°
Band 4						
MM-29	3.4646	998.5	554.9	0.0009	0.306	159.9
MM-30	3.4860	150156.2	578.0	**0.1371**	0.315	140.3
MM-31	3.5144	70110.2	612.3	**0.0635**	0.328	120.5
MM-32	3.5452	3089.7	659.0	0.0028	0.347	100.6
MM-33	3.5748	294.3	724.8	0.0003	0.375	80.6
MM-34	3.5994	345.9	820.3	0.0003	0.419	60.0
MM-35	3.6160	575.1	940.6	0.0005	0.476	38.1
MM-36	3.6248	320.8	1026.1	0.0003	0.517	3.8
MM-37	3.6263	385.1	1063.4	0.0003	0.535	0.0
Band 5						
MM-38	3.6563	7822.6	1262.9	0.0068	0.625	156.6
MM-39	3.6572	16223.0	1252.1	0.0141	0.619	133.5
MM-40	3.6589	2476.6	1231.5	0.0022	0.609	111.2
MM-41	3.6620	2089.2	1198.7	0.0018	0.591	90.6
MM-42	3.6666	1013.0	1149.2	0.0009	0.565	72.2
MM-43	3.6733	529.7	1075.3	0.0005	0.527	55.2
MM-44	3.6817	170.3	997.8	0.0001	0.487	37.7
MM-45	3.6895	11.9	955.7	0.0000	0.464	19.2
MM-46	3.7729	581.5	348.2	0.0005	0.162	—
MM-47	3.7729	4.9	348.2	0.0000	0.162	—
Band 6						
MM-48	3.8531	96110.0	563.0	**0.0794**	0.251	156.8
MM-49	3.8541	4202.8	562.3	0.0035	0.250	133.8
MM-50	3.8561	11027.1	561.5	0.0091	0.250	111.1
MM-51	3.8592	1026.8	561.1	0.0008	0.249	89.0
MM-52	3.8638	5723.1	562.2	0.0047	0.249	67.3
MM-53	3.8695	242.0	565.7	0.0002	0.250	46.6
MM-54	3.8746	9279.9	567.1	0.0076	0.250	28.7
MM-55	3.8769	16.3	561.5	0.0000	0.247	18.8
MM-56	3.8780	5057.1	565.3	0.0042	0.249	12.5

Table 22: List of quadrupole modes in a 9-cell TDR-like TESLA cavity, 4th, 5th and 6th passbands,(magnetic boundaries).

mode	f /GHz	$k^{(2)}(r)/r^4/$ V/(pC m^4)	G_1 /Ω	$(R/Q)^{(2)}$ / Ω/cm^4	Q_0/Q_{0FM}	φ /°
Band 4						
EE-29	3.4646	1012.4	555.1	0.0009	0.306	159.9
EE-30	3.4860	150397.3	578.3	**0.1373**	0.315	140.3
EE-31	3.5144	70072.8	612.7	**0.0635**	0.328	120.5
EE-32	3.5452	3030.4	659.8	0.0027	0.347	100.6
EE-33	3.5749	291.4	725.9	0.0003	0.376	80.5
EE-34	3.5995	332.2	822.1	0.0003	0.420	60.0
EE-35	3.6160	578.4	942.8	0.0005	0.477	38.0
EE-36	3.6249	311.9	1028.7	0.0003	0.518	1.9
EE-37	3.6263	395.1	1065.0	0.0003	0.536	0.0
Band 5						
EE-38	3.6563	7822.2	1262.9	0.0068	0.625	156.6
EE-39	3.6572	16222.9	1252.1	0.0141	0.619	133.5
EE-40	3.6589	2475.5	1231.5	0.0022	0.609	111.2
EE-41	3.6620	2091.0	1198.7	0.0018	0.591	90.6
EE-42	3.6666	1005.7	1149.3	0.0009	0.566	72.2
EE-43	3.6733	536.6	1075.9	0.0005	0.528	55.1
EE-44	3.6817	163.9	998.9	0.0001	0.487	37.7
EE-45	3.6895	12.9	956.3	0.0000	0.465	19.1
Band 6						
EE-46	3.8528	50544.8	508.3	0.0418	0.227	166.9
EE-47	3.8530	1907.9	458.9	0.0016	0.204	157.4
EE-48	3.8534	45205.5	485.7	0.0373	0.216	147.1
EE-49	3.8544	2570.7	535.6	0.0021	0.239	130.0
EE-50	3.8562	14937.6	555.4	0.0123	0.247	109.7
EE-51	3.8592	993.3	560.9	0.0008	0.249	88.6
EE-52	3.8638	5259.6	561.8	0.0043	0.249	67.3
EE-53	3.8698	277.1	563.1	0.0002	0.249	45.7
EE-54	3.8759	1211.4	568.3	0.0010	0.250	23.4

Table 23: List of quadrupole modes in a 9-cell TDR-like TESLA cavity, 4th, 5th and 6th passbands, (electric boundaries).

A graphical representation of the R/Q of the quadrupole modes listed in tables 21, 22 and 23 is given in Fig. 50.

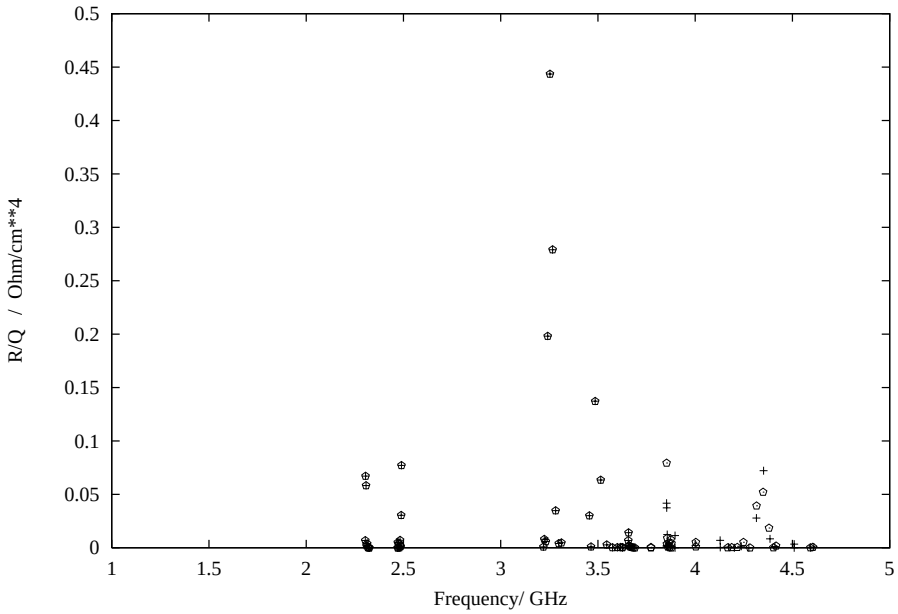

Figure 50: The parameter R/Q for quadrupole modes of a 9-cell TESLA TDR-like cavity plotted versus the frequency of the mode. The pentagons show the modes calculated with magnetic (MM) boundary conditions and the crosses show the modes calculated with electric (EE) boundary conditions.

7 Summary and conclusion

The monopole, dipole and quadrupole modes of a 9-cell TESLA TDR-like cavity have been studied. The data obtained are intended to be used in further beam dynamics studies in the TESLA linac and in the interpretation of HOM measurements at the TESLA Test Facility. It has been demonstrated that the modes of a 9-cell cavity can be classified in terms of the passband structure of a cavity mid-cell using periodic boundary conditions. The code MAFIA [6, 5] has been used to calculate the basic mode parameters including the frequency, (R/Q) and G_1 of all modes in a frequency range below 4 GHz. It is instructive to plot $(R/Q)^{(1)}$ of all dipole modes in a logarithmic representation. The quantity

$$10 \log_{10} \left(\frac{(R/Q)^{(1)}}{1\ \Omega/\mathrm{cm}^2} \right) \tag{51}$$

is plotted in Fig. 51 versus the frequency of all considered dipole modes. The

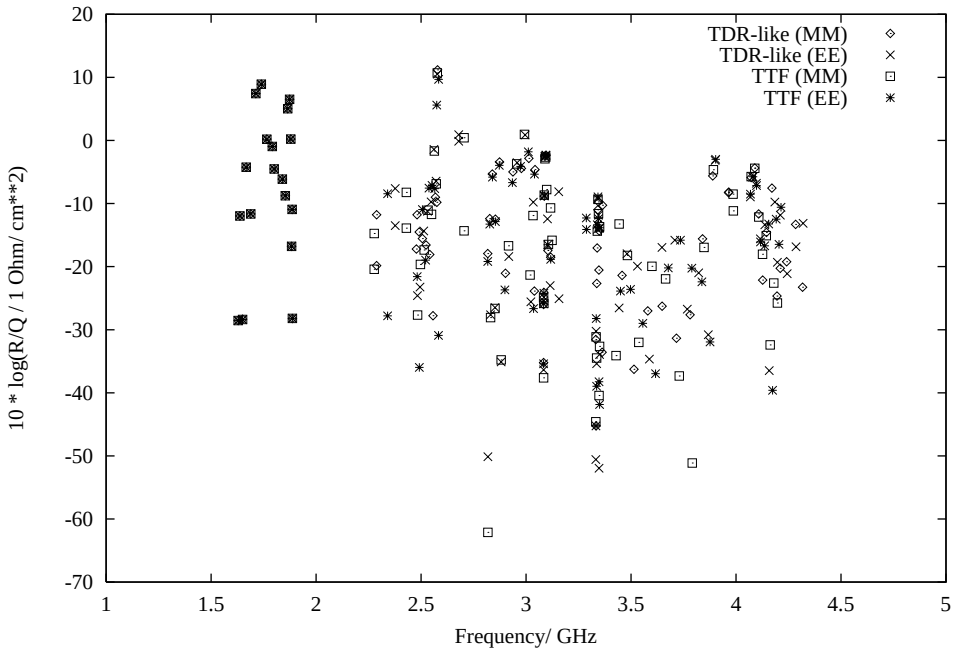

Figure 51: A logarithmic representation of the $(R/Q)^{(1)}$ versus the frequency of all calculated dipole modes is show in the figure.

modes with large (R/Q) are found in the first 3 passbands. The largest (R/Q) belongs to a mode in the 3rd passband (see also [20]). Within a passband the modes which are synchronous with the beam have the largest (R/Q). These are the modes near the intersection of the dispersion curve with the light cone. The frequency of the modes of the 3rd passband are above the cutoff frequency of the

beam pipe. These modes are in general not localized within one 9-cell cavity but are multi-cavity modes. A set of 9-cell cavities may be regarded as a biperiodic rf-structure. Fig. 52 shows the electric field of the dipole mode with frequency $f = 2.5785$ GHz from the 3rd passband in two halves of a TESLA TDR-like cavity. The field pattern is the same as that of mode MM-30 of a 9-cell cavity which is shown in Fig. 31. For the MAFIA calculations an idealized situation has been assumed with identical cavities without couplers or asymmetries in the end cells. The fabrication tolerances and couplers with a real cavity affect the field pattern and therefore the (R/Q) of the modes. A comparison between the TESLA TDR-like and the TTF cavity already demonstrates that the modes of the 3rd passband are sensitive to the inter-cavity spacing, see also the investigation in [21].

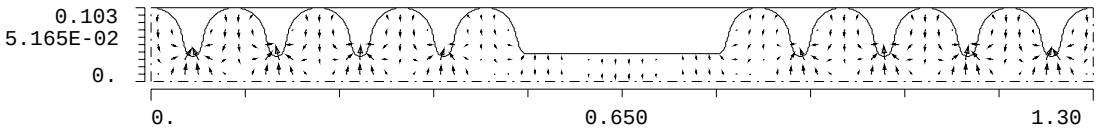

Figure 52: The electric field of the dipole mode with frequency $f = 2.5785$ GHz is shown in two halves of TESLA TDR-like cavity.

There exist trapped modes in the 5th dipole passband. Fortunately the (R/Q) of these modes are rather small. The mode with largest (R/Q) of about 0.5 Ω/cm^2 is shown in Fig. 34 and 130. One can expect that a HOM-coupler can damp this mode well because there is field in the end-cells of the cavity. A comparison of the field distribution between this trapped mode, shown in Fig. 130, and a mode below the cutoff frequency of the beam pipe, e.g. that shown in Fig. 98, indicates that less electric field of the trapped mode MM-46 leaks out into the beam than in the case of mode MM-14 from the 2nd passband. Therefore one can expect that the modes from the 5th passband have larger external Q-values than the modes from the 1st and 2nd passbands even though there is some field in the end-cells. Detailed predictions of the external Q-values is beyond the scope of these investigations. The external Q-value of one dipole mode of the first passband has been estimated to be $\sim 10^5$ using a simplified geometry for the HOM-coupler.

The $(R/Q)^{(2)}$ is small (below 0.5 Ω/cm^4) for all quadrupole modes considered. Nevertheless the effect of quadrupole modes can be larger than the effect of dipole modes if the beam transverses the cavity with a large (~ 2 cm) offset from the axis. A comparison of (R/Q) at an offset of 2 cm is shown in Fig. 53: the quantities

$$10\ \log_{10}\left(\frac{(R/Q)^{(1)}}{1\ \Omega}(2\ \mathrm{cm})^2\right) \qquad \text{and} \qquad 10\ \log_{10}\left(\frac{(R/Q)^{(2)}}{1\ \Omega}(2\ \mathrm{cm})^4\right) \tag{52}$$

are plotted for the dipole modes of a 9-cell TESLA TTF cavity (MM boundary conditions) and the quadrupoles modes listed in tables 21 and 22 (MM boundary

conditions) which have been calculated for a 9-cell TESLA TDR-like cavity (but do not depend on the beam pipe since the cutoff frequency for TE-quadrupole modes is about 3.7 GHz). In the frequency range from 3 GHz to 3.5 GHz the (R/Q) at a transverse offset of 2 cm of the quadrupole modes is larger than the (R/Q) of the dipole modes.

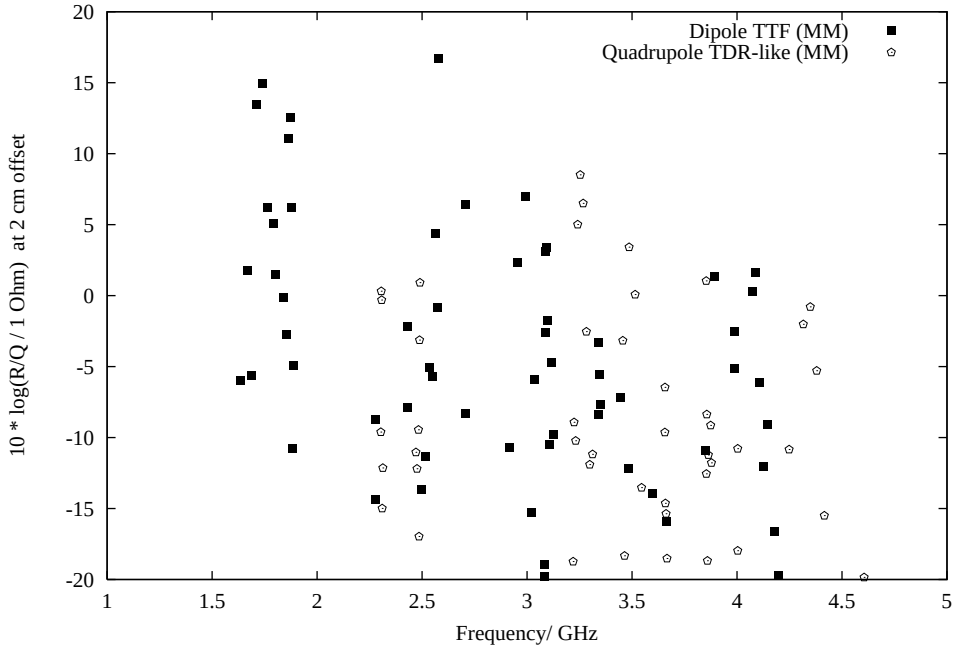

Figure 53: The (R/Q) for an offset of 2 cm of the quadrupole modes compared to the (R/Q) of the dipole modes of an 9-cell TESLA TTF cavity.

Acknowledgment

I would like to thank M. Lomperski for carefully reading the manuscript. M. Dohlus deserves special thanks for many helpful discussions.

References

[1] B. Aune *et al.*, *The superconducting TESLA cavities*, Phys. Rev. ST Accel. Beams**3** (2000) 092001 [physics/0003011].

[2] *TESLA, The Superconducting Electron-Positron Linear Collider with an Integrated X-Ray Laser Laboratory, Technical Design Report*, Part II: The Accelerator, R. Brinkmann, K. Flöttmann, J. Rossbach, P. Schmüser, N. Walker, H. Weise eds., DESY 2001-011, ECFA 2001-209, TESLA Report 2001-23, TESLA-FEL 2001-05

[3] N. Baboi, *Studies on Higher Order Modes in Accelerating Structures for Linear Colliders*, Thesis, University of Hamburg, Hamburg, April 2001

[4] C. Magne, talk given at the TTF meeting, Hamburg, May 2001

[5] T. Weiland, *On the numerical solution of Maxwell's Equations and Applications in the Field of Accelerator Physics*, Part. Acc. 15 (1984), 245-292

[6] *MAFIA Release 4 (V4.021)* CST GmbH, Büdinger Str. 2a, 64289 Darmstadt, Germany

[7] T. Weiland, *On the computation of resonant modes in cylindrically symmetric cavities*, NIM 216 (1983) 329-348

[8] T. Weiland, R. Wanzenberg, *Wake fields and impedances*, in: Joint US-CERN part. acc. school, Hilton Head Island, SC, USA, 7 - 14 Nov 1990 / Ed. by M Dienes, M Month and S Turner. - Springer, Berlin, 1992- (Lecture notes in physics ; 400) - pp.39-79

[9] T. Weiland, *Comment on wake field computation in time domain*, DESY M-83-02, Feb. 1983

[10] W.K.H. Panofsky, W.A. Wenzel, *Some consideration concerning the transverse deflection of charged particles in radio-frequency fields* , Rev. Sci. Inst. Vol 27, 11 (1956), 967

[11] P.B. Wilson *High Energy Electron Linacs: Application to Storage Ring RF Systems and Linear Colliders*, AIP Conference Proceedings 87, American Institute of Physics, New York (1982),p. 450-563

[12] D.A. Watkins *Topics in Electromagnetic Theory* , Wiley 1958, New York

[13] D.R. Lide, Ed. *Handbook of Chemistry and Physics* , 79th edition, 1998-1999, CRC Press, Washington, D.C.

[14] W.K.H. Panofsky, M. Phillips, *Classical Electricity and Magnetism*, Addison-Wesley, Reading Massachusetts 1962

[15] H. Padamsee, J. Knobloch, T. Hays, *RF Superconductivity for Accelerators*, Wiley, New York 1998

[16] M. Dohlus, private communication

[17] N.M. Kroll, D.U.L. Yu, *Computer determination of the external Q and resonant frequency of waveguide loaded cavities*, Part. Acc., 1990, Vol. 34, pp. 231-250

[18] M. Dohlus, V. Kaljuzhny, in preparation

[19] E. Haebel, *Couplers, Tutorial and Update*, Part. Acc., 1992, Vol 40, pp. 141-159

[20] S. Fartoukh et al., *Evidence for a strongly coupled dipole mode with insufficient damping in TTF first accelerating module*, Proc. of IEEE Particle Accelerator Conference (PAC 99), New York, NY, March 1999.

[21] N. Baboi, M. Dohlus, C. Magne, A. Mosnier, O. Napoly and H. W. Glock, *Investigation of a high-Q dipole mode at the TESLA cavities*, Proc. of EPAC 2000, Vienna, Austria

A Electric fields of monopole modes

A.1 TDR-like TESLA 9-cell cavity, magnetic (MM) boundary conditions.

A.1.1 Band 1

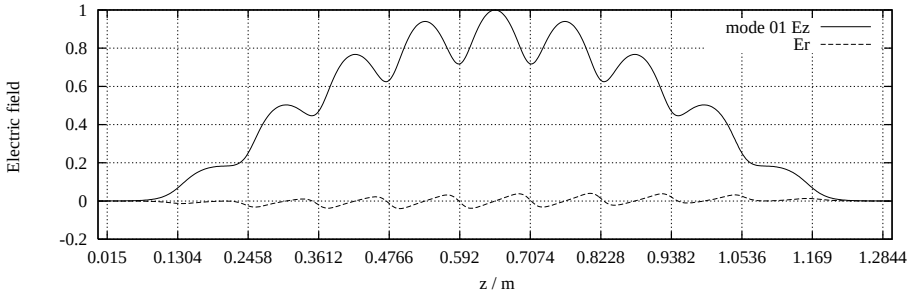

Figure 54: Electric field (E_z at $r = 0$, E_r at $r = 1$ cm) versus z of mode: MM-01

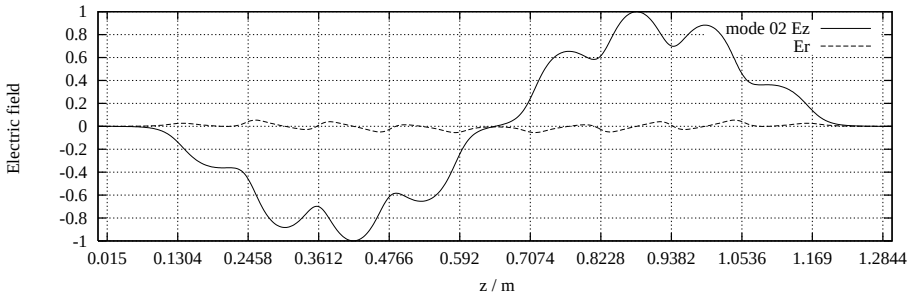

Figure 55: Electric field (E_z at $r = 0$, E_r at $r = 1$ cm) versus z of mode: MM-02

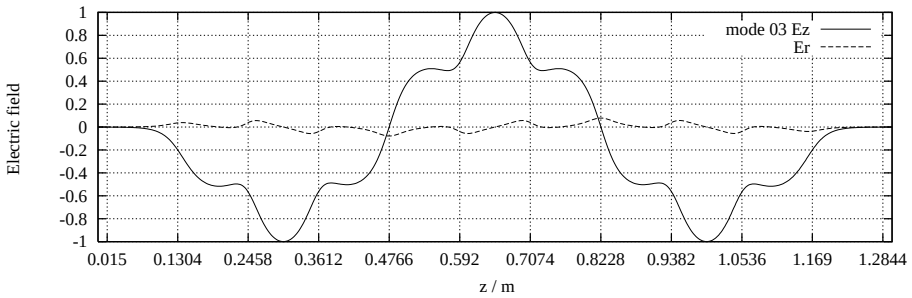

Figure 56: Electric field (E_z at $r = 0$, E_r at $r = 1$ cm) versus z of mode: MM-03

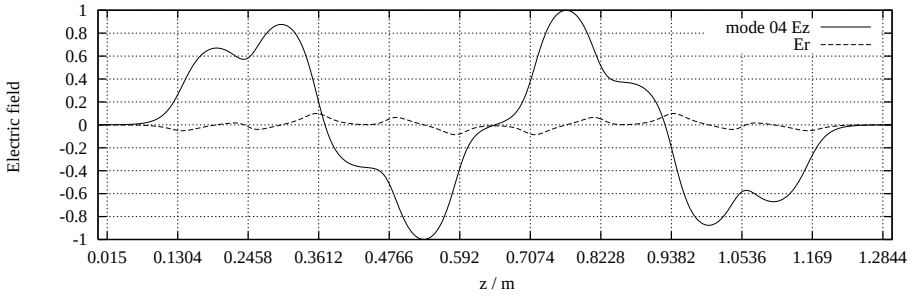

Figure 57: Electric field (E_z at $r = 0$, E_r at $r = 1$ cm) versus z of mode: MM-04

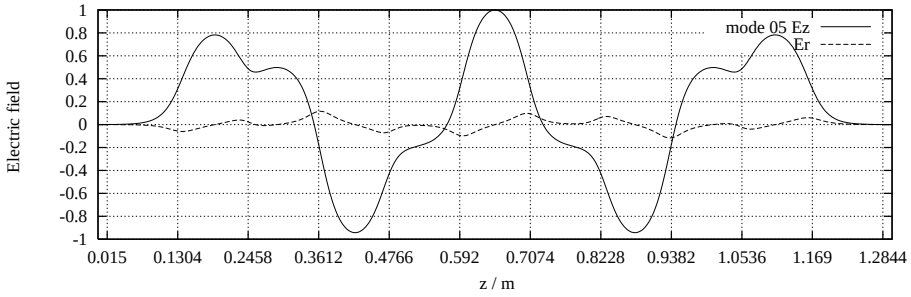

Figure 58: Electric field (E_z at $r = 0$, E_r at $r = 1$ cm) versus z of mode: MM-05

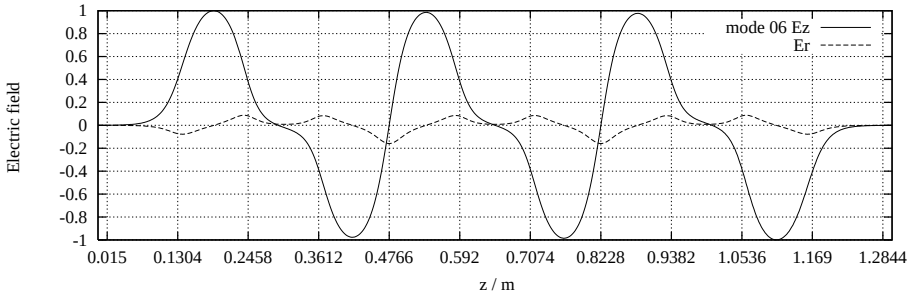

Figure 59: Electric field (E_z at $r = 0$, E_r at $r = 1$ cm) versus z of mode: MM-06

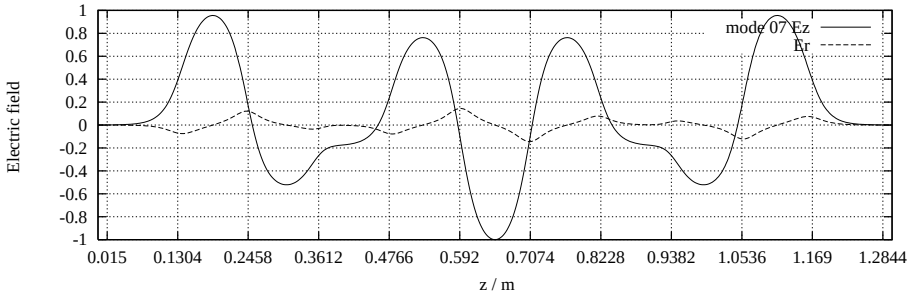

Figure 60: Electric field (E_z at $r = 0$, E_r at $r = 1$ cm) versus z of mode: MM-07

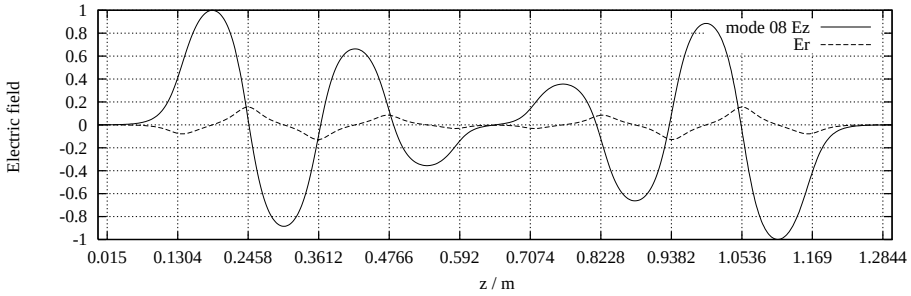

Figure 61: Electric field (E_z at $r = 0$, E_r at $r = 1$ cm) versus z of mode: MM-08

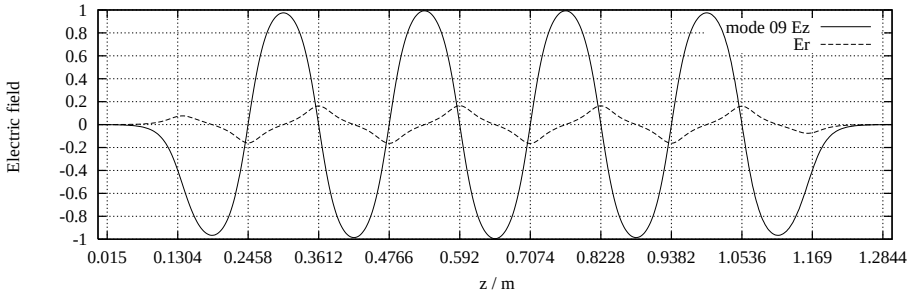

Figure 62: Electric field (E_z at $r = 0$, E_r at $r = 1$ cm) versus z of mode: MM-09

A.1.2 Band 2

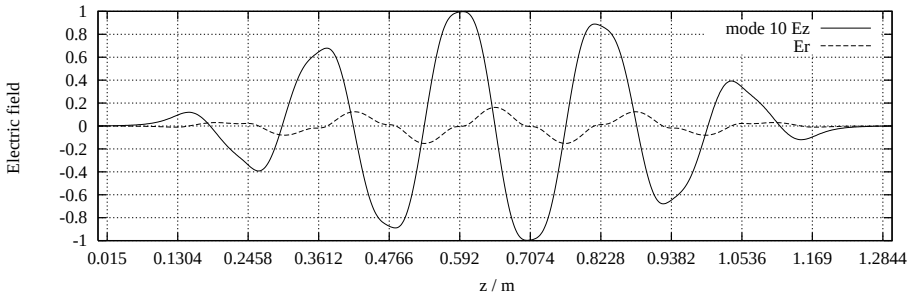

Figure 63: Electric field (E_z at $r = 0$, E_r at $r = 1$ cm) versus z of mode: MM-10

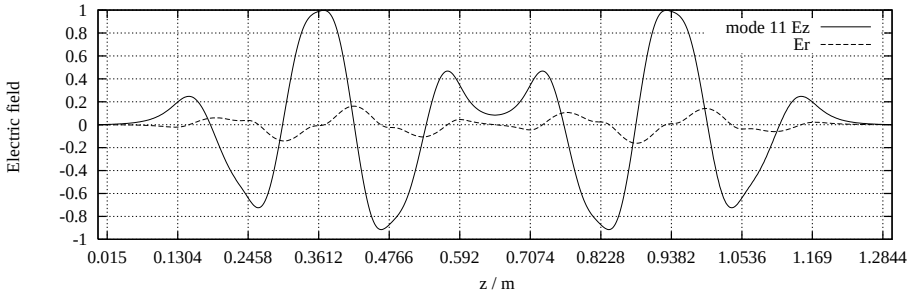

Figure 64: Electric field (E_z at $r = 0$, E_r at $r = 1$ cm) versus z of mode: MM-11

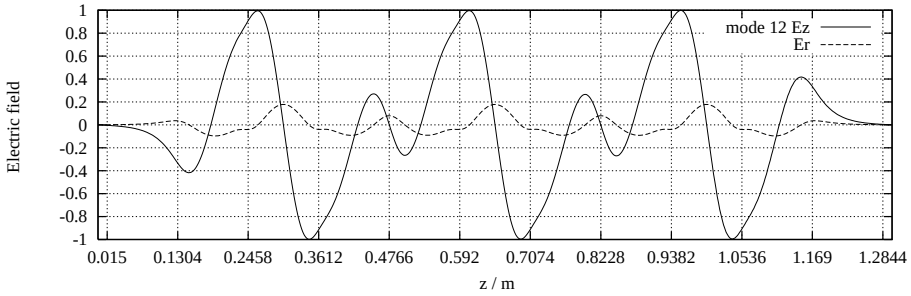

Figure 65: Electric field (E_z at $r = 0$, E_r at $r = 1$ cm) versus z of mode: MM-12

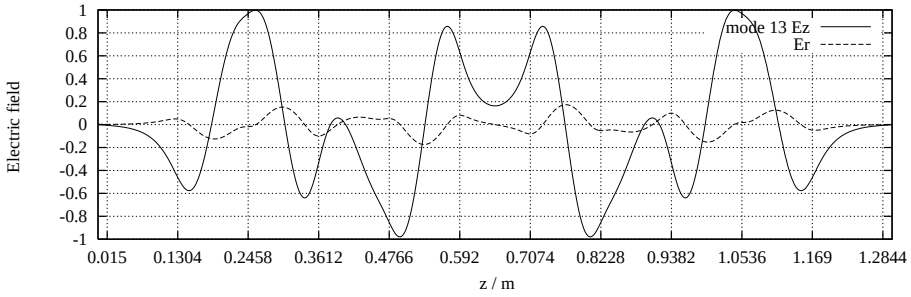

Figure 66: Electric field (E_z at $r = 0$, E_r at $r = 1$ cm) versus z of mode: MM-13

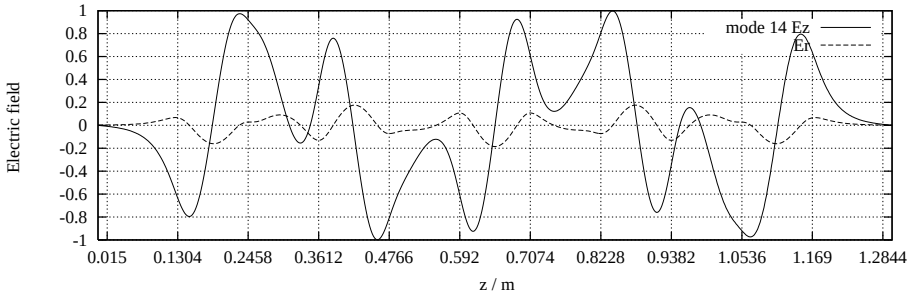

Figure 67: Electric field (E_z at $r = 0$, E_r at $r = 1$ cm) versus z of mode: MM-14

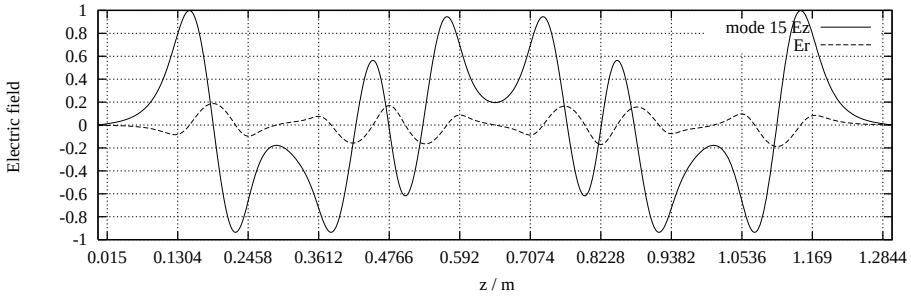

Figure 68: Electric field (E_z at $r = 0$, E_r at $r = 1$ cm) versus z of mode: MM-15

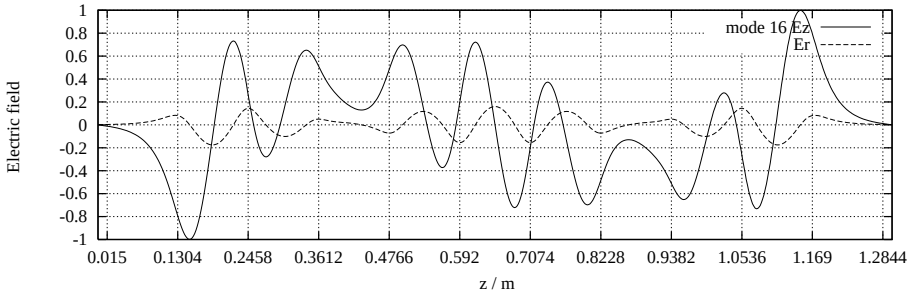

Figure 69: Electric field (E_z at $r = 0$, E_r at $r = 1$ cm) versus z of mode: MM-16

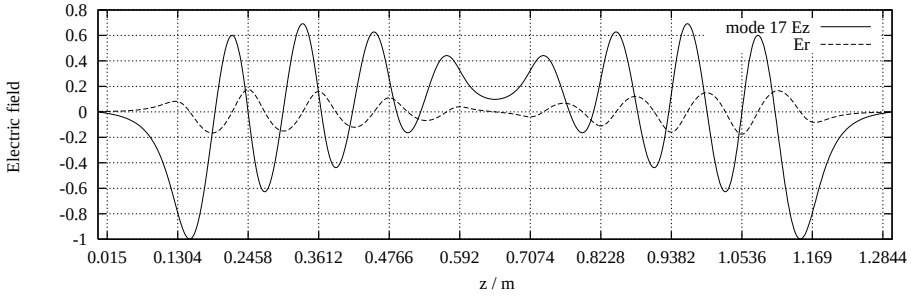

Figure 70: Electric field (E_z at $r = 0$, E_r at $r = 1$ cm) versus z of mode: MM-17

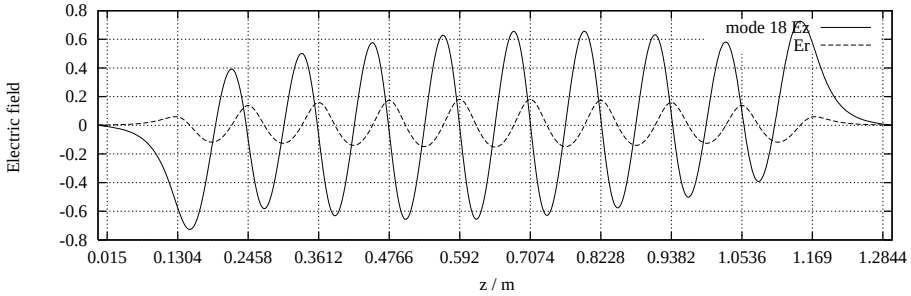

Figure 71: Electric field (E_z at $r = 0$, E_r at $r = 1$ cm) versus z of mode: MM-18

A.1.3 Band 3

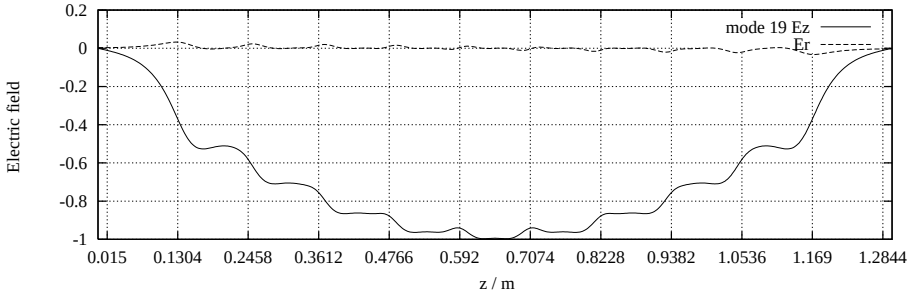

Figure 72: Electric field (E_z at $r = 0$, E_r at $r = 1$ cm) versus z of mode: MM-19

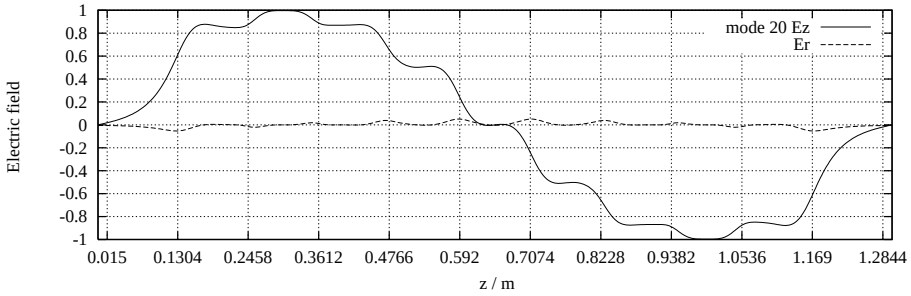

Figure 73: Electric field (E_z at $r = 0$, E_r at $r = 1$ cm) versus z of mode: MM-20

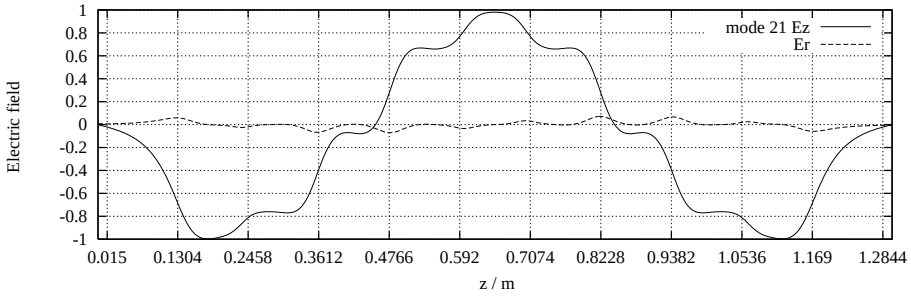

Figure 74: Electric field (E_z at $r = 0$, E_r at $r = 1$ cm) versus z of mode: MM-21

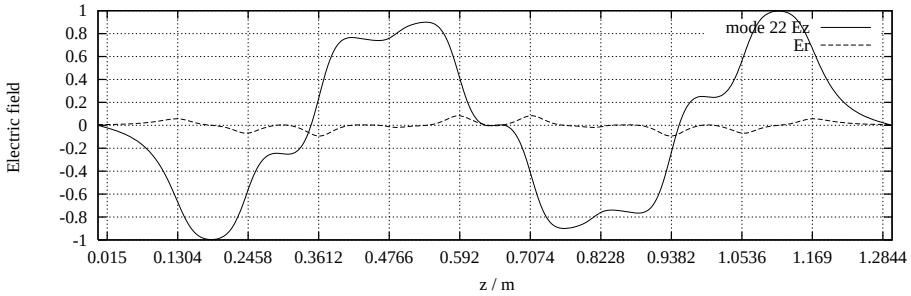

Figure 75: Electric field (E_z at $r = 0$, E_r at $r = 1$ cm) versus z of mode: MM-22

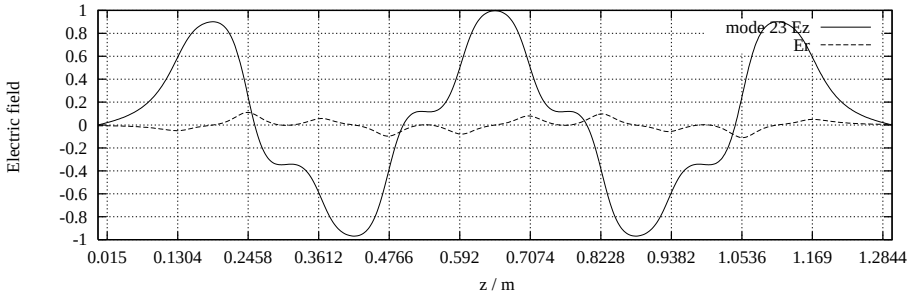

Figure 76: Electric field (E_z at $r = 0$, E_r at $r = 1$ cm) versus z of mode: MM-23

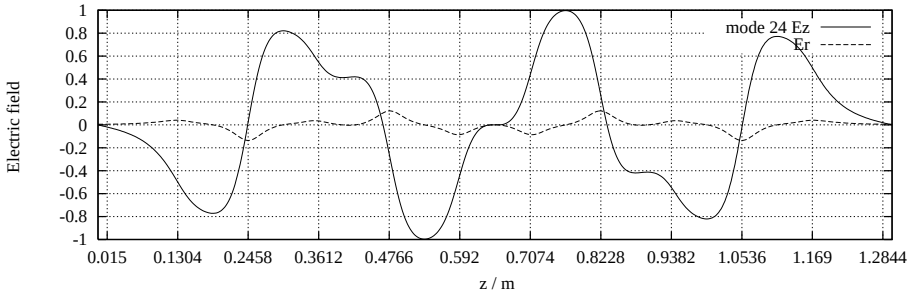

Figure 77: Electric field (E_z at $r = 0$, E_r at $r = 1$ cm) versus z of mode: MM-24

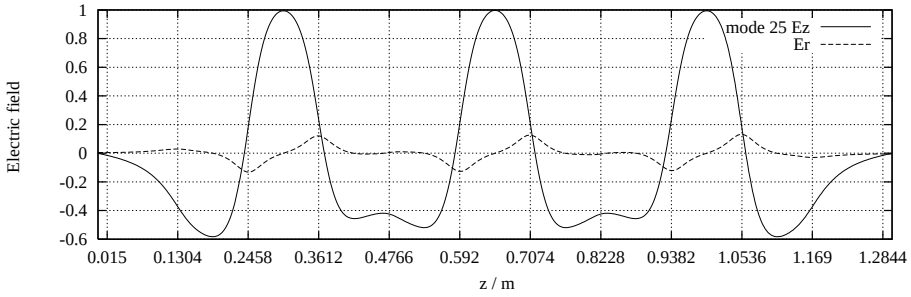

Figure 78: Electric field (E_z at $r = 0$, E_r at $r = 1$ cm) versus z of mode: MM-25

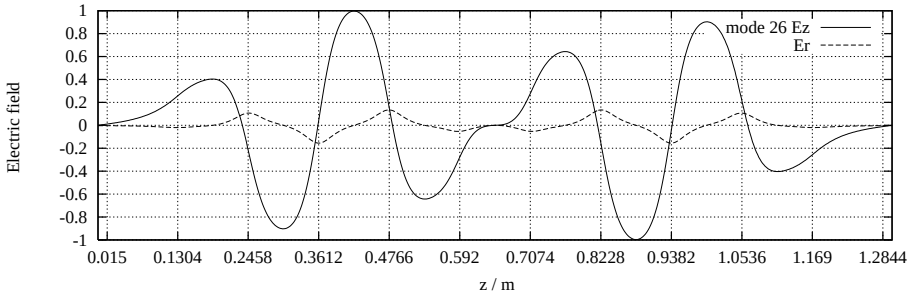

Figure 79: Electric field (E_z at $r = 0$, E_r at $r = 1$ cm) versus z of mode: MM-26

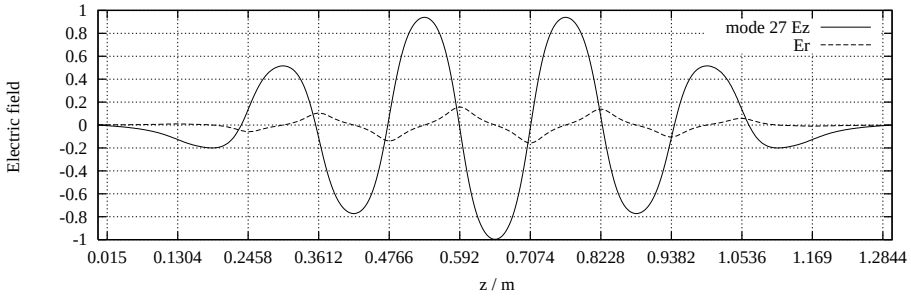

Figure 80: Electric field (E_z at $r = 0$, E_r at $r = 1$ cm) versus z of mode: MM-27

A.1.4 Beam pipe modes and modes from band 4

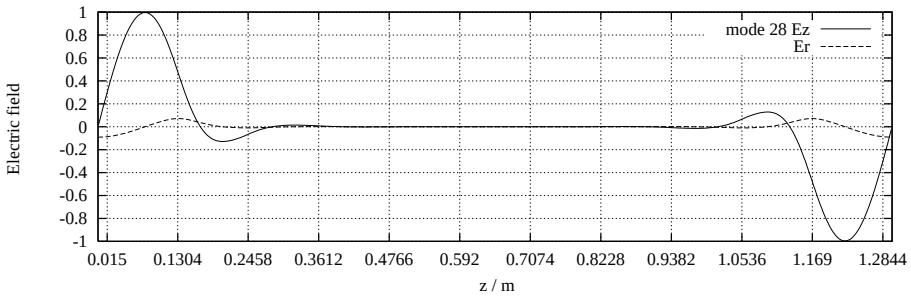

Figure 81: Electric field (E_z at $r = 0$, E_r at $r = 1$ cm) versus z of mode: MM-28

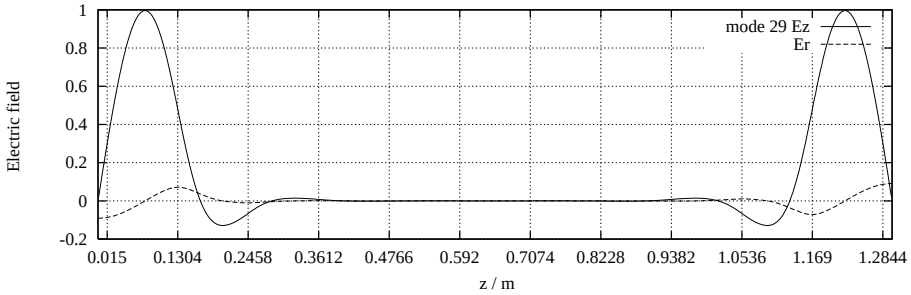

Figure 82: Electric field (E_z at $r = 0$, E_r at $r = 1$ cm) versus z of mode: MM-29

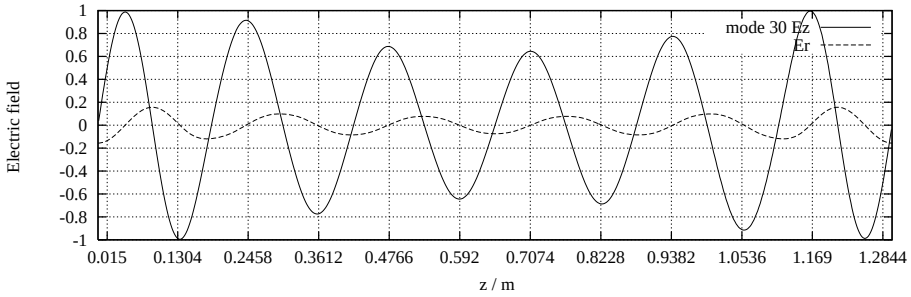

Figure 83: Electric field (E_z at $r = 0$, E_r at $r = 1$ cm) versus z of mode: MM-30

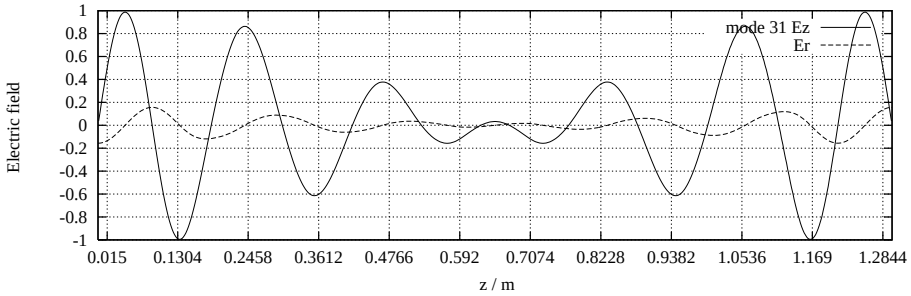

Figure 84: Electric field (E_z at $r = 0$, E_r at $r = 1$ cm) versus z of mode: MM-31

B Electric Fields of Dipole modes

B.1 TDR-like TESLA 9-cell cavity, magnetic (MM) boundary conditions.

B.1.1 Band 1

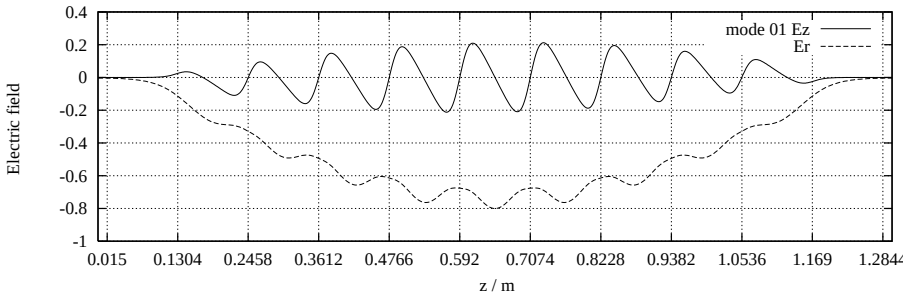

Figure 85: Electric field ($3 \cdot E_z$ and E_r) at $r = 1$ cm versus z of mode: MM-01

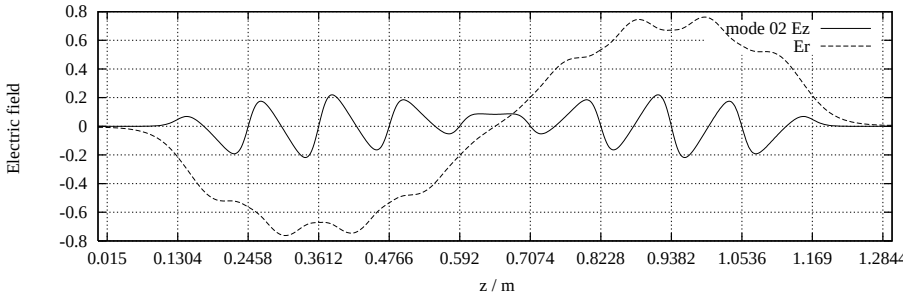

Figure 86: Electric field ($3 \cdot E_z$ and E_r) at $r = 1$ cm versus z of mode: MM-02

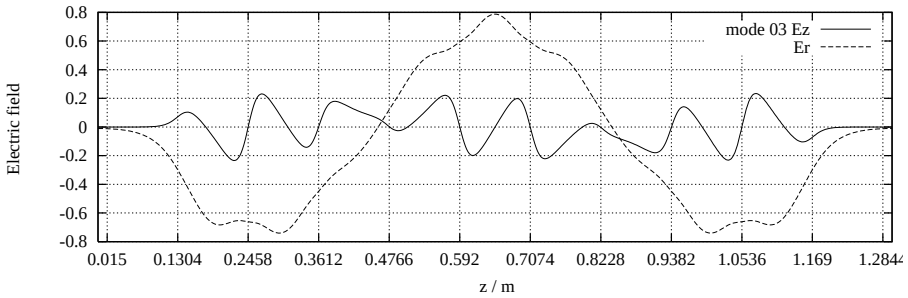

Figure 87: Electric field ($3 \cdot E_z$ and E_r) at $r = 1$ cm versus z of mode: MM-03

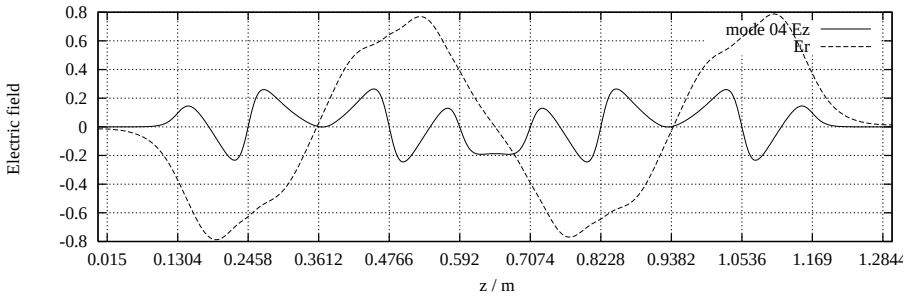

Figure 88: Electric field ($3 \cdot E_z$ and E_r) at $r = 1$ cm versus z of mode: MM-04

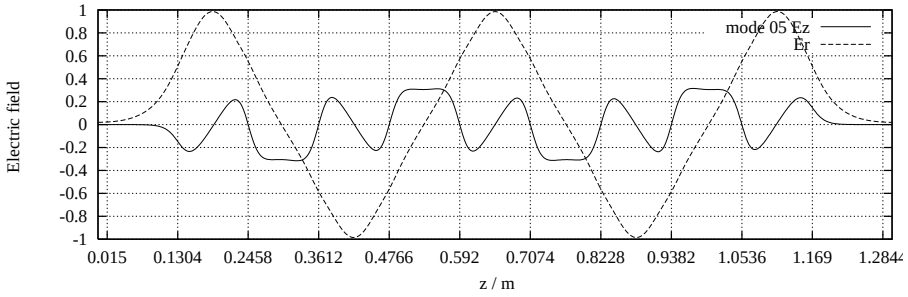

Figure 89: Electric field ($3 \cdot E_z$ and E_r) at $r = 1$ cm versus z of mode: MM-05

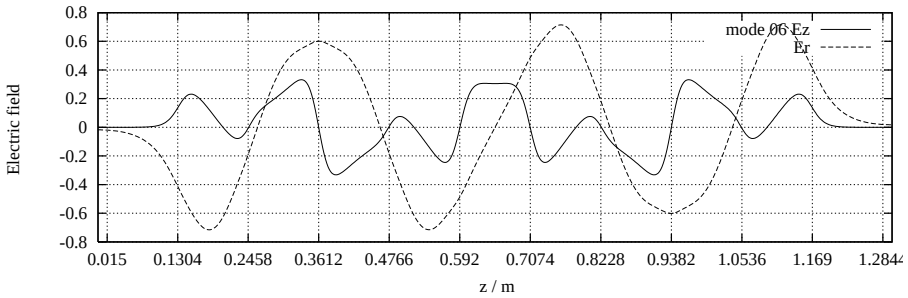

Figure 90: Electric field ($3 \cdot E_z$ and E_r) at $r = 1$ cm versus z of mode: MM-06

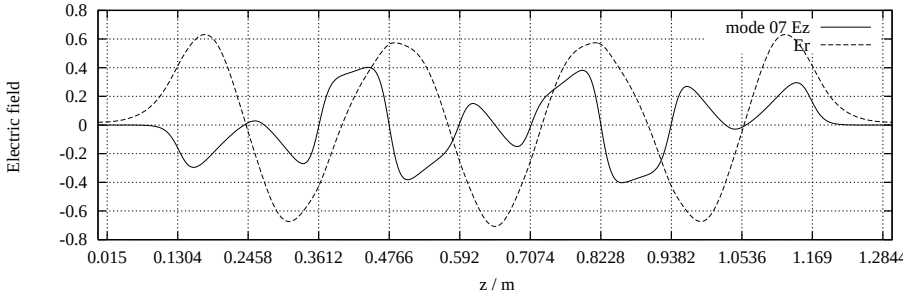

Figure 91: Electric field ($3 \cdot E_z$ and E_r) at $r = 1$ cm versus z of mode: MM-07

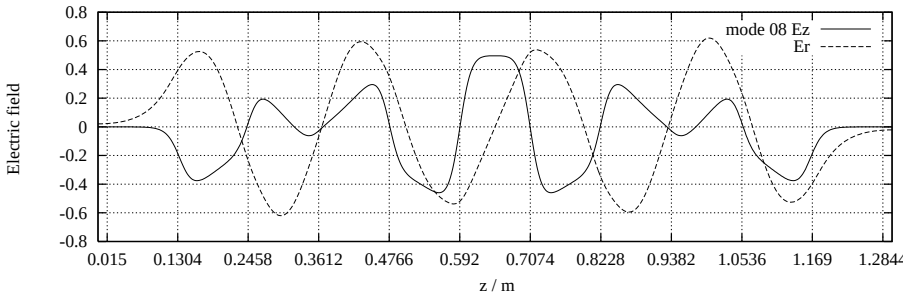

Figure 92: Electric field ($3 \cdot E_z$ and E_r) at $r = 1$ cm versus z of mode: MM-08

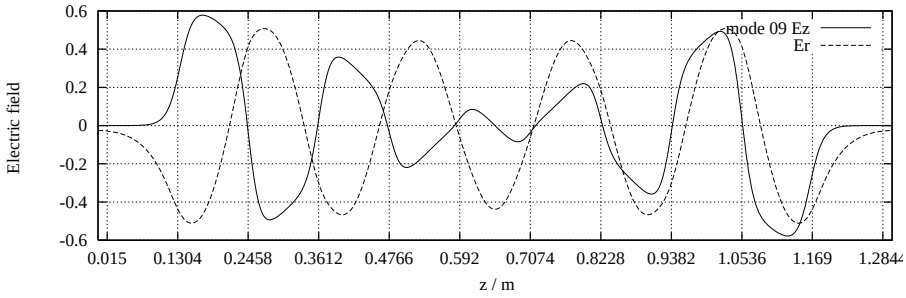

Figure 93: Electric field ($3 \cdot E_z$ and E_r) at $r = 1$ cm versus z of mode: MM-09

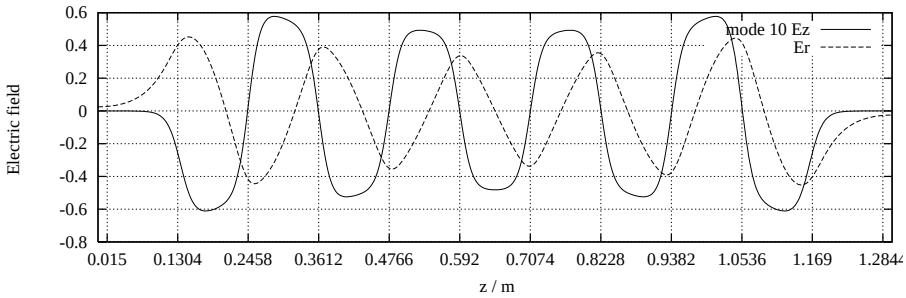

Figure 94: Electric field ($3 \cdot E_z$ and E_r) at $r = 1$ cm versus z of mode: MM-10

B.1.2 Band 2

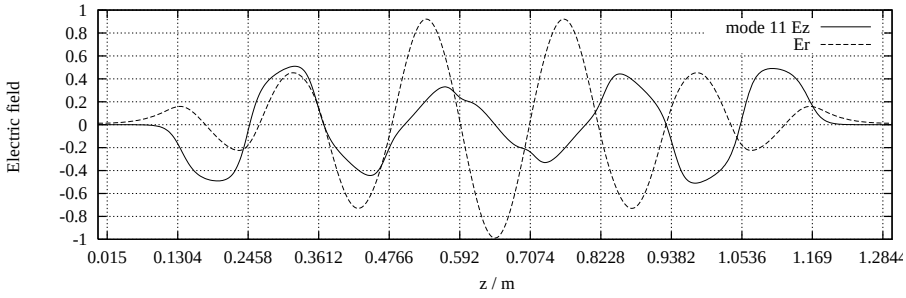

Figure 95: Electric field ($3 \cdot E_z$ and E_r) at $r = 1$ cm versus z of mode: MM-11

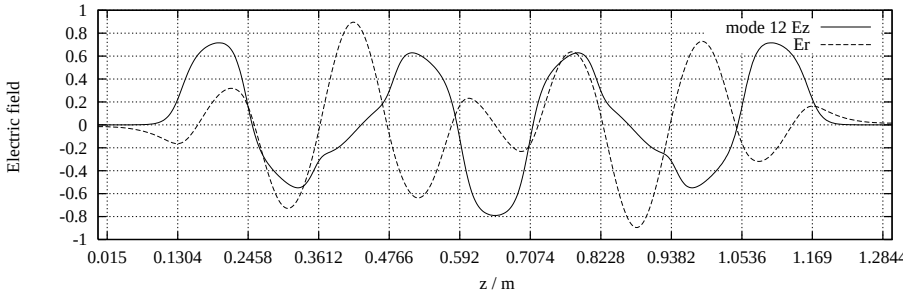

Figure 96: Electric field ($3 \cdot E_z$ and E_r) at $r = 1$ cm versus z of mode: MM-12

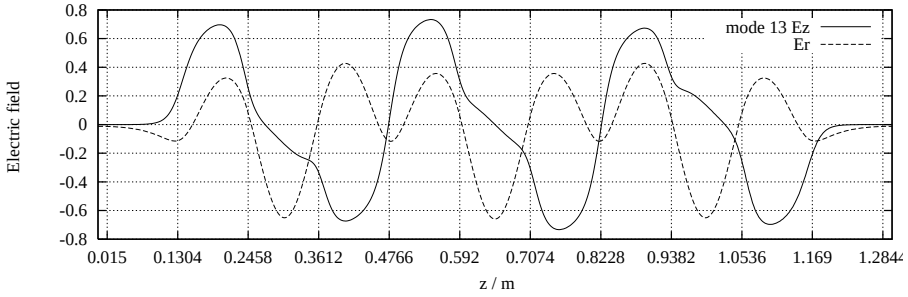

Figure 97: Electric field ($3 \cdot E_z$ and E_r) at $r = 1$ cm versus z of mode: MM-13

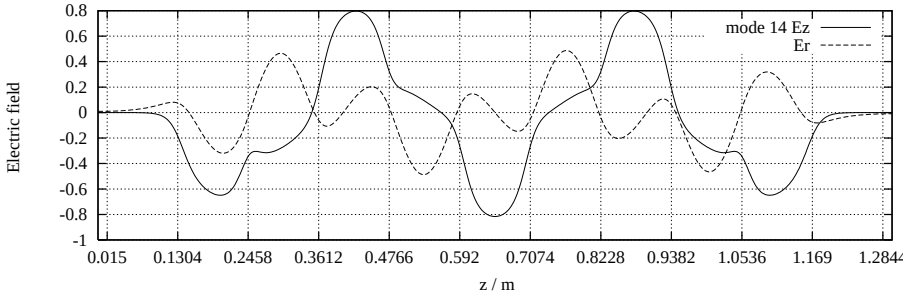

Figure 98: Electric field ($3 \cdot E_z$ and E_r) at $r = 1$ cm versus z of mode: MM-14

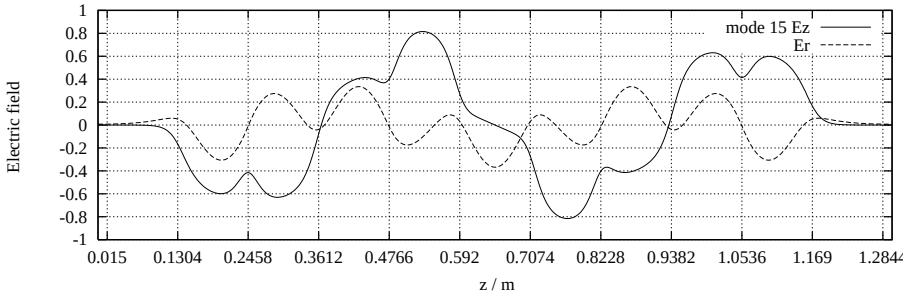

Figure 99: Electric field ($3 \cdot E_z$ and E_r) at $r = 1$ cm versus z of mode: MM-15

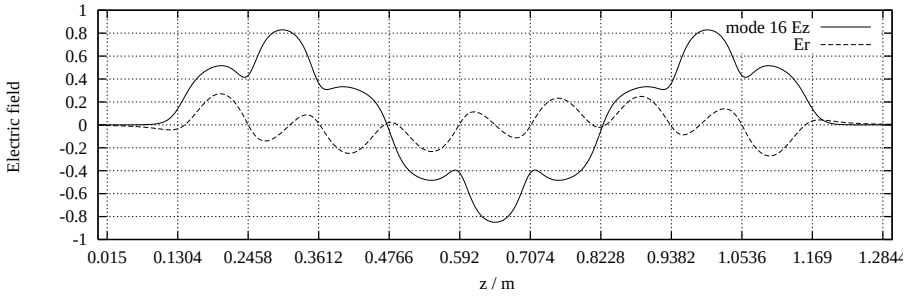

Figure 100: Electric field ($3 \cdot E_z$ and E_r) at $r = 1$ cm versus z of mode: MM-16

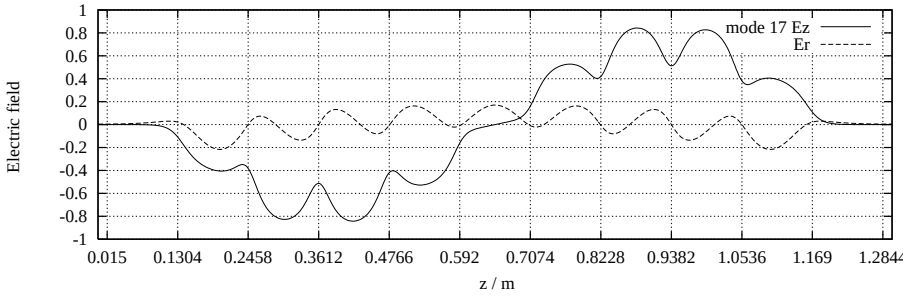

Figure 101: Electric field ($3 \cdot E_z$ and E_r) at $r = 1$ cm versus z of mode: MM-17

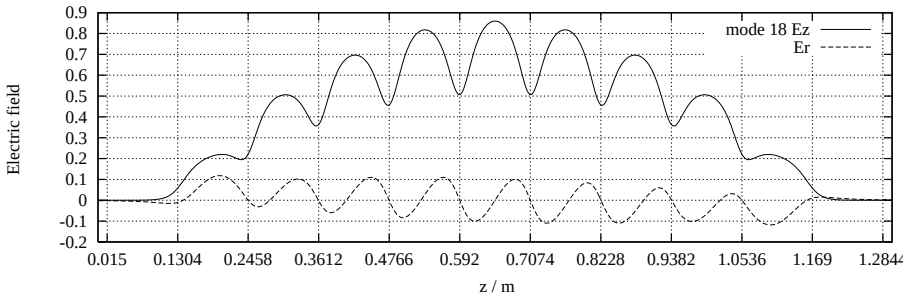

Figure 102: Electric field ($3 \cdot E_z$ and E_r) at $r = 1$ cm versus z of mode: MM-18

B.1.3 Beam pipe modes

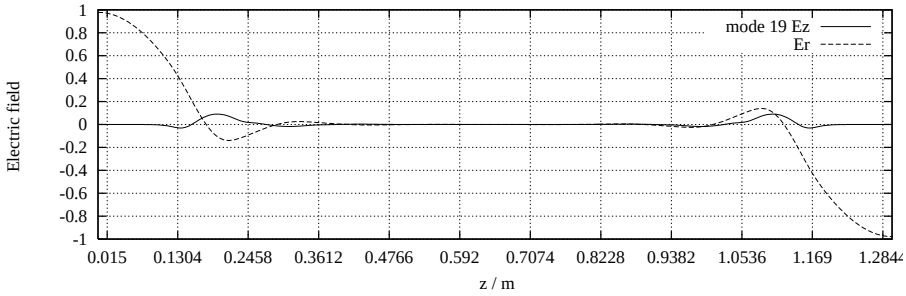

Figure 103: Electric field ($3 \cdot E_z$ and E_r) at $r = 1$ cm versus z of mode: MM-19

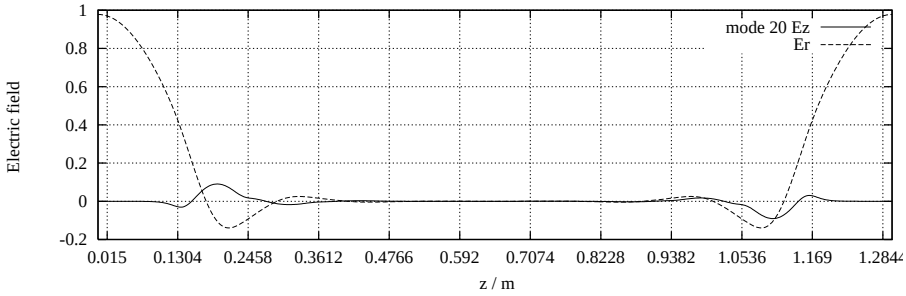

Figure 104: Electric field ($3 \cdot E_z$ and E_r) at $r = 1$ cm versus z of mode: MM-20

B.1.4 Band 3

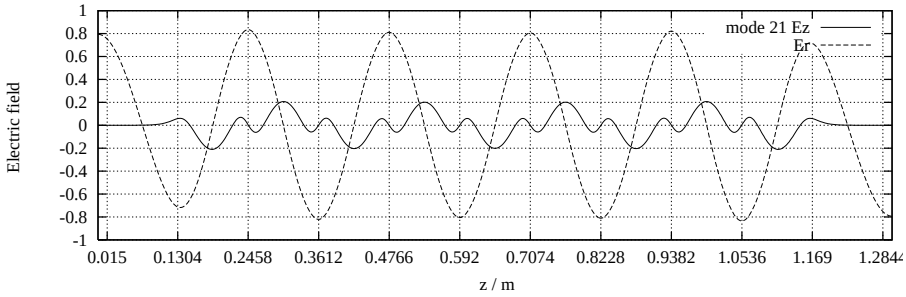

Figure 105: Electric field ($3 \cdot E_z$ and E_r) at $r = 1$ cm versus z of mode: MM-21

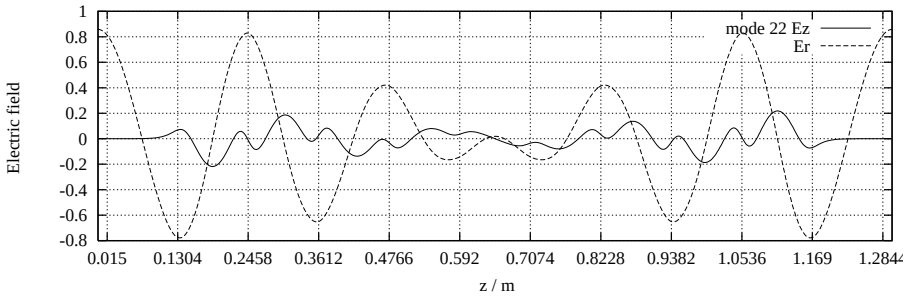

Figure 106: Electric field ($3 \cdot E_z$ and E_r) at $r = 1$ cm versus z of mode: MM-22

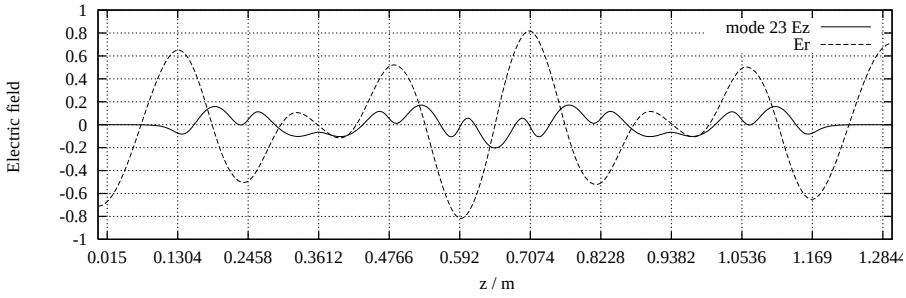

Figure 107: Electric field ($3 \cdot E_z$ and E_r) at $r = 1$ cm versus z of mode: MM-23

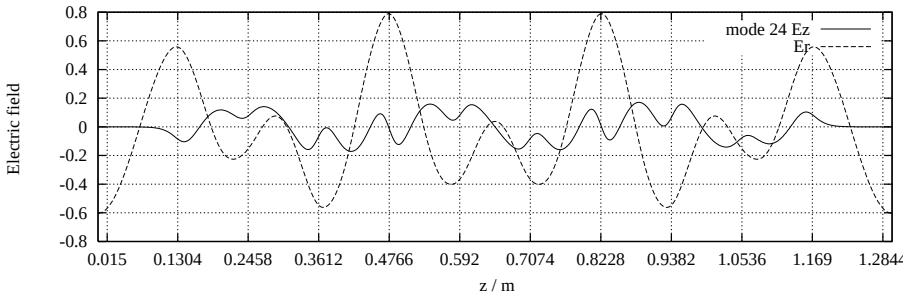

Figure 108: Electric field ($3 \cdot E_z$ and E_r) at $r = 1$ cm versus z of mode: MM-24

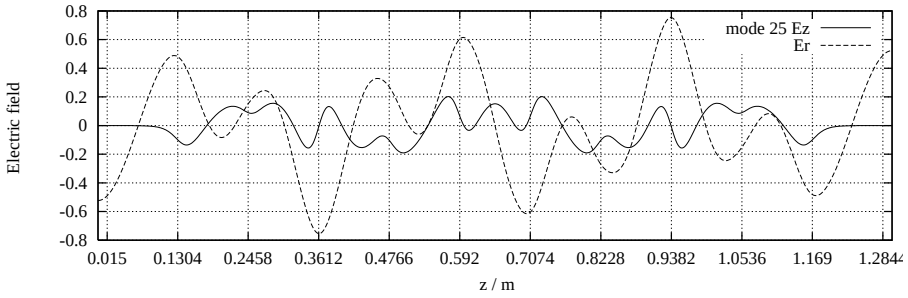

Figure 109: Electric field ($3 \cdot E_z$ and E_r) at $r = 1$ cm versus z of mode: MM-25

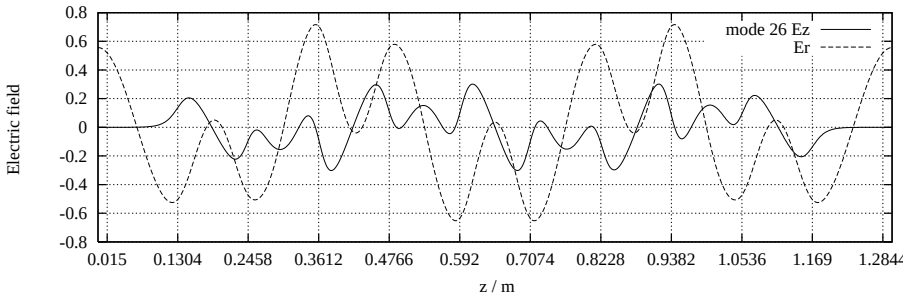

Figure 110: Electric field ($3 \cdot E_z$ and E_r) at $r = 1$ cm versus z of mode: MM-26

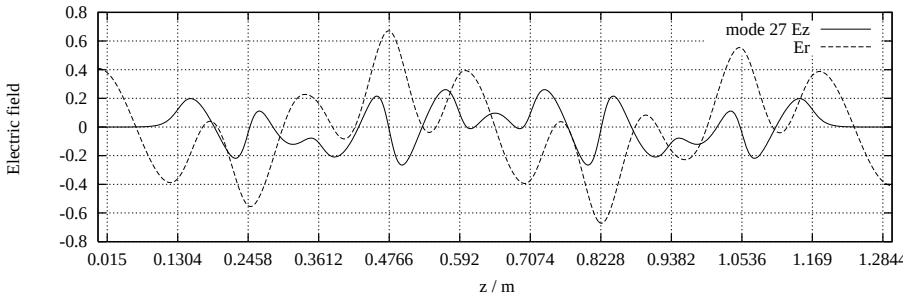

Figure 111: Electric field ($3 \cdot E_z$ and E_r) at $r = 1$ cm versus z of mode: MM-27

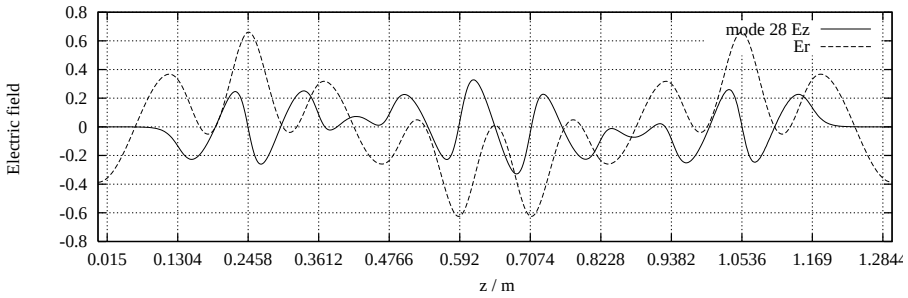

Figure 112: Electric field ($3 \cdot E_z$ and E_r) at $r = 1$ cm versus z of mode: MM-28

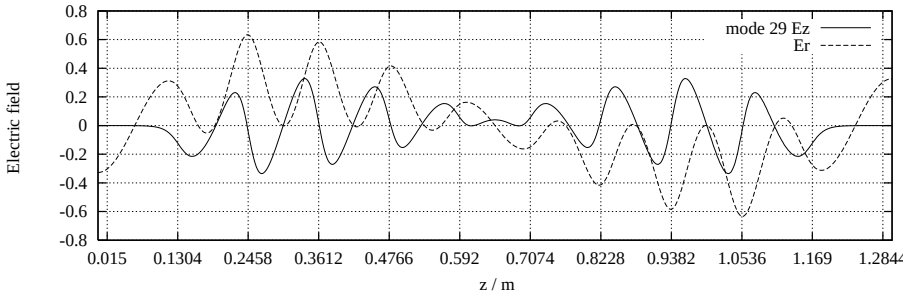

Figure 113: Electric field ($3 \cdot E_z$ and E_r) at $r = 1$ cm versus z of mode: MM-29

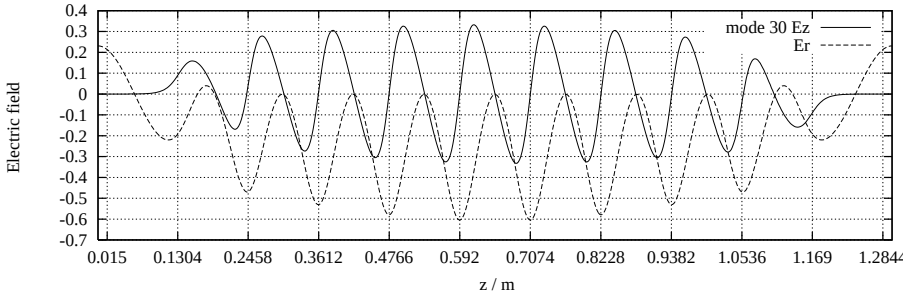

Figure 114: Electric field ($3 \cdot E_z$ and E_r) at $r = 1$ cm versus z of mode: MM-30

B.1.5 Band 4

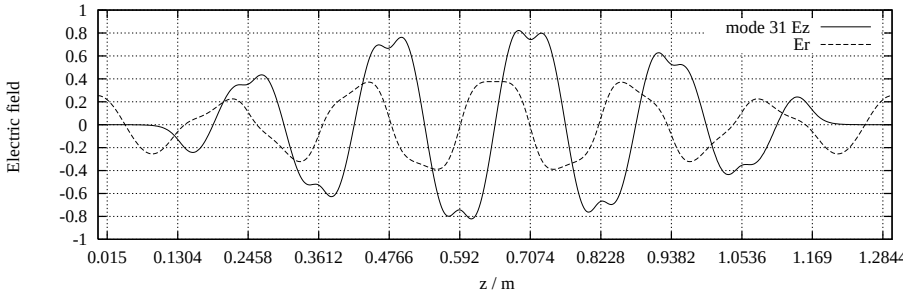

Figure 115: Electric field ($3 \cdot E_z$ and E_r) at $r = 1$ cm versus z of mode: MM-31

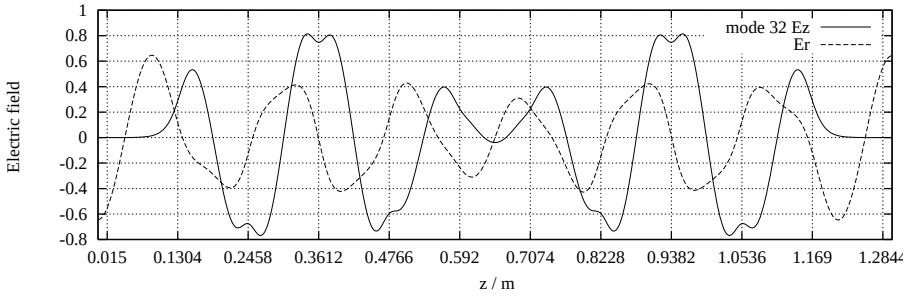

Figure 116: Electric field ($3 \cdot E_z$ and E_r) at $r = 1$ cm versus z of mode: MM-32

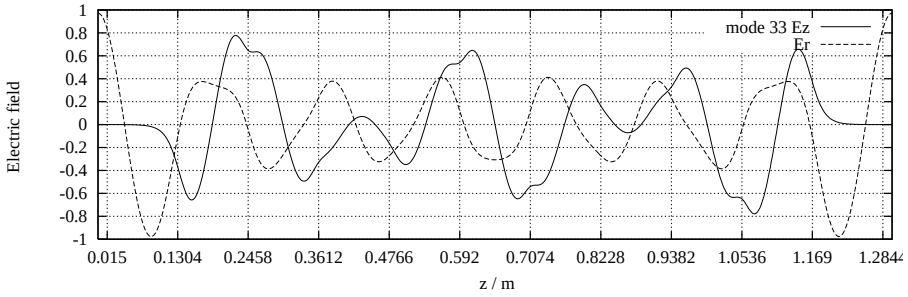

Figure 117: Electric field ($3 \cdot E_z$ and E_r) at $r = 1$ cm versus z of mode: MM-33

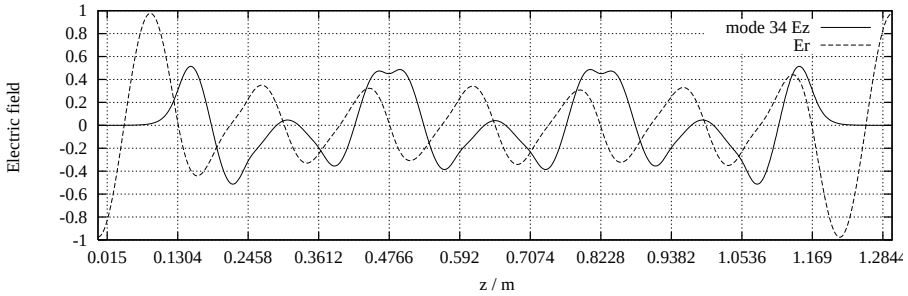

Figure 118: Electric field ($3 \cdot E_z$ and E_r) at $r = 1$ cm versus z of mode: MM-34

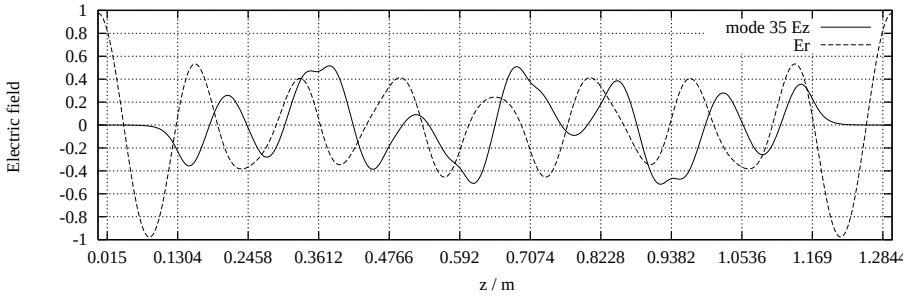

Figure 119: Electric field ($3 \cdot E_z$ and E_r) at $r = 1$ cm versus z of mode: MM-35

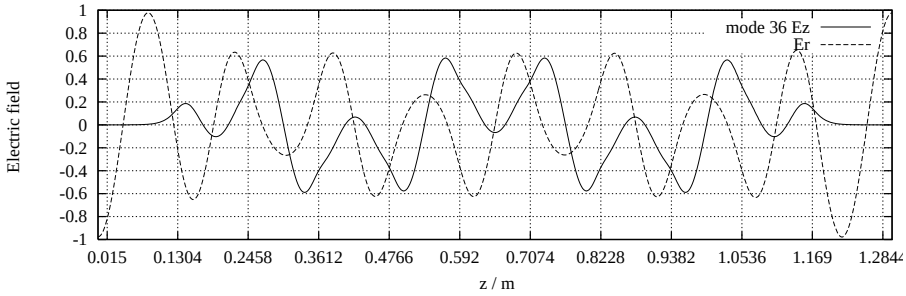

Figure 120: Electric field ($3 \cdot E_z$ and E_r) at $r = 1$ cm versus z of mode: MM-36

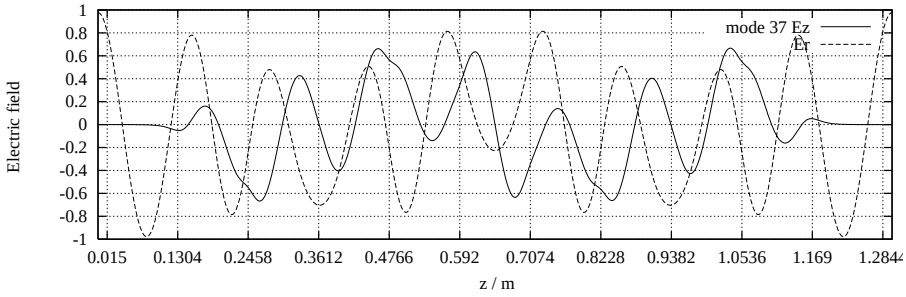

Figure 121: Electric field ($3 \cdot E_z$ and E_r) at $r = 1$ cm versus z of mode: MM-37

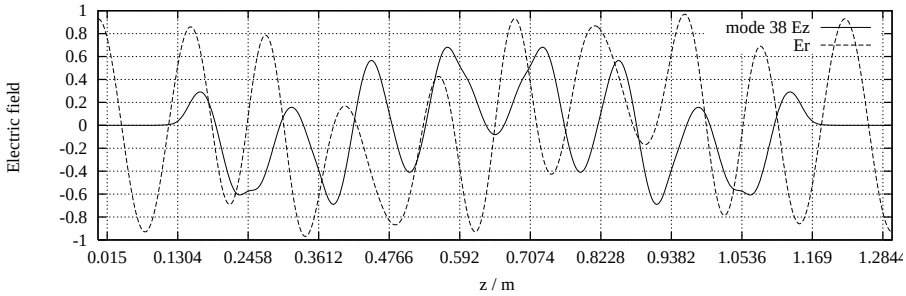

Figure 122: Electric field ($3 \cdot E_z$ and E_r) at $r = 1$ cm versus z of mode: MM-38

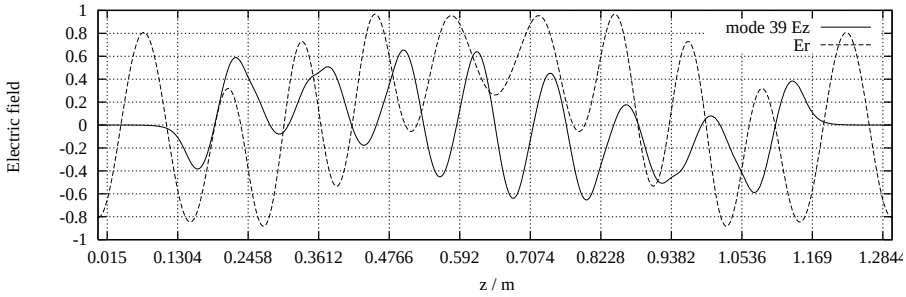

Figure 123: Electric field ($3 \cdot E_z$ and E_r) at $r = 1$ cm versus z of mode: MM-39

B.1.6 Beam pipe modes

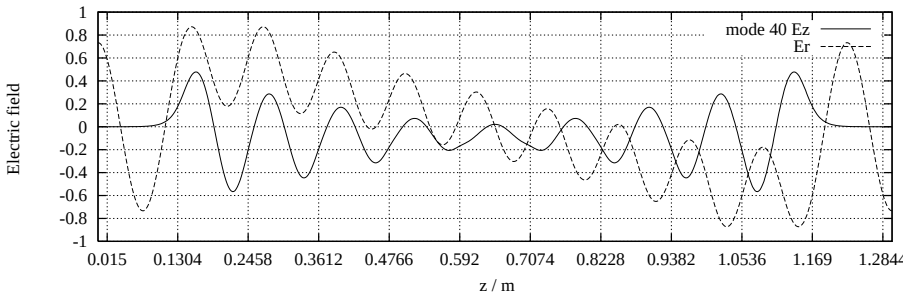

Figure 124: Electric field ($3 \cdot E_z$ and E_r) at $r = 1$ cm versus z of mode: MM-40

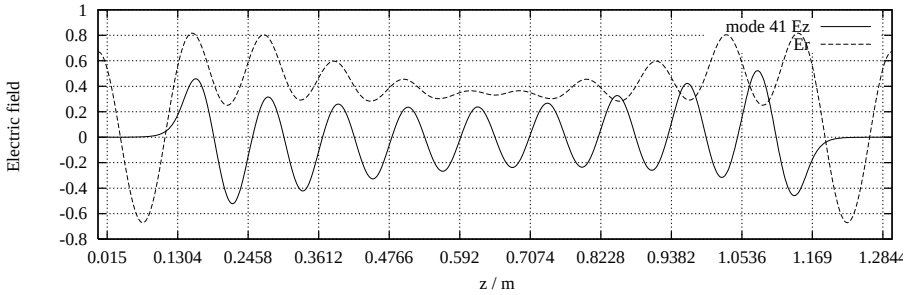

Figure 125: Electric field ($3 \cdot E_z$ and E_r) at $r = 1$ cm versus z of mode: MM-41

B.1.7 Band 5

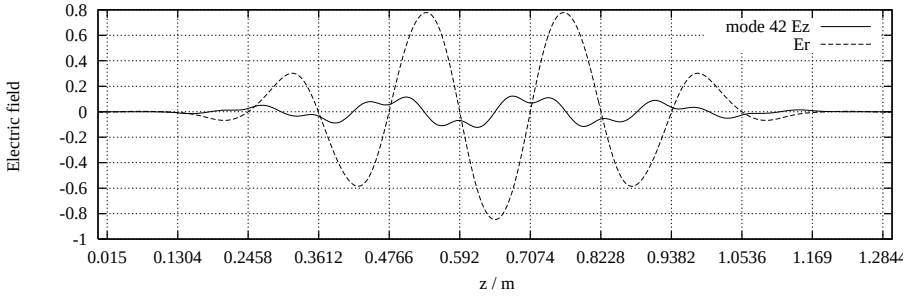

Figure 126: Electric field ($3 \cdot E_z$ and E_r) at $r = 1$ cm versus z of mode: MM-42

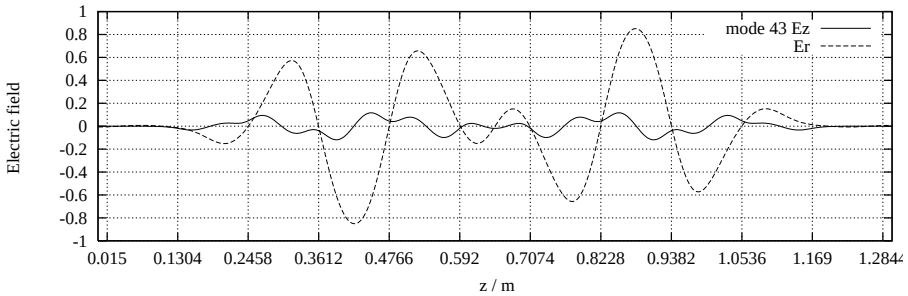

Figure 127: Electric field ($3 \cdot E_z$ and E_r) at $r = 1$ cm versus z of mode: MM-43

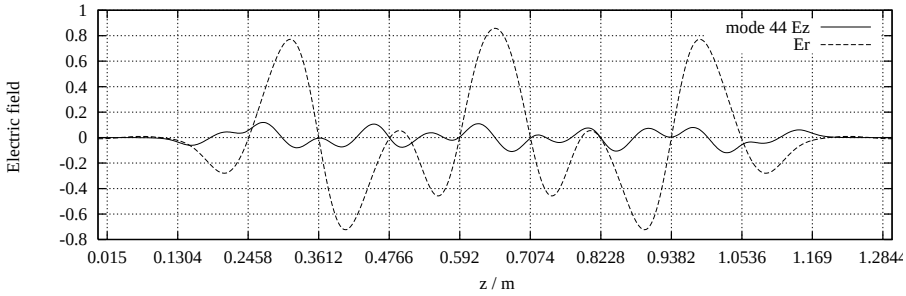

Figure 128: Electric field ($3 \cdot E_z$ and E_r) at $r = 1$ cm versus z of mode: MM-44

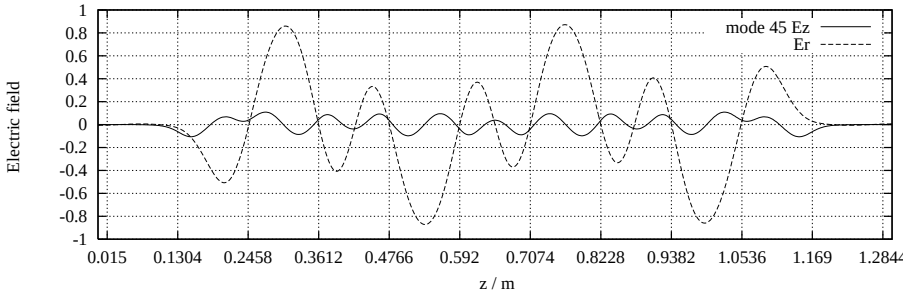

Figure 129: Electric field ($3 \cdot E_z$ and E_r) at $r = 1$ cm versus z of mode: MM-45

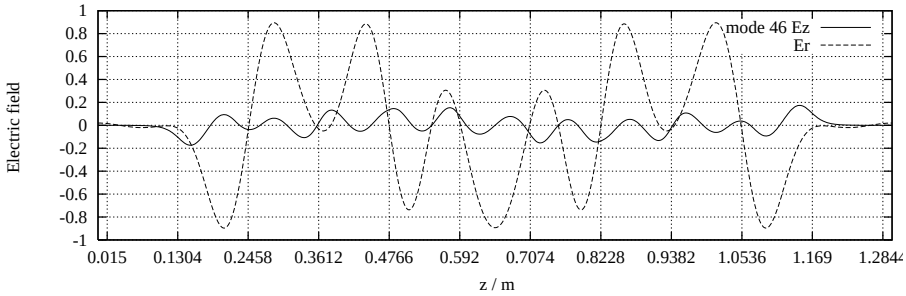

Figure 130: Electric field ($3 \cdot E_z$ and E_r) at $r = 1$ cm versus z of mode: MM-46

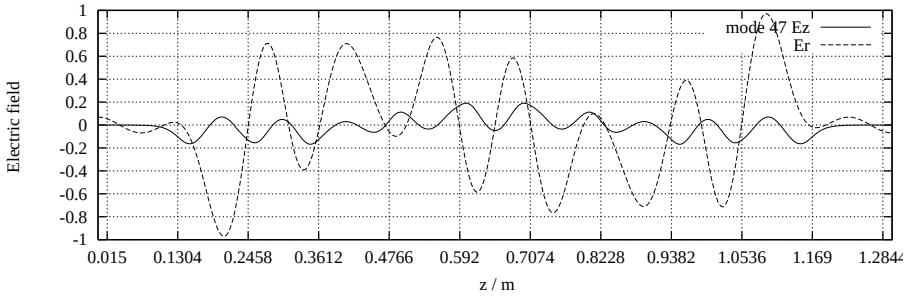

Figure 131: Electric field ($3 \cdot E_z$ and E_r) at $r = 1$ cm versus z of mode: MM-47

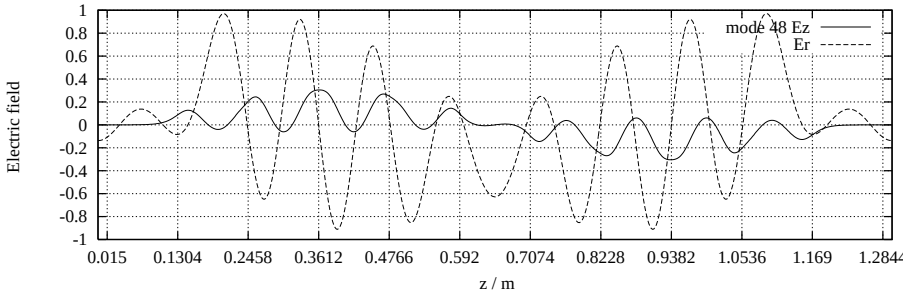

Figure 132: Electric field ($3 \cdot E_z$ and E_r) at $r = 1$ cm versus z of mode: MM-48

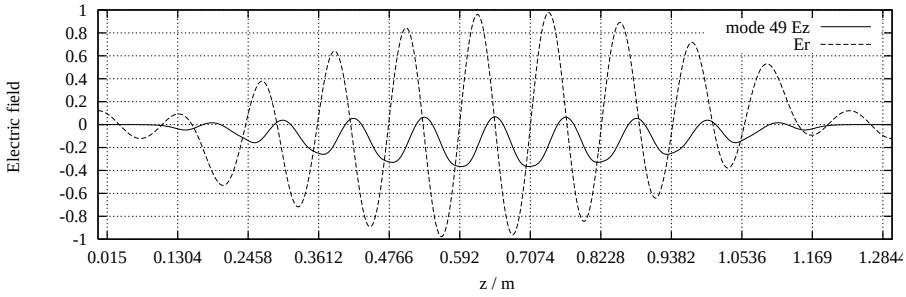

Figure 133: Electric field ($3 \cdot E_z$ and E_r) at $r = 1$ cm versus z of mode: MM-49

B.1.8 Band 6

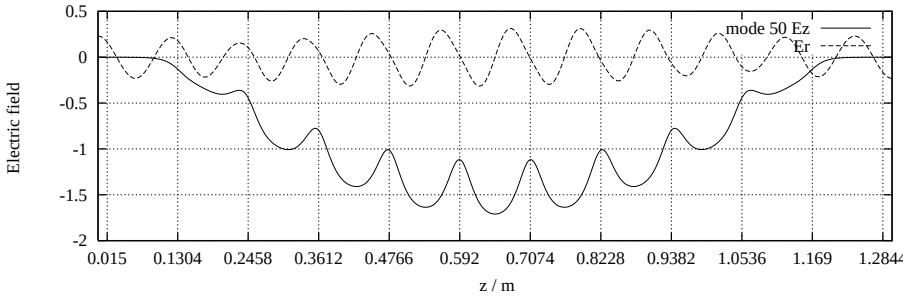

Figure 134: Electric field ($3 \cdot E_z$ and E_r) at $r = 1$ cm versus z of mode: MM-50

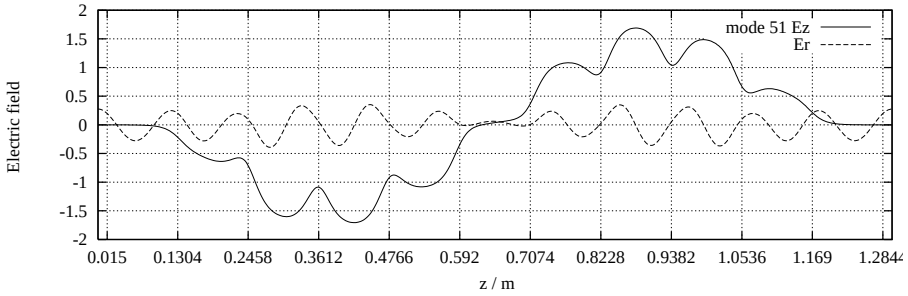

Figure 135: Electric field ($3 \cdot E_z$ and E_r) at $r = 1$ cm versus z of mode: MM-51

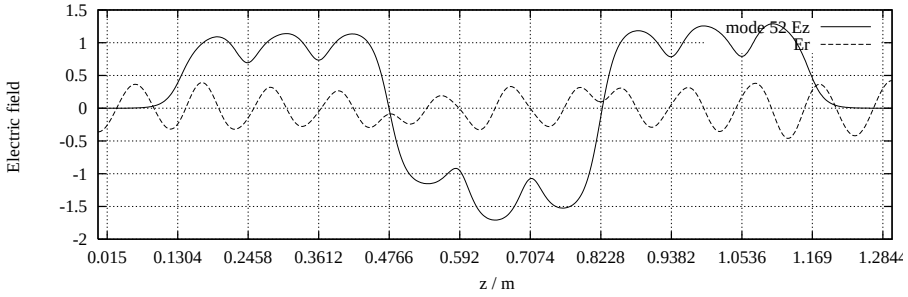

Figure 136: Electric field ($3 \cdot E_z$ and E_r) at $r = 1$ cm versus z of mode: MM-52

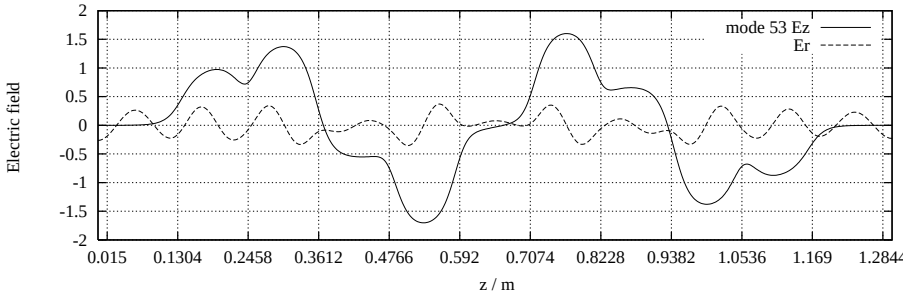

Figure 137: Electric field ($3 \cdot E_z$ and E_r) at $r = 1$ cm versus z of mode: MM-53

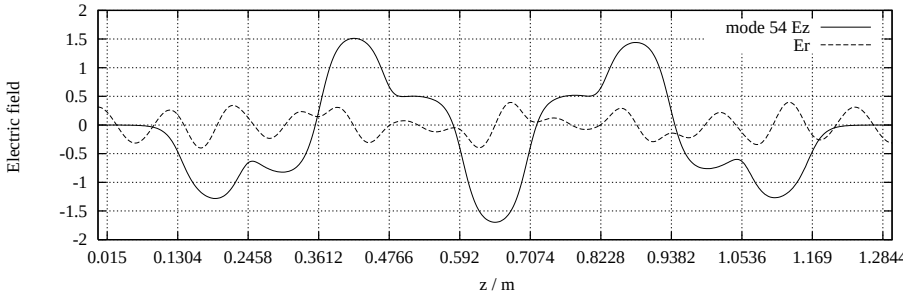

Figure 138: Electric field ($3 \cdot E_z$ and E_r) at $r = 1$ cm versus z of mode: MM-54

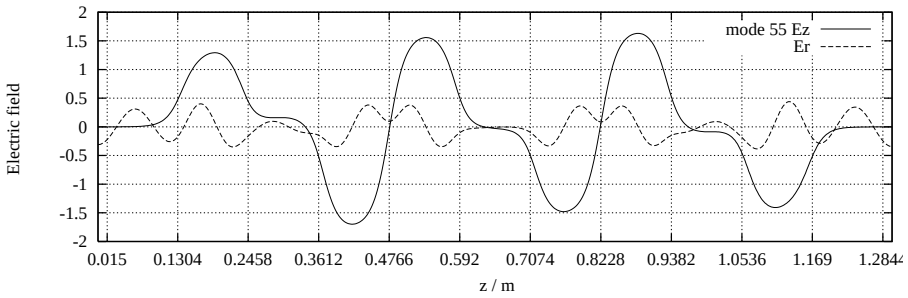

Figure 139: Electric field ($3 \cdot E_z$ and E_r) at $r = 1$ cm versus z of mode: MM-55

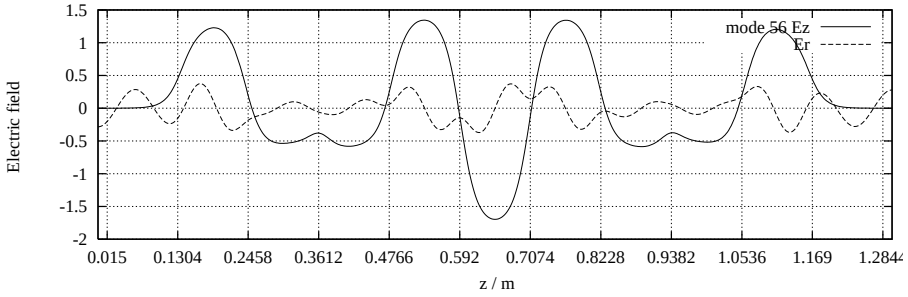

Figure 140: Electric field ($3 \cdot E_z$ and E_r) at $r = 1$ cm versus z of mode: MM-56

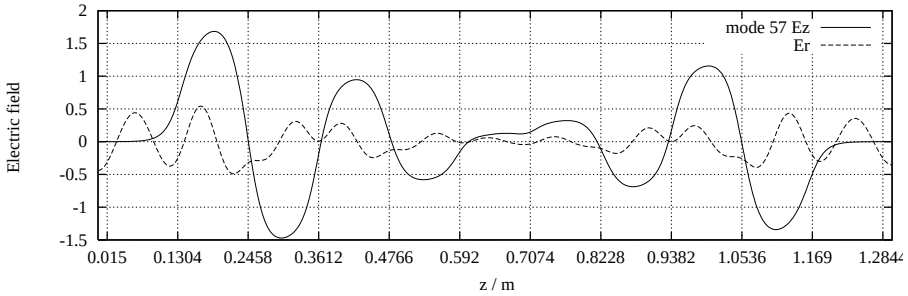

Figure 141: Electric field ($3 \cdot E_z$ and E_r) at $r = 1$ cm versus z of mode: MM-57

B.1.9 Beam pipe modes

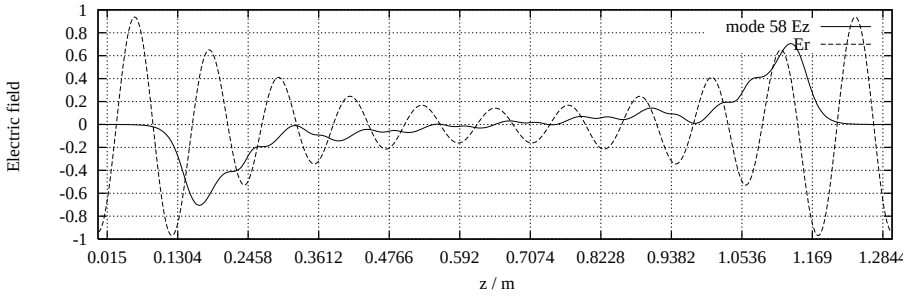

Figure 142: Electric field ($3 \cdot E_z$ and E_r) at $r = 1$ cm versus z of mode: MM-58

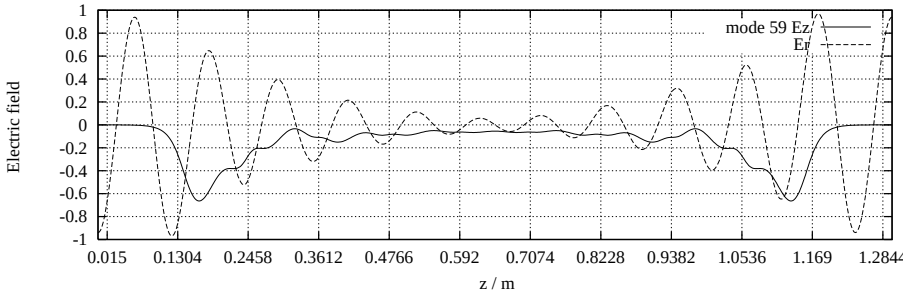

Figure 143: Electric field ($3 \cdot E_z$ and E_r) at $r = 1$ cm versus z of mode: MM-59

B.1.10 Band 7 and modes above band 7

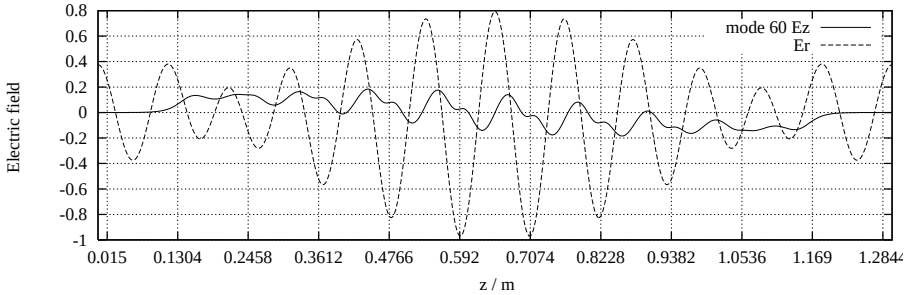

Figure 144: Electric field ($3 \cdot E_z$ and E_r) at $r = 1$ cm versus z of mode: MM-60

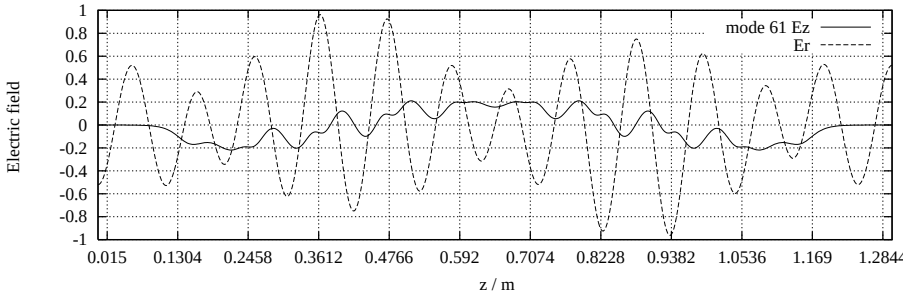

Figure 145: Electric field ($3 \cdot E_z$ and E_r) at $r = 1$ cm versus z of mode: MM-61

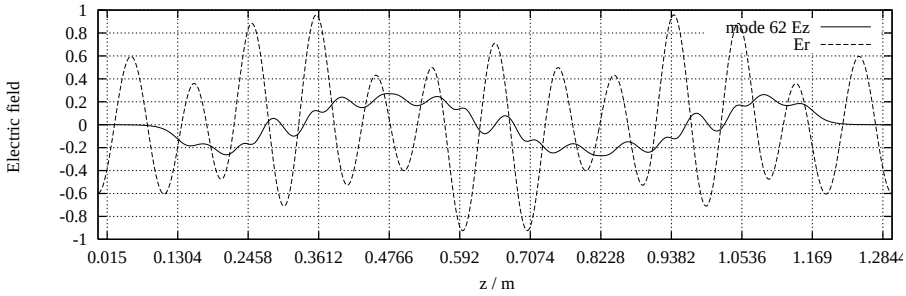

Figure 146: Electric field ($3 \cdot E_z$ and E_r) at $r = 1$ cm versus z of mode: MM-62

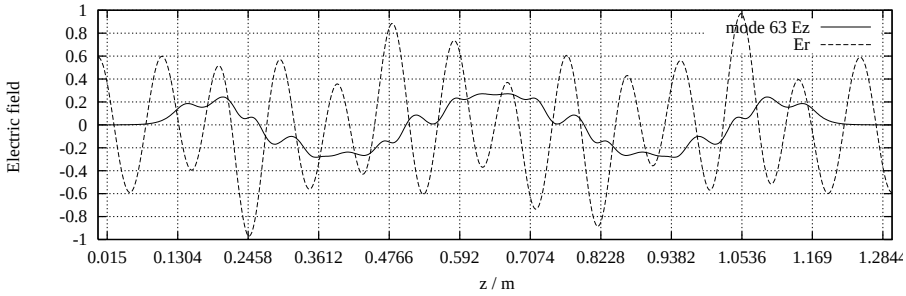

Figure 147: Electric field ($3 \cdot E_z$ and E_r) at $r = 1$ cm versus z of mode: MM-63

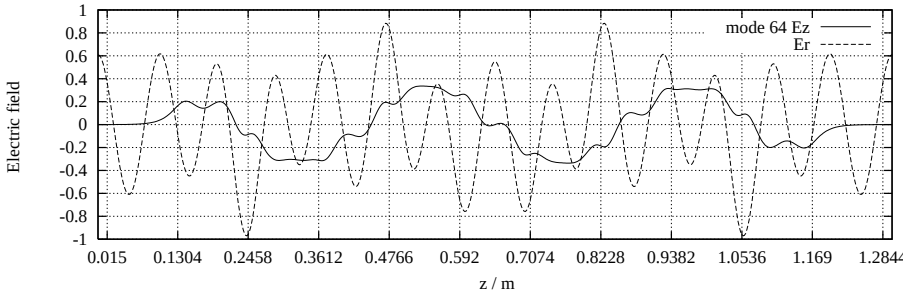

Figure 148: Electric field ($3 \cdot E_z$ and E_r) at $r = 1$ cm versus z of mode: MM-64

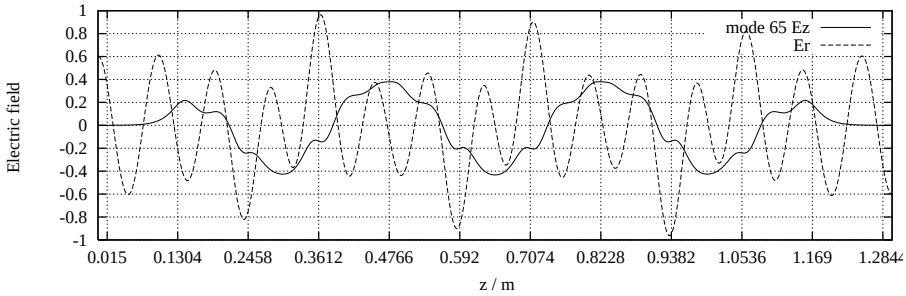

Figure 149: Electric field ($3 \cdot E_z$ and E_r) at $r = 1$ cm versus z of mode: MM-65

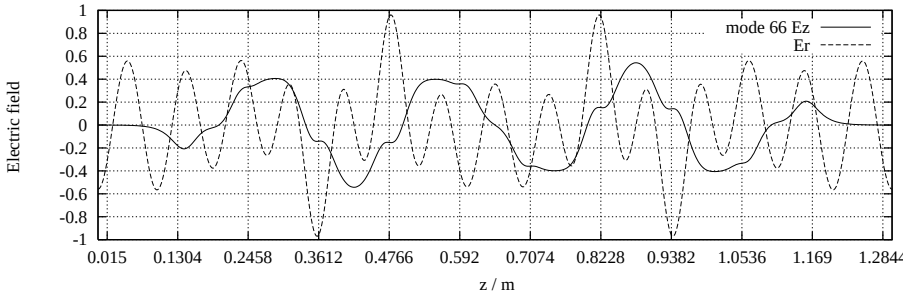

Figure 150: Electric field ($3 \cdot E_z$ and E_r) at $r = 1$ cm versus z of mode: MM-66

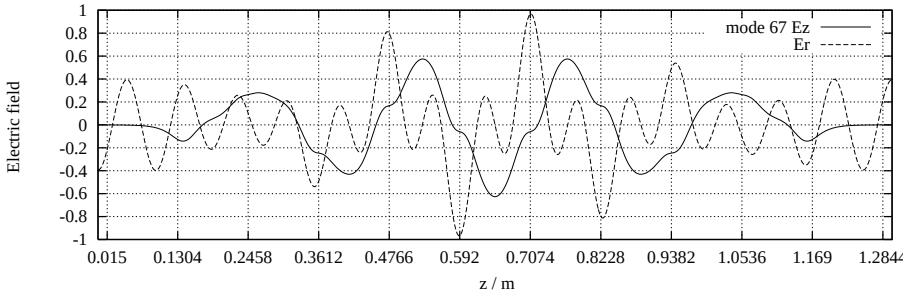

Figure 151: Electric field ($3 \cdot E_z$ and E_r) at $r = 1$ cm versus z of mode: MM-67

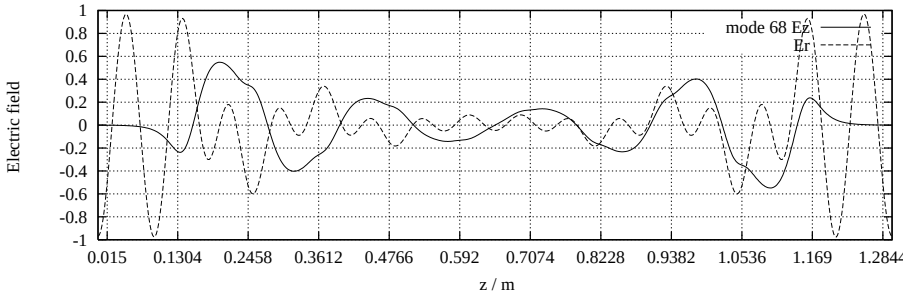

Figure 152: Electric field ($3 \cdot E_z$ and E_r) at $r = 1$ cm versus z of mode: MM-68

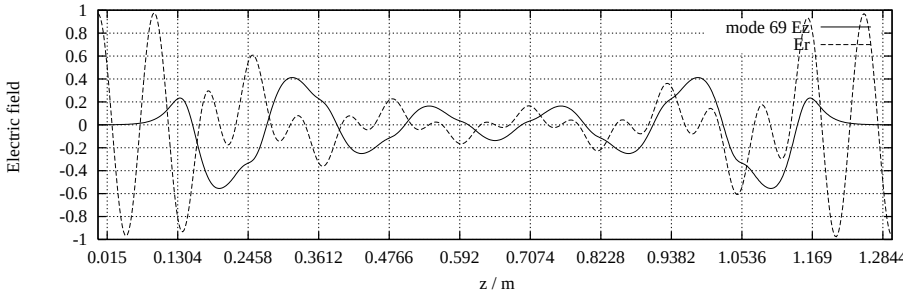

Figure 153: Electric field ($3 \cdot E_z$ and E_r) at $r = 1$ cm versus z of mode: MM-69

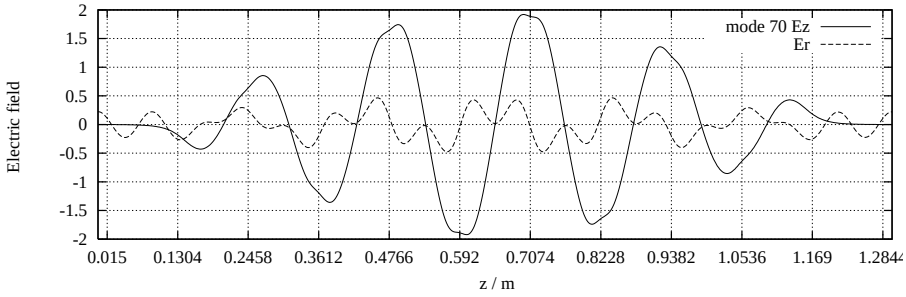

Figure 154: Electric field ($3 \cdot E_z$ and E_r) at $r = 1$ cm versus z of mode: MM-70

B.2 TDR-like TESLA 9-cell cavity, electric (EE) boundary conditions.

The modes of the first two bands obtained for electric (EE) boundary conditions at both ends are very similar to the modes obtained with magnetic boundary (MM). That is also true for some higher passbands. Therefore it is possible to omit some graphical representations of modes.

B.2.1 Bands 1 and 2

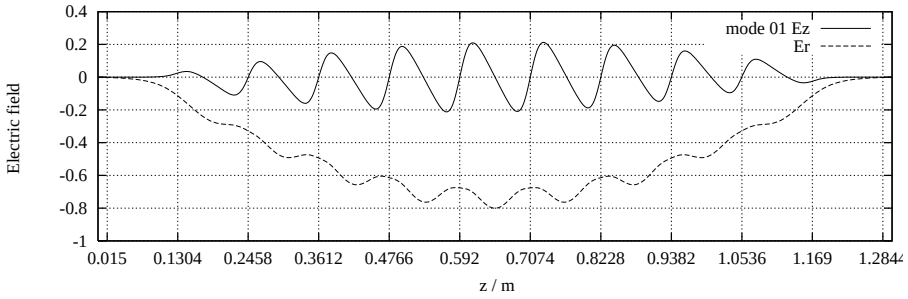

Figure 155: Electric field ($3 \cdot E_z$ and E_r) at $r = 1$ cm versus z of mode: EE-01

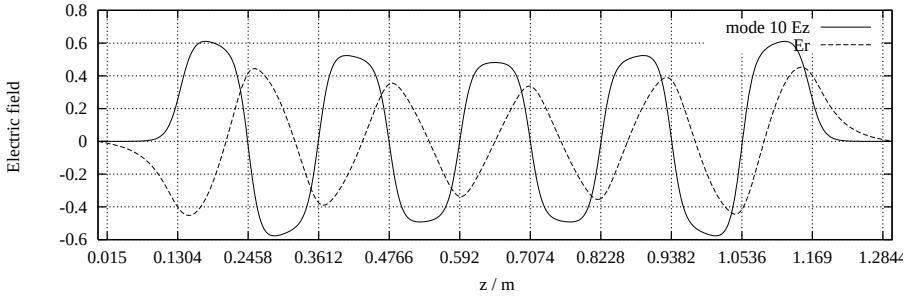

Figure 156: Electric field ($3 \cdot E_z$ and E_r) at $r = 1$ cm versus z of mode: EE-10

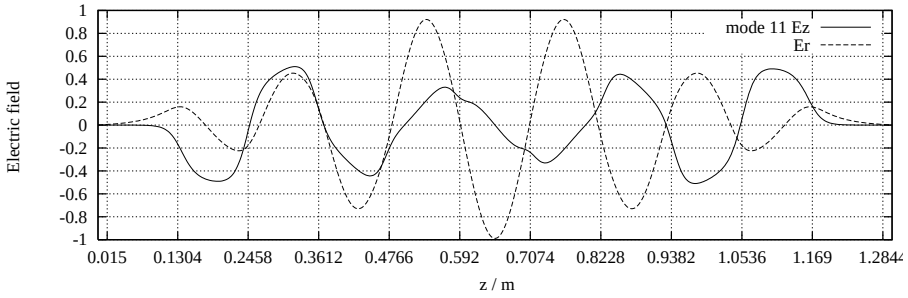

Figure 157: Electric field ($3 \cdot E_z$ and E_r) at $r = 1$ cm versus z of mode: EE-11

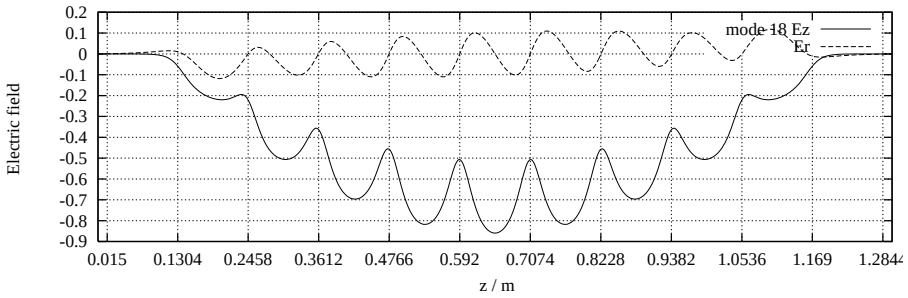

Figure 158: Electric field ($3 \cdot E_z$ and E_r) at $r = 1$ cm versus z of mode: EE-18

B.2.2 Beam pipe modes

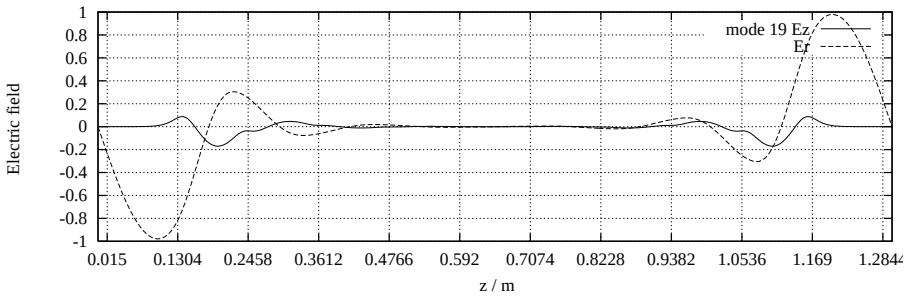

Figure 159: Electric field ($3 \cdot E_z$ and E_r) at $r = 1$ cm versus z of mode: EE-19

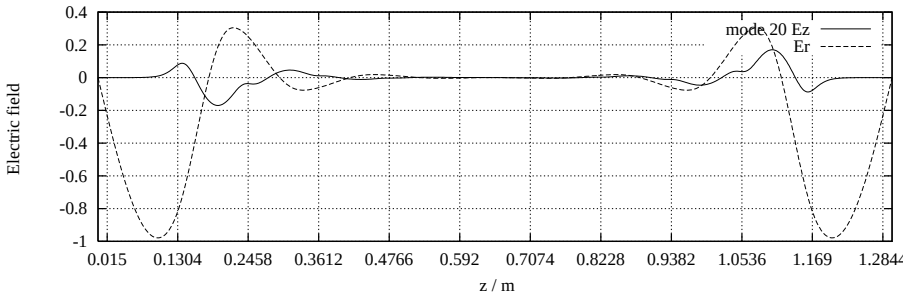

Figure 160: Electric field ($3 \cdot E_z$ and E_r) at $r = 1$ cm versus z of mode: EE-20

B.2.3 Band 3

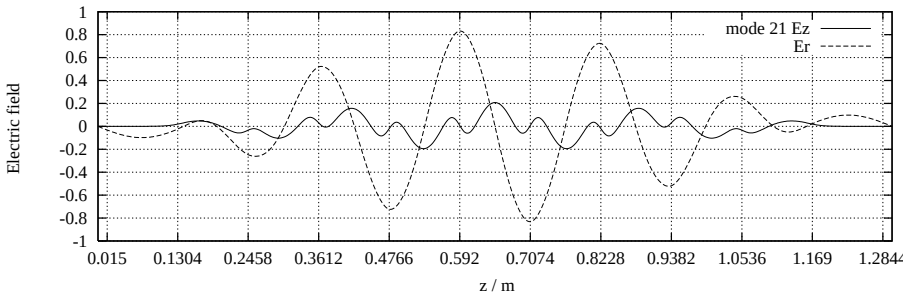

Figure 161: Electric field ($3 \cdot E_z$ and E_r) at $r = 1$ cm versus z of mode: EE-21

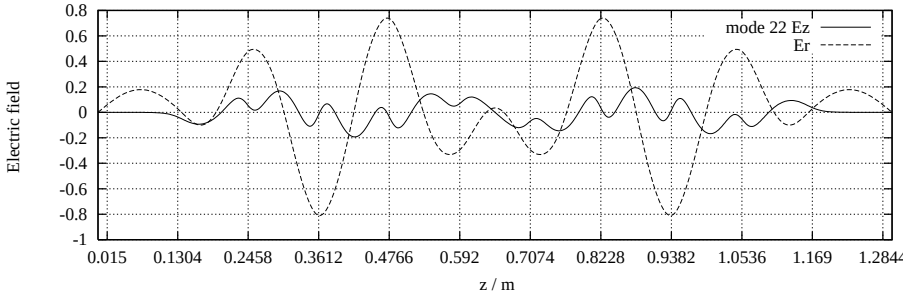

Figure 162: Electric field ($3 \cdot E_z$ and E_r) at $r = 1$ cm versus z of mode: EE-22

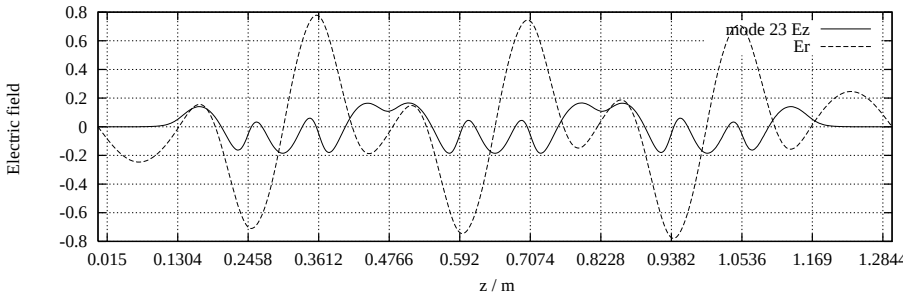

Figure 163: Electric field ($3 \cdot E_z$ and E_r) at $r = 1$ cm versus z of mode: EE-23

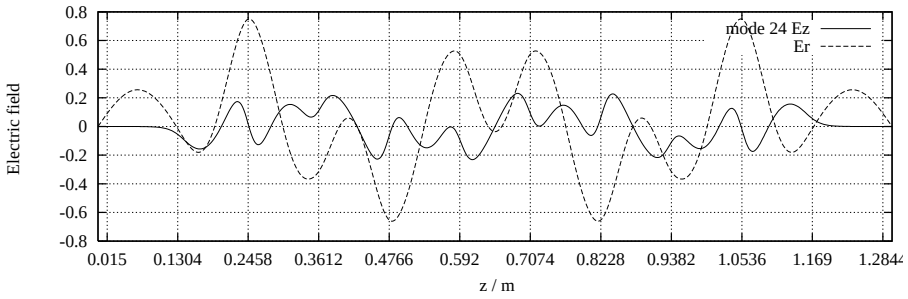

Figure 164: Electric field ($3 \cdot E_z$ and E_r) at $r = 1$ cm versus z of mode: EE-24

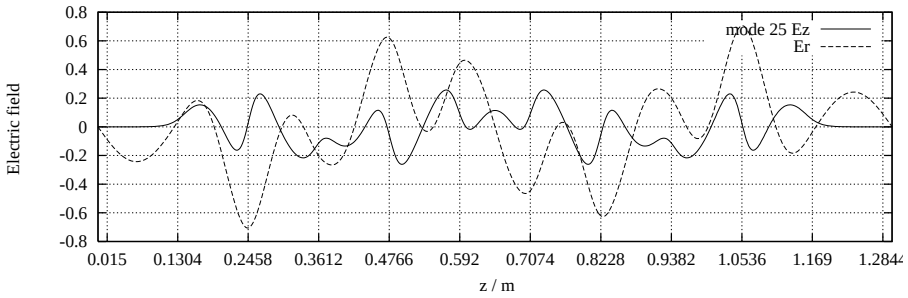

Figure 165: Electric field ($3 \cdot E_z$ and E_r) at $r = 1$ cm versus z of mode: EE-25

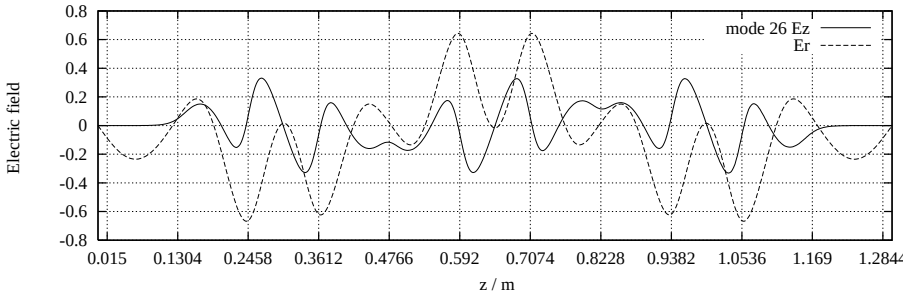

Figure 166: Electric field ($3 \cdot E_z$ and E_r) at $r = 1$ cm versus z of mode: EE-26

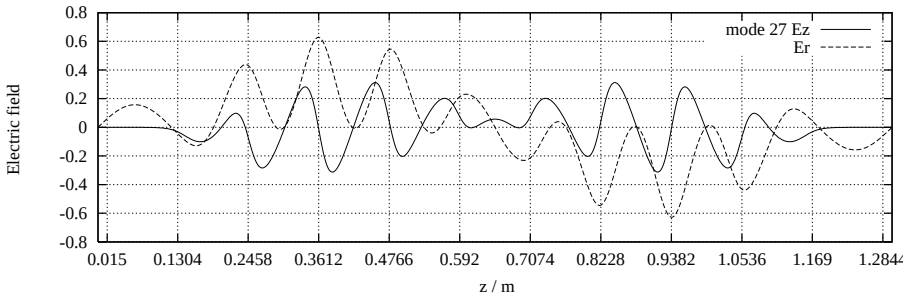

Figure 167: Electric field ($3 \cdot E_z$ and E_r) at $r = 1$ cm versus z of mode: EE-27

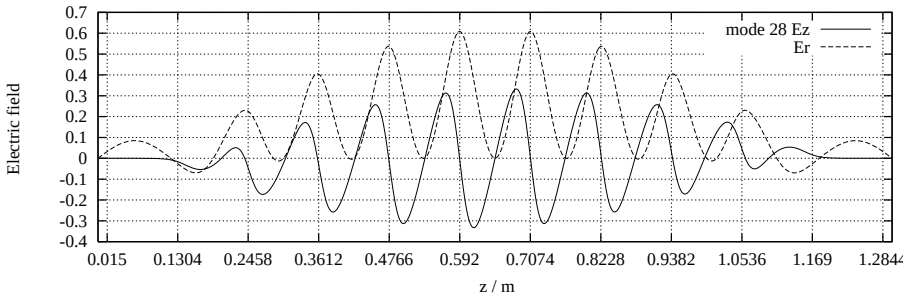

Figure 168: Electric field ($3 \cdot E_z$ and E_r) at $r = 1$ cm versus z of mode: EE-28

B.2.4 Beam pipe modes

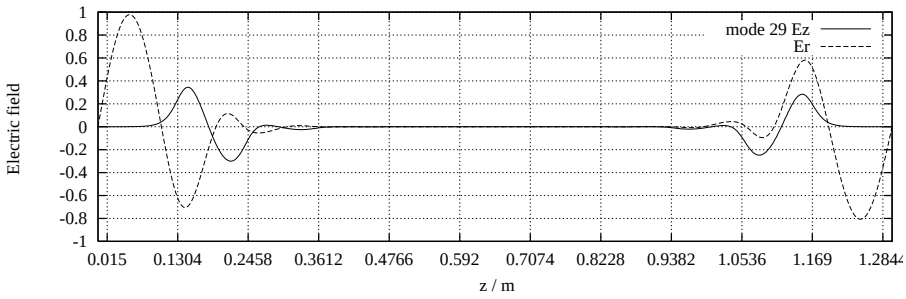

Figure 169: Electric field ($3 \cdot E_z$ and E_r) at $r = 1$ cm versus z of mode: EE-29

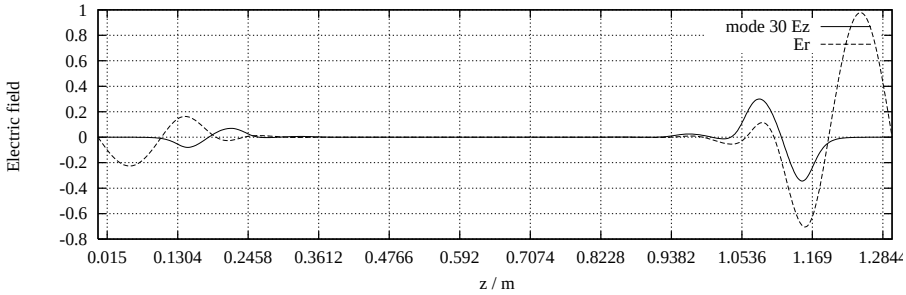

Figure 170: Electric field ($3 \cdot E_z$ and E_r) at $r = 1$ cm versus z of mode: EE-30

B.2.5 Band 4

Only the first and the last modes of the band is shown

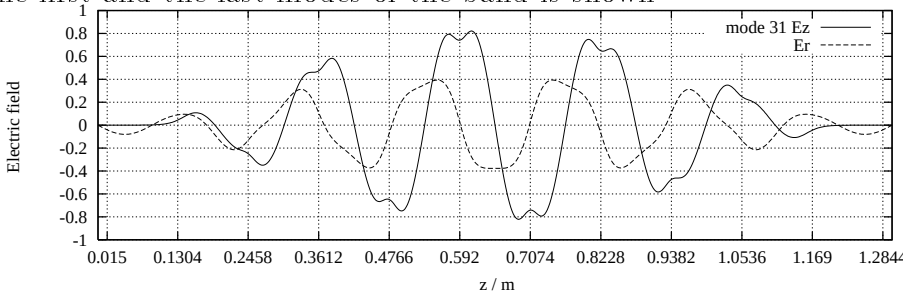

Figure 171: Electric field ($3 \cdot E_z$ and E_r) at $r = 1$ cm versus z of mode: EE-31

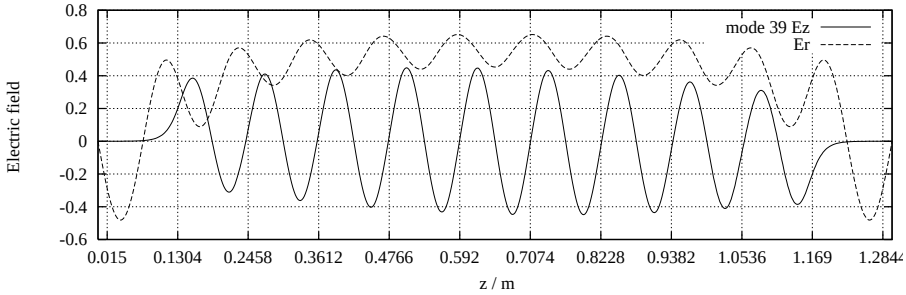

Figure 172: Electric field ($3 \cdot E_z$ and E_r) at $r = 1$ cm versus z of mode: EE-39

B.2.6 Band 5

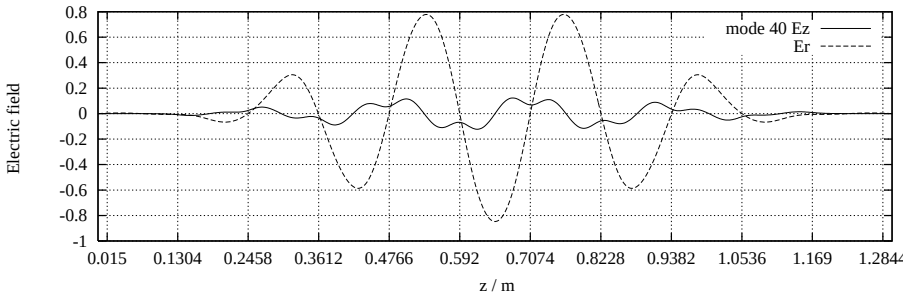

Figure 173: Electric field ($3 \cdot E_z$ and E_r) at $r = 1$ cm versus z of mode: EE-40

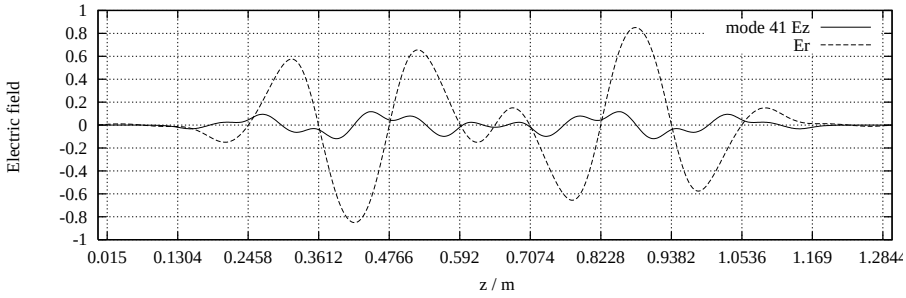

Figure 174: Electric field ($3 \cdot E_z$ and E_r) at $r = 1$ cm versus z of mode: EE-41

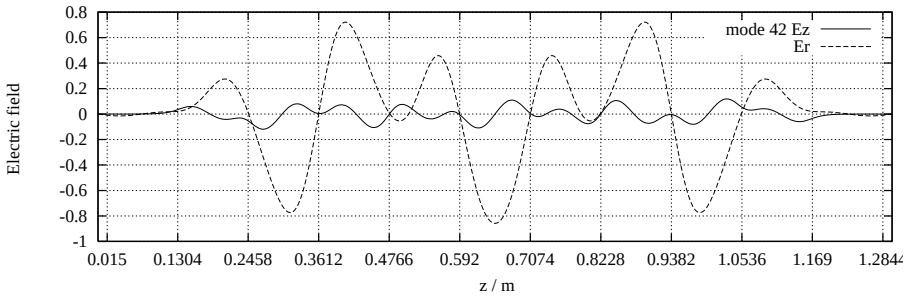

Figure 175: Electric field ($3 \cdot E_z$ and E_r) at $r = 1$ cm versus z of mode: EE-42

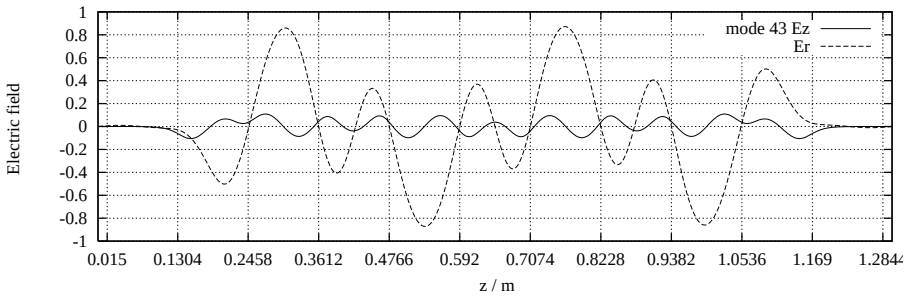

Figure 176: Electric field ($3 \cdot E_z$ and E_r) at $r = 1$ cm versus z of mode: EE-43

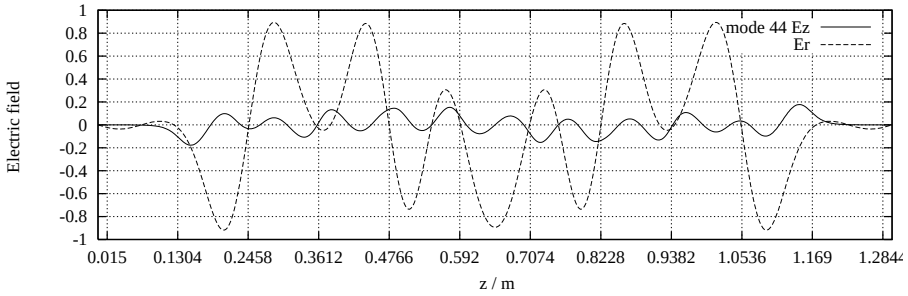

Figure 177: Electric field ($3 \cdot E_z$ and E_r) at $r = 1$ cm versus z of mode: EE-44

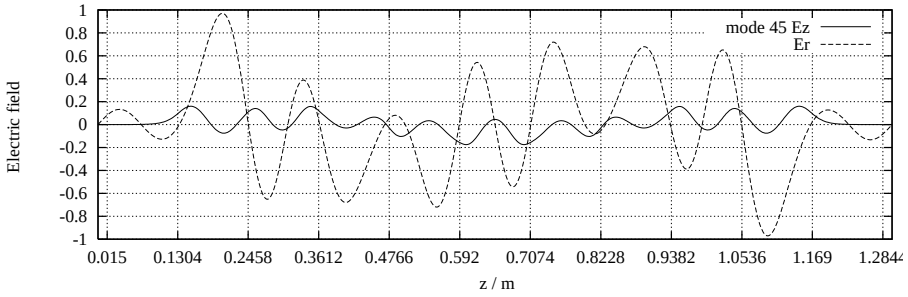

Figure 178: Electric field ($3 \cdot E_z$ and E_r) at $r = 1$ cm versus z of mode: EE-45

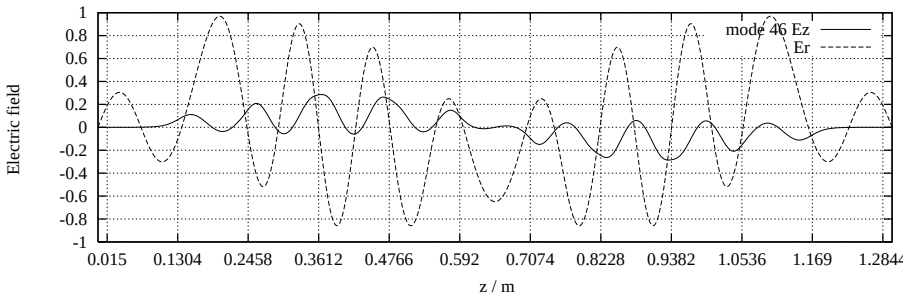

Figure 179: Electric field ($3 \cdot E_z$ and E_r) at $r = 1$ cm versus z of mode: EE-46

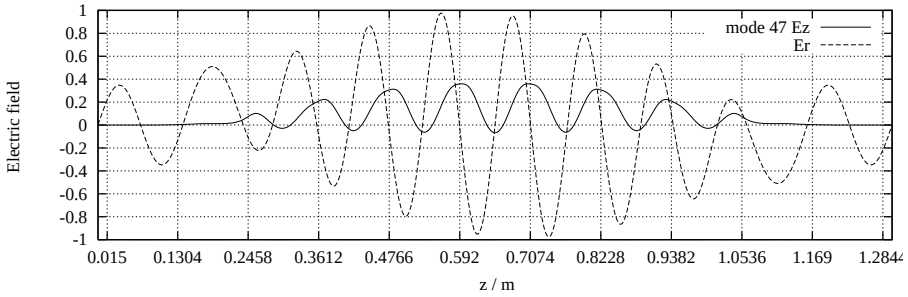

Figure 180: Electric field ($3 \cdot E_z$ and E_r) at $r = 1$ cm versus z of mode: EE-47

B.2.7 Beam pipe modes

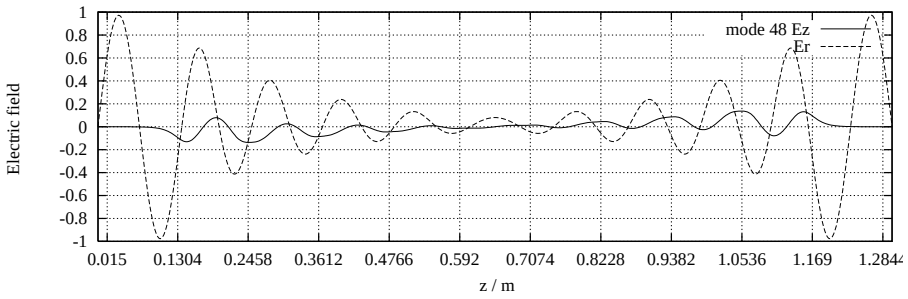

Figure 181: Electric field ($3 \cdot E_z$ and E_r) at $r = 1$ cm versus z of mode: EE-48

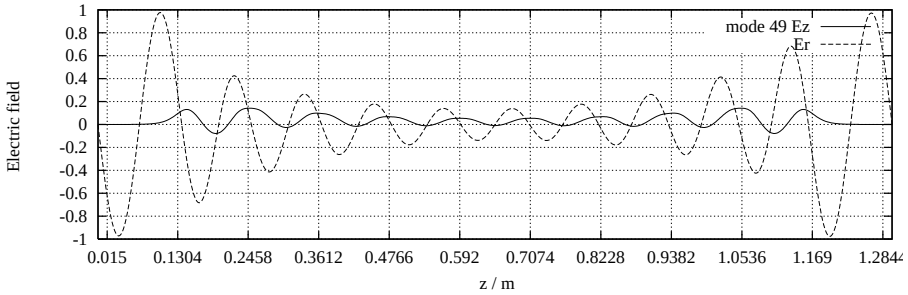

Figure 182: Electric field ($3 \cdot E_z$ and E_r) at $r = 1$ cm versus z of mode: EE-49

B.2.8 Band 6 and modes from higher passbands

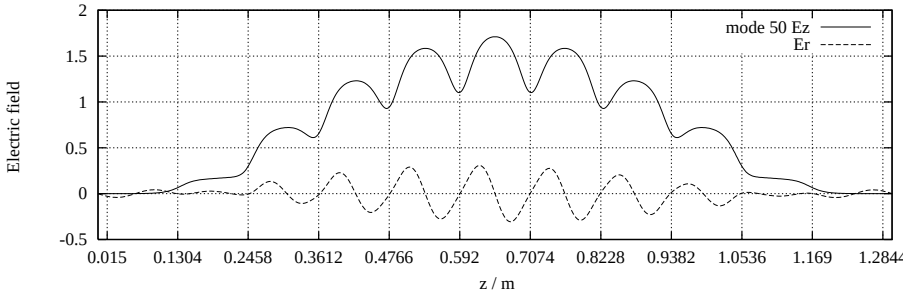

Figure 183: Electric field ($3 \cdot E_z$ and E_r) at $r = 1$ cm versus z of mode: EE-50

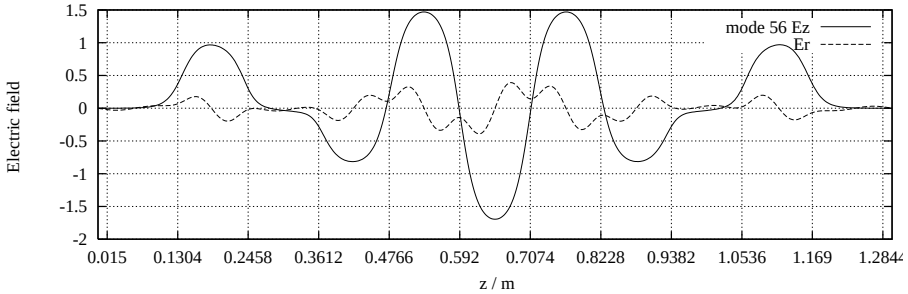

Figure 184: Electric field ($3 \cdot E_z$ and E_r) at $r = 1$ cm versus z of mode: EE-56

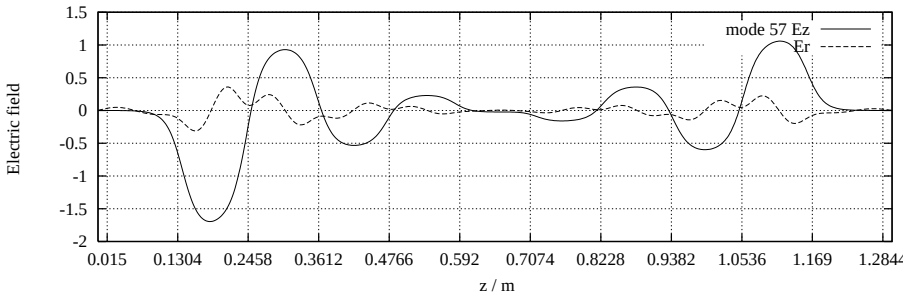

Figure 185: Electric field ($3 \cdot E_z$ and E_r) at $r = 1$ cm versus z of mode: EE-57

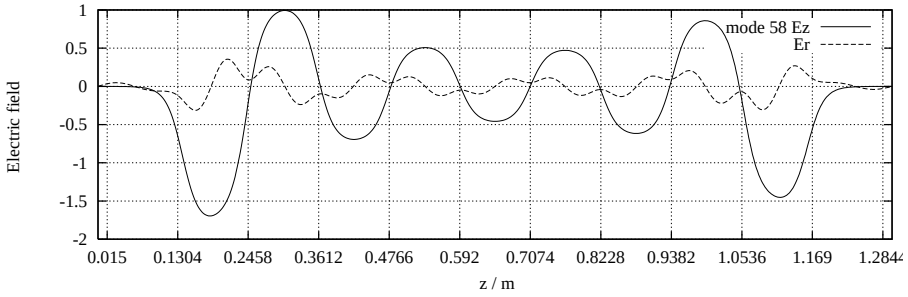

Figure 186: Electric field ($3 \cdot E_z$ and E_r) at $r = 1$ cm versus z of mode: EE-58

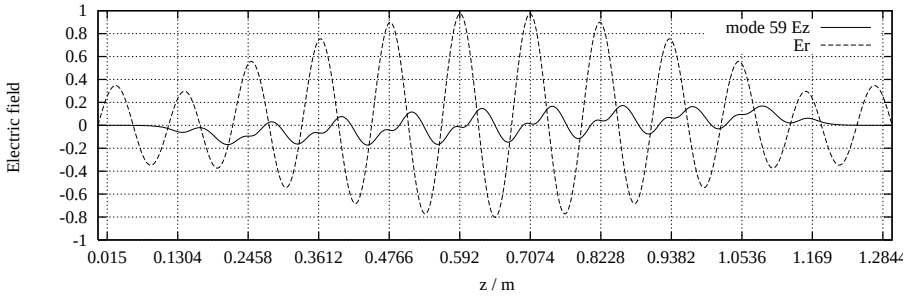

Figure 187: Electric field ($3 \cdot E_z$ and E_r) at $r = 1$ cm versus z of mode: EE-59

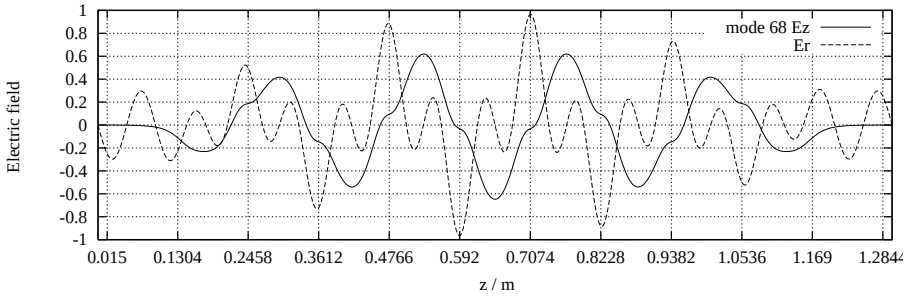

Figure 188: Electric field ($3 \cdot E_z$ and E_r) at $r = 1$ cm versus z of mode: EE-68

B.3 TTF-like TESLA 9-cell cavity, magnetic (MM) boundary conditions.

B.3.1 Beam pipe modes

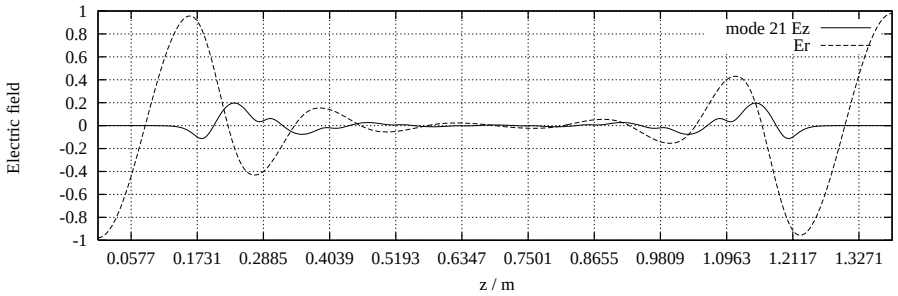

Figure 189: Electric field ($3 \cdot E_z$ and E_r) at $r = 1$ cm versus z of mode: EE-21

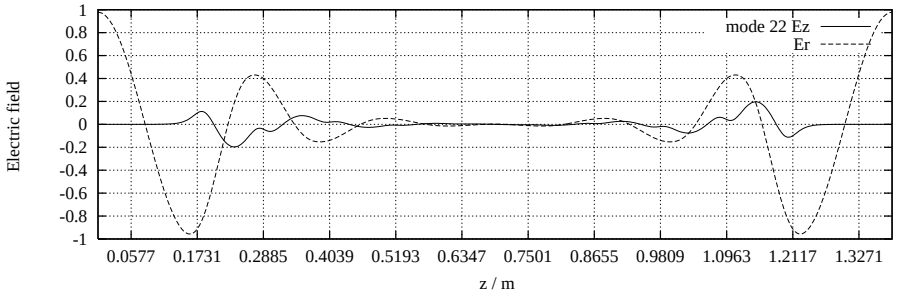

Figure 190: Electric field ($3 \cdot E_z$ and E_r) at $r = 1$ cm versus z of mode: EE-22

B.3.2 Band 3

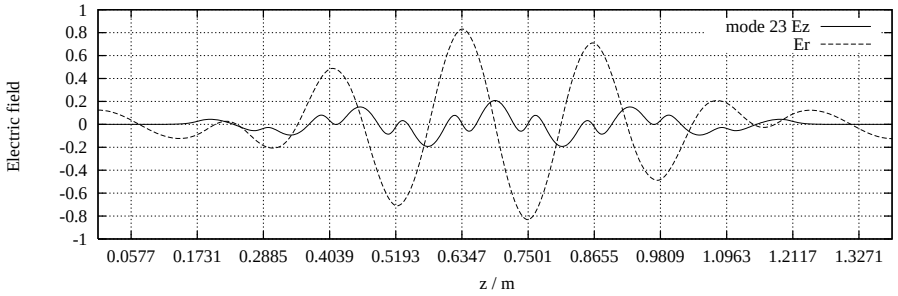

Figure 191: Electric field ($3 \cdot E_z$ and E_r) at $r = 1$ cm versus z of mode: EE-23

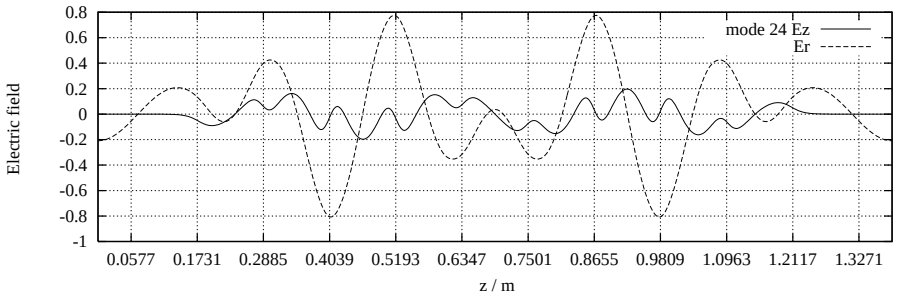

Figure 192: Electric field ($3 \cdot E_z$ and E_r) at $r = 1$ cm versus z of mode: EE-24

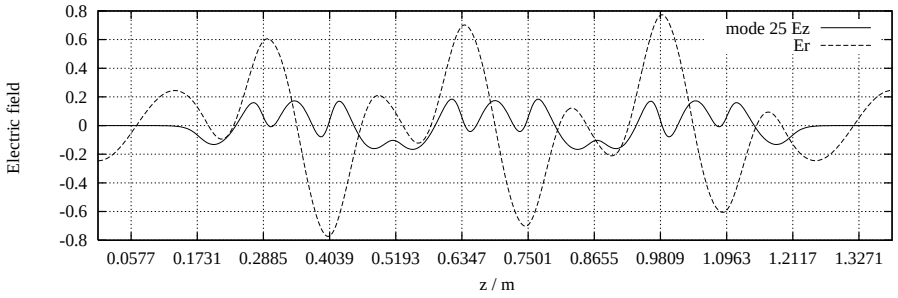

Figure 193: Electric field ($3 \cdot E_z$ and E_r) at $r = 1$ cm versus z of mode: EE-25

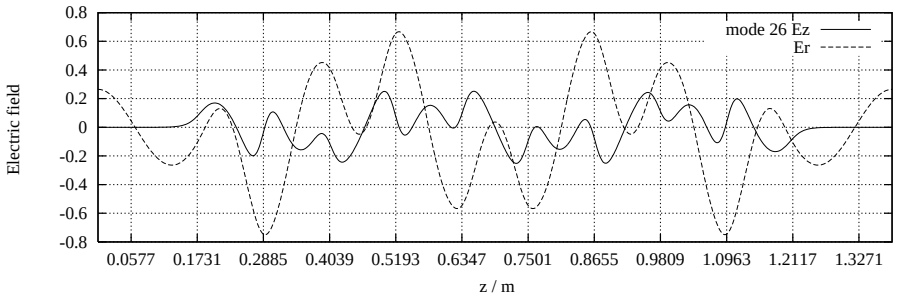

Figure 194: Electric field ($3 \cdot E_z$ and E_r) at $r = 1$ cm versus z of mode: EE-26

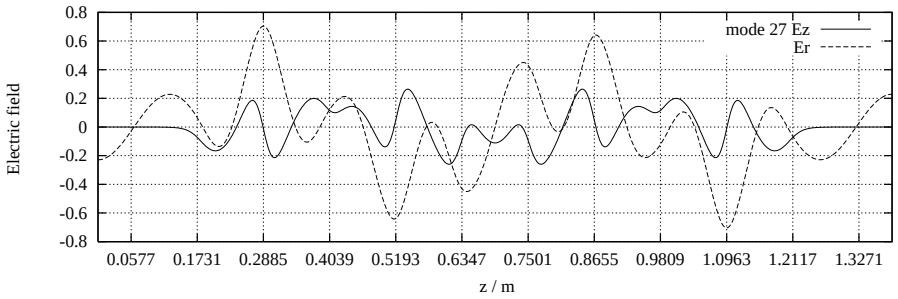

Figure 195: Electric field ($3 \cdot E_z$ and E_r) at $r = 1$ cm versus z of mode: EE-27

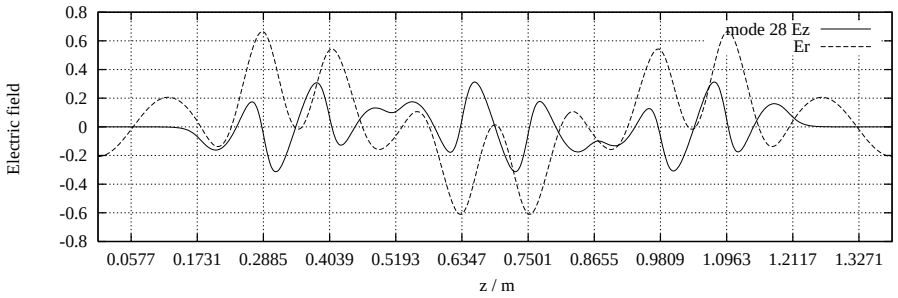

Figure 196: Electric field ($3 \cdot E_z$ and E_r) at $r = 1$ cm versus z of mode: EE-28

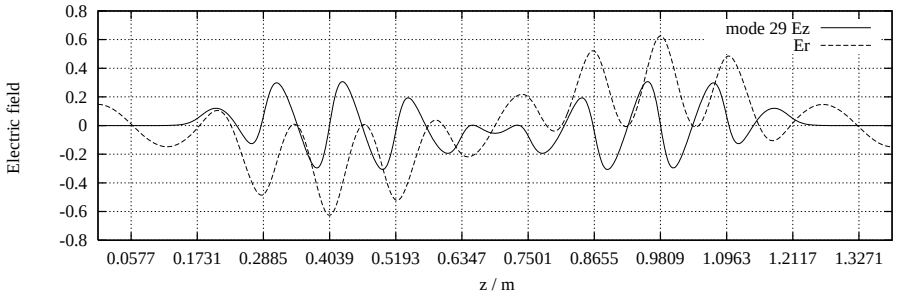

Figure 197: Electric field ($3 \cdot E_z$ and E_r) at $r = 1$ cm versus z of mode: EE-29

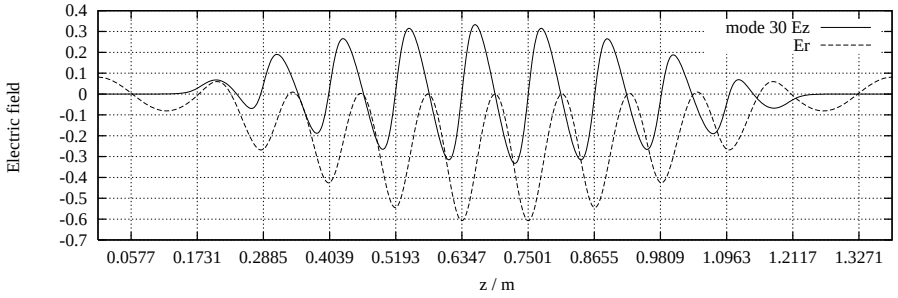

Figure 198: Electric field ($3 \cdot E_z$ and E_r) at $r = 1$ cm versus z of mode: EE-30

B.3.3 Band 5

Only four modes of the passband 5 are shown here: the first and the last modes of the passband, the trapped mode with the highest frequency and the mode with the lowest frequency which is just not trapped.

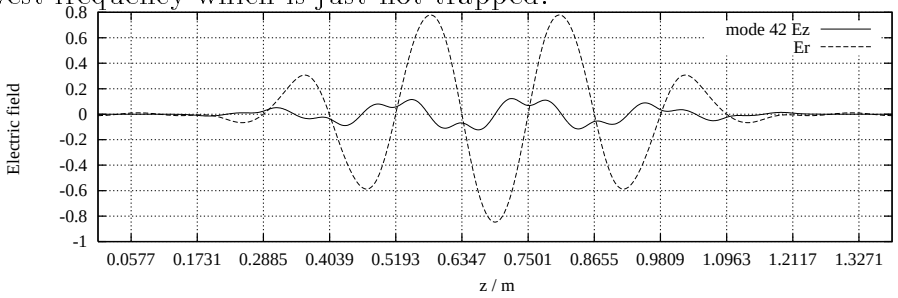

Figure 199: Electric field ($3 \cdot E_z$ and E_r) at $r = 1$ cm versus z of mode: EE-42

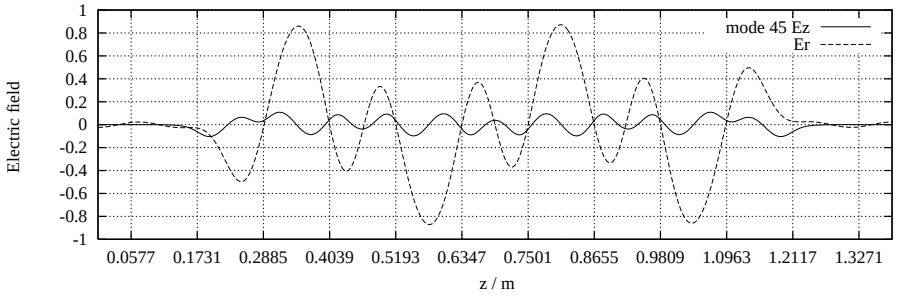

Figure 200: Electric field ($3 \cdot E_z$ and E_r) at $r = 1$ cm versus z of mode: EE-45

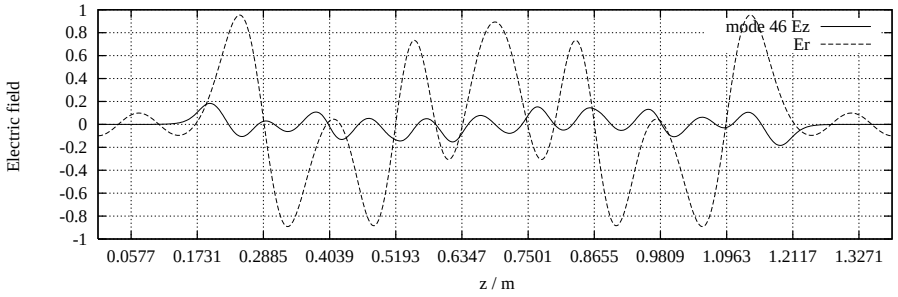

Figure 201: Electric field ($3 \cdot E_z$ and E_r) at $r = 1$ cm versus z of mode: EE-46

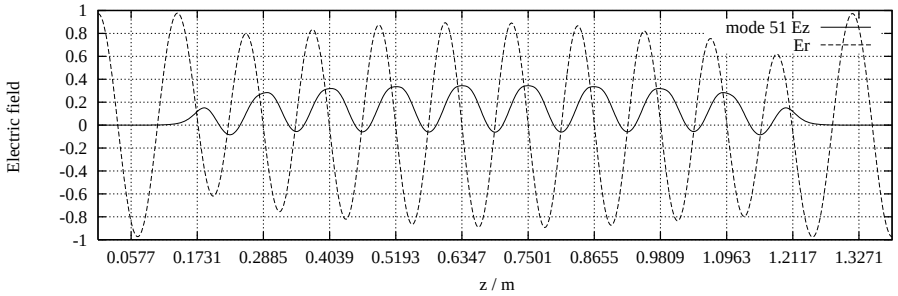

Figure 202: Electric field ($3 \cdot E_z$ and E_r) at $r = 1$ cm versus z of mode: EE-51

B.4 TTF-like TESLA 9-cell cavity, electric (EE) boundary conditions.

B.4.1 Band 3

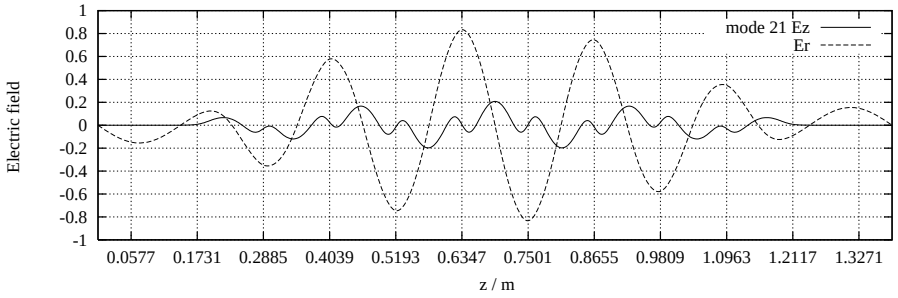

Figure 203: Electric field ($3 \cdot E_z$ and E_r) at $r = 1$ cm versus z of mode: EE-21

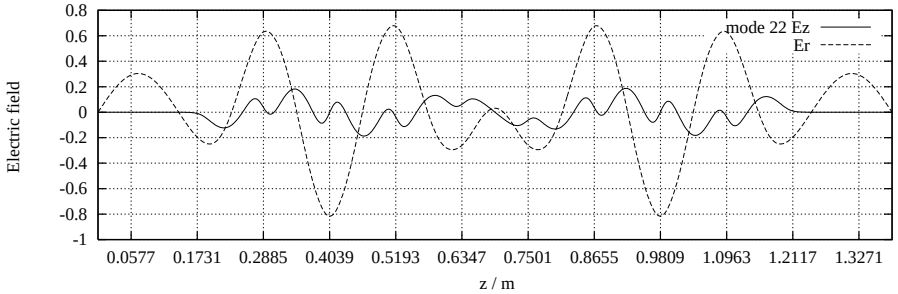

Figure 204: Electric field ($3 \cdot E_z$ and E_r) at $r = 1$ cm versus z of mode: EE-22

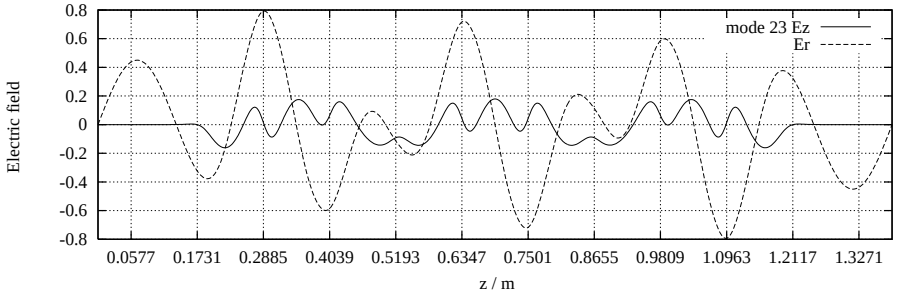

Figure 205: Electric field ($3 \cdot E_z$ and E_r) at $r = 1$ cm versus z of mode: EE-23

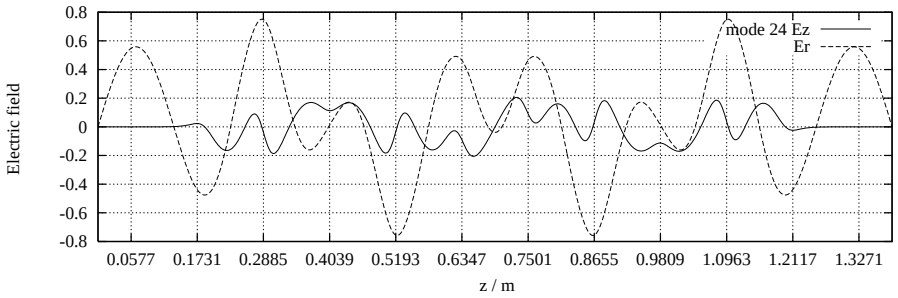

Figure 206: Electric field ($3 \cdot E_z$ and E_r) at $r = 1$ cm versus z of mode: EE-24

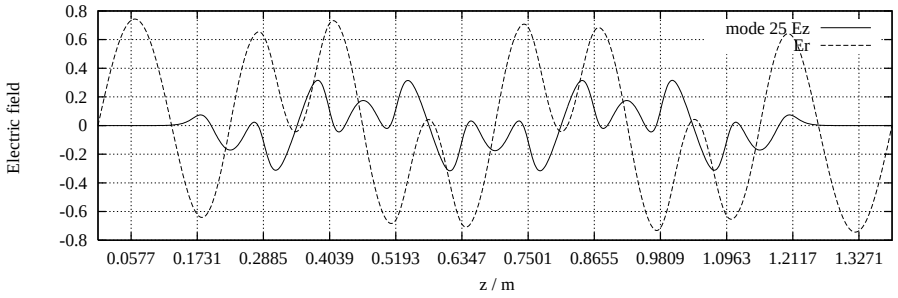

Figure 207: Electric field ($3 \cdot E_z$ and E_r) at $r = 1$ cm versus z of mode: EE-25

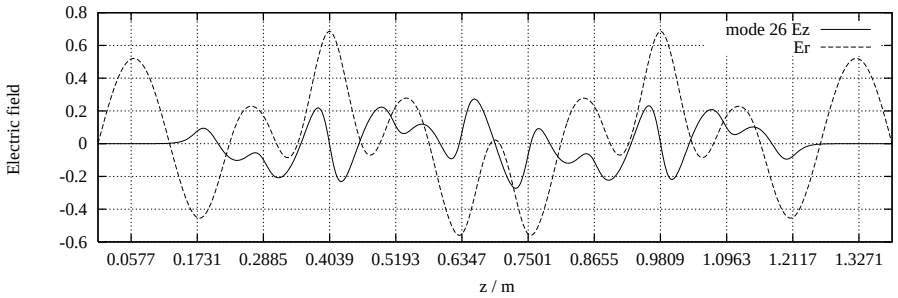

Figure 208: Electric field ($3 \cdot E_z$ and E_r) at $r = 1$ cm versus z of mode: EE-26

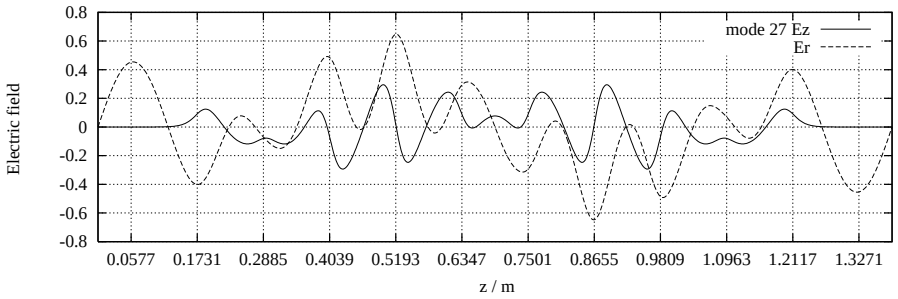

Figure 209: Electric field ($3 \cdot E_z$ and E_r) at $r = 1$ cm versus z of mode: EE-27

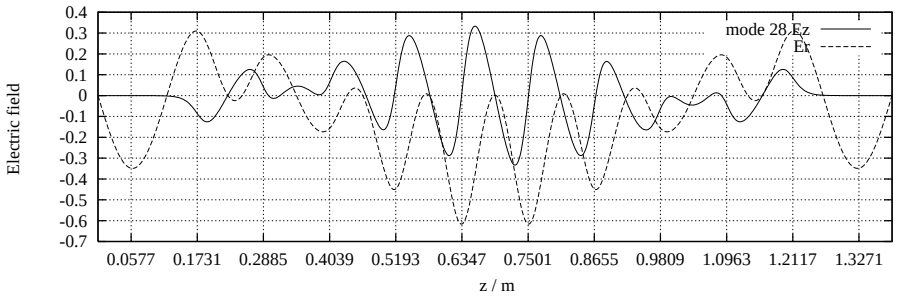

Figure 210: Electric field ($3 \cdot E_z$ and E_r) at $r = 1$ cm versus z of mode: EE-28

B.4.2 Beam pipe modes

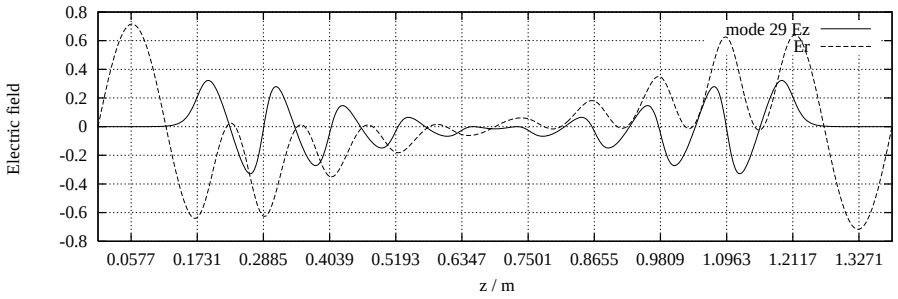

Figure 211: Electric field ($3 \cdot E_z$ and E_r) at $r = 1$ cm versus z of mode: EE-29

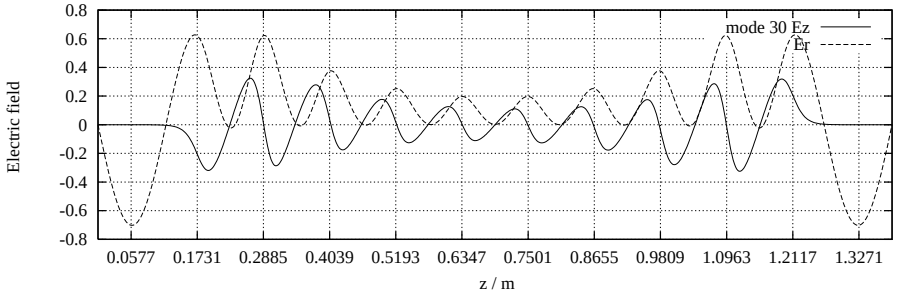

Figure 212: Electric field ($3 \cdot E_z$ and E_r) at $r = 1$ cm versus z of mode: EE-30

C Electric fields of quadrupole modes

C.1 TDR-like TESLA 9-cell cavity, magnetic (MM) boundary conditions.

C.1.1 Band 1

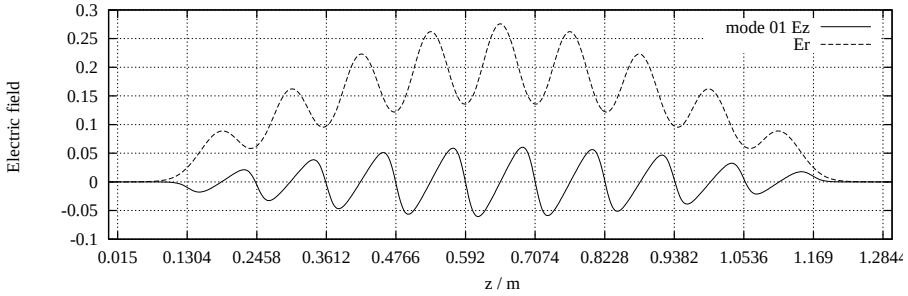

Figure 213: Electric field ($3 \cdot E_z$ and E_r) at $r = 1$ cm versus z of mode: MM-01

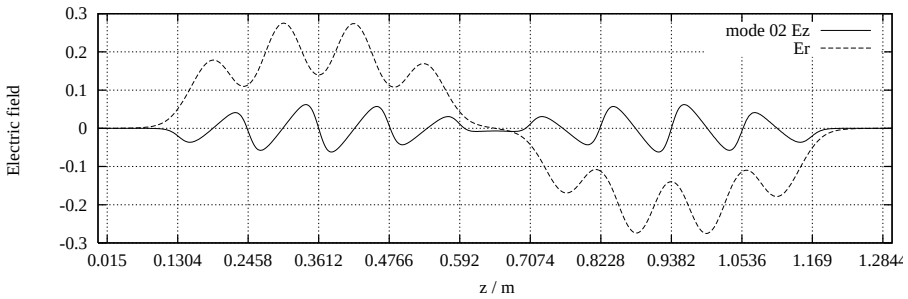

Figure 214: Electric field ($3 \cdot E_z$ and E_r) at $r = 1$ cm versus z of mode: MM-02

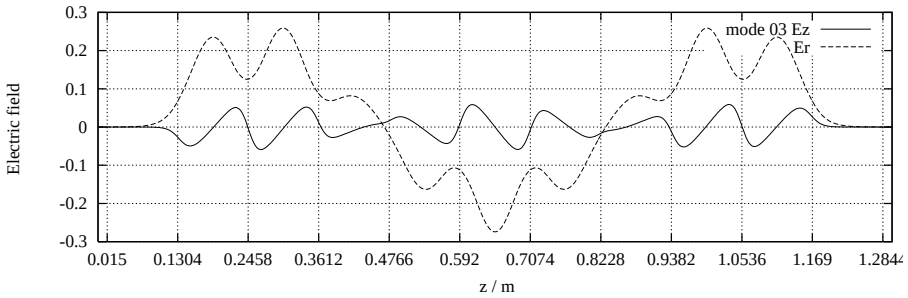

Figure 215: Electric field ($3 \cdot E_z$ and E_r) at $r = 1$ cm versus z of mode: MM-03

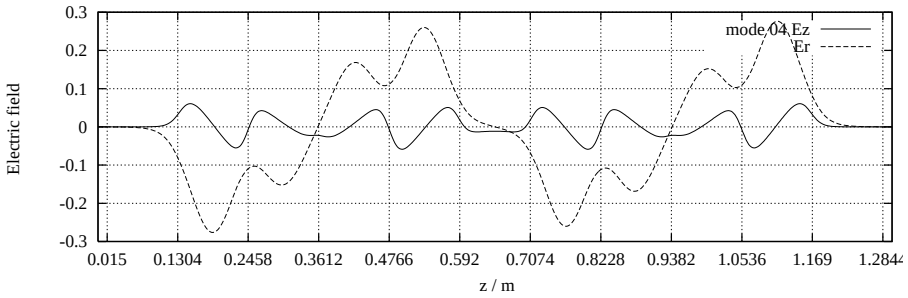

Figure 216: Electric field ($3 \cdot E_z$ and E_r) at $r = 1$ cm versus z of mode: MM-04

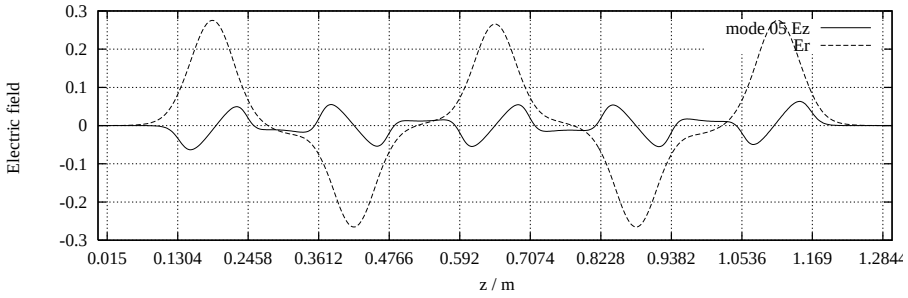

Figure 217: Electric field ($3 \cdot E_z$ and E_r) at $r = 1$ cm versus z of mode: MM-05

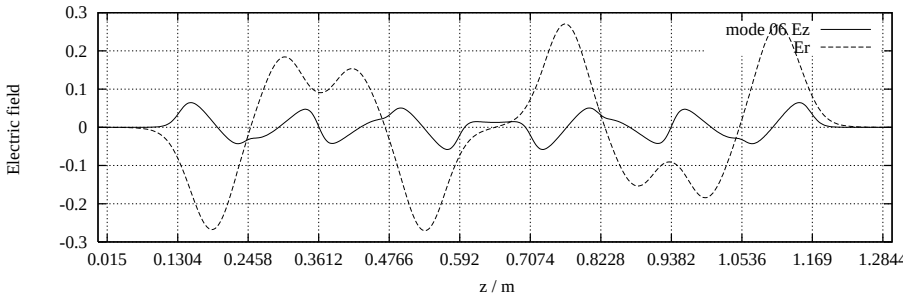

Figure 218: Electric field ($3 \cdot E_z$ and E_r) at $r = 1$ cm versus z of mode: MM-06

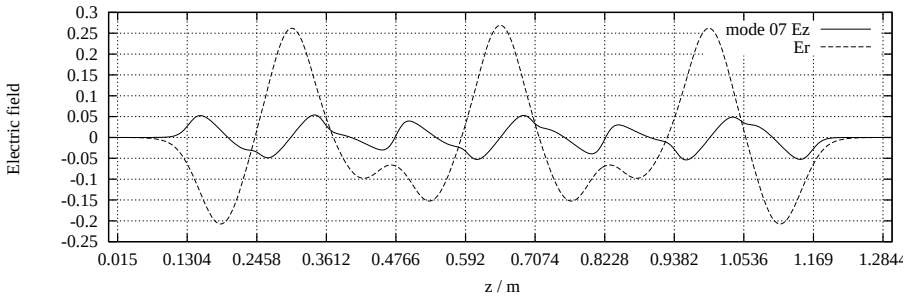

Figure 219: Electric field ($3 \cdot E_z$ and E_r) at $r = 1$ cm versus z of mode: MM-07

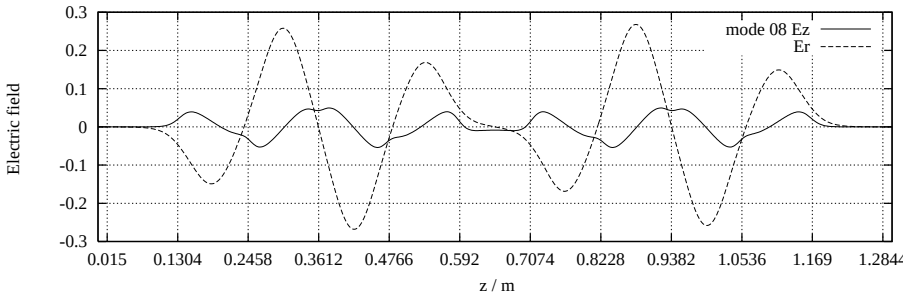

Figure 220: Electric field ($3 \cdot E_z$ and E_r) at $r = 1$ cm versus z of mode: MM-08

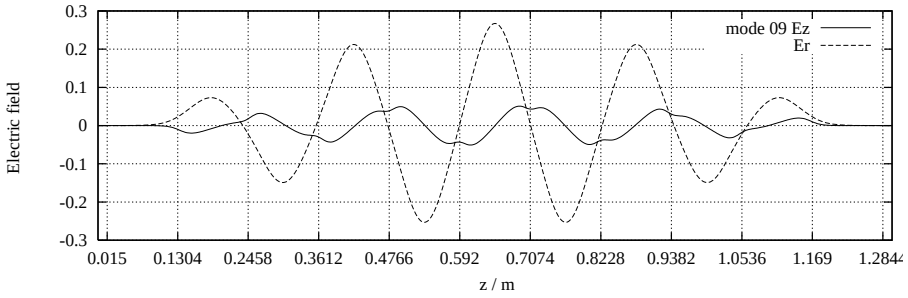

Figure 221: Electric field ($3 \cdot E_z$ and E_r) at $r = 1$ cm versus z of mode: MM-09

C.1.2 Band 2

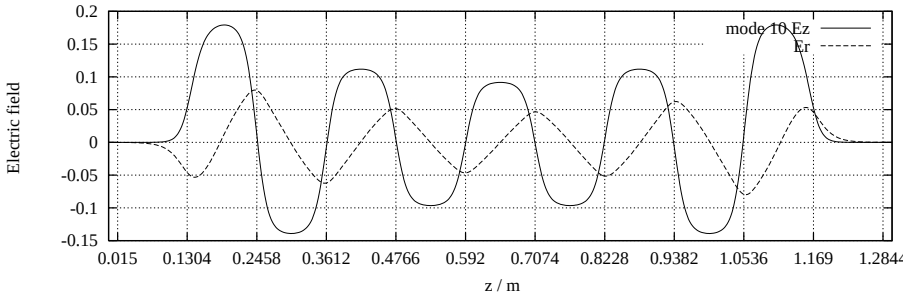

Figure 222: Electric field ($3 \cdot E_z$ and E_r) at $r = 1$ cm versus z of mode: MM-10

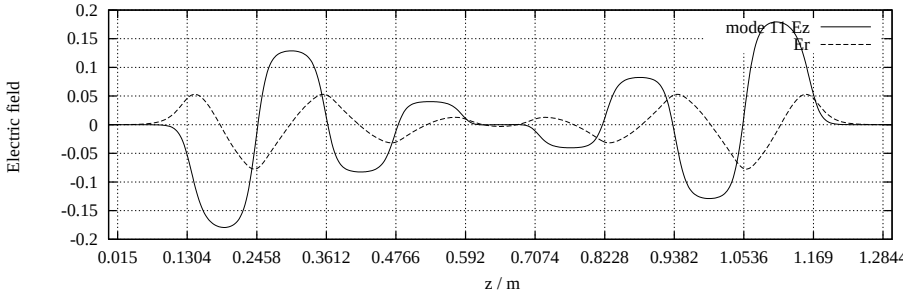

Figure 223: Electric field ($3 \cdot E_z$ and E_r) at $r = 1$ cm versus z of mode: MM-11

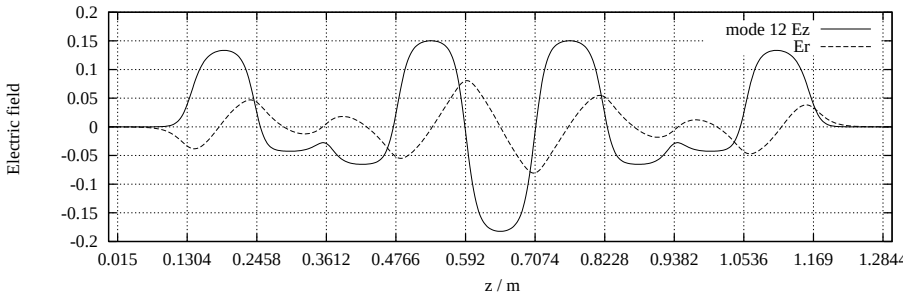

Figure 224: Electric field ($3 \cdot E_z$ and E_r) at $r = 1$ cm versus z of mode: MM-12

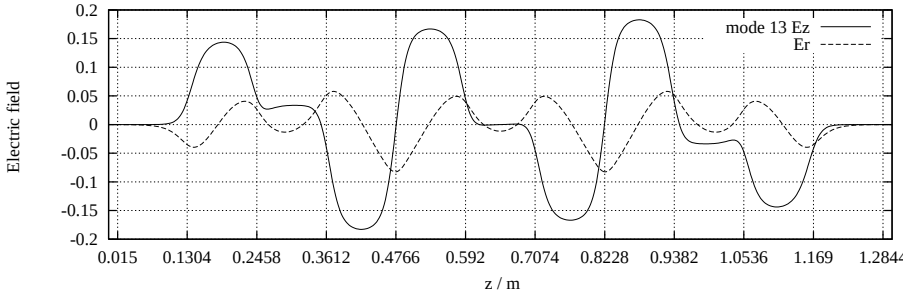

Figure 225: Electric field ($3 \cdot E_z$ and E_r) at $r = 1$ cm versus z of mode: MM-13

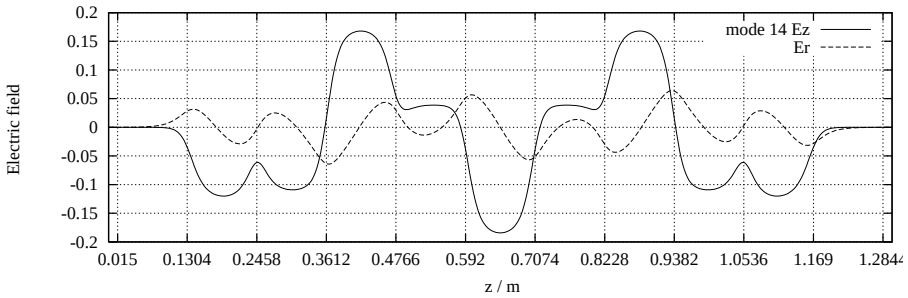

Figure 226: Electric field ($3 \cdot E_z$ and E_r) at $r = 1$ cm versus z of mode: MM-14

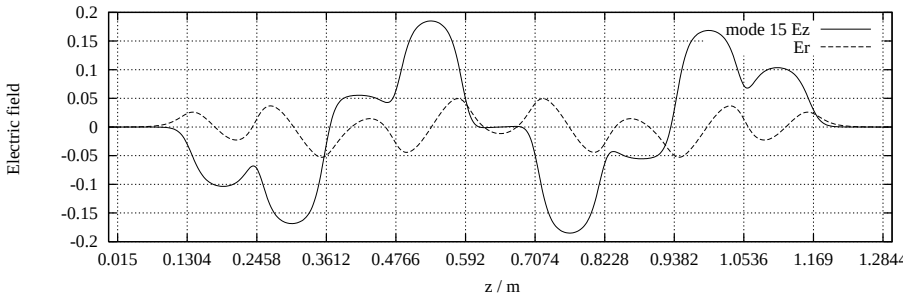

Figure 227: Electric field ($3 \cdot E_z$ and E_r) at $r = 1$ cm versus z of mode: MM-15

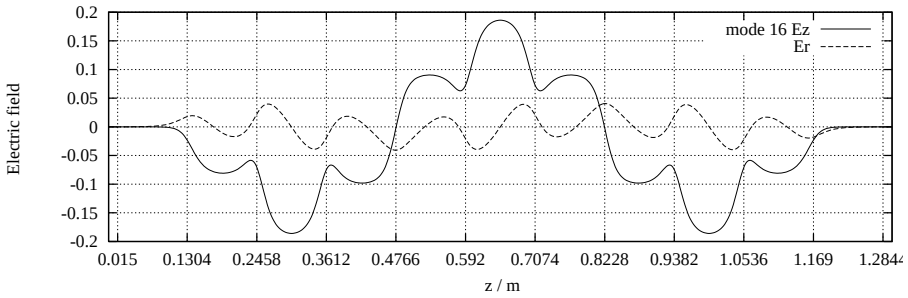

Figure 228: Electric field ($3 \cdot E_z$ and E_r) at $r = 1$ cm versus z of mode: MM-16

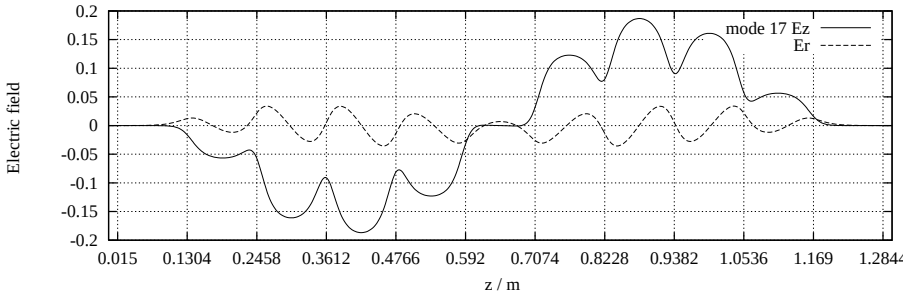

Figure 229: Electric field ($3 \cdot E_z$ and E_r) at $r = 1$ cm versus z of mode: MM-17

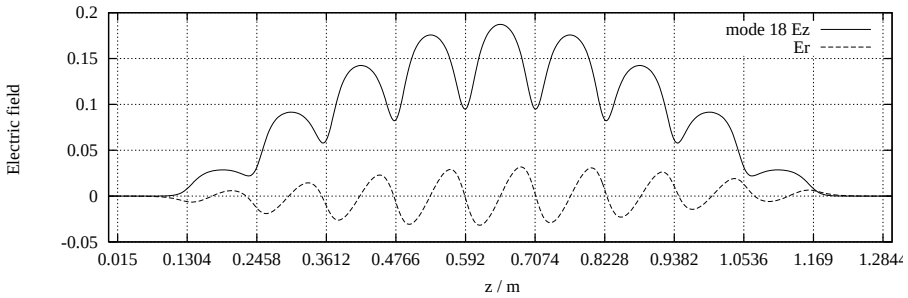

Figure 230: Electric field ($3 \cdot E_z$ and E_r) at $r = 1$ cm versus z of mode: MM-18

C.1.3 Band 3

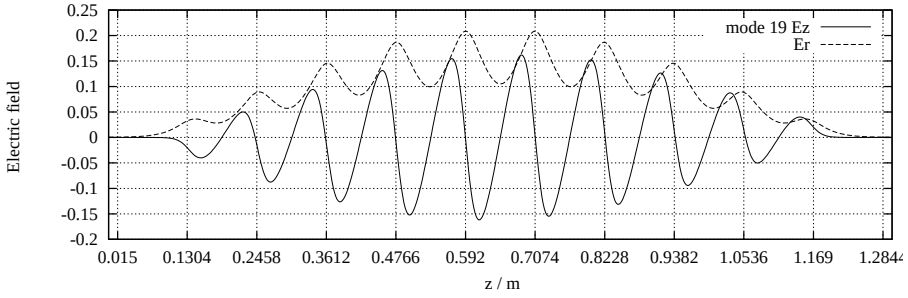

Figure 231: Electric field ($3 \cdot E_z$ and E_r) at $r = 1$ cm versus z of mode: MM-19

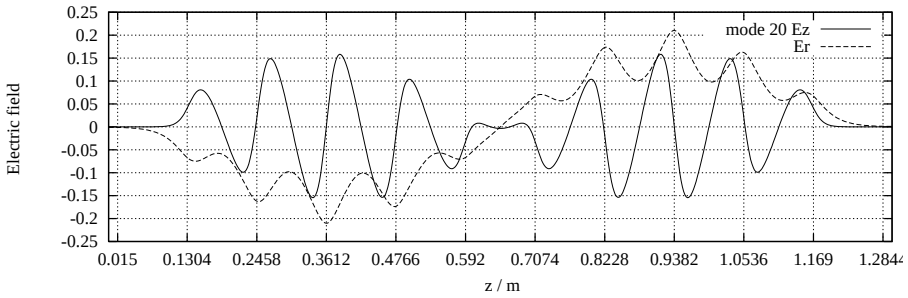

Figure 232: Electric field ($3 \cdot E_z$ and E_r) at $r = 1$ cm versus z of mode: MM-20

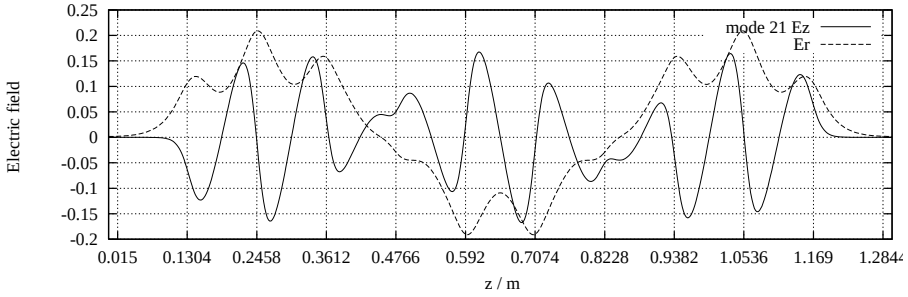

Figure 233: Electric field ($3 \cdot E_z$ and E_r) at $r = 1$ cm versus z of mode: MM-21

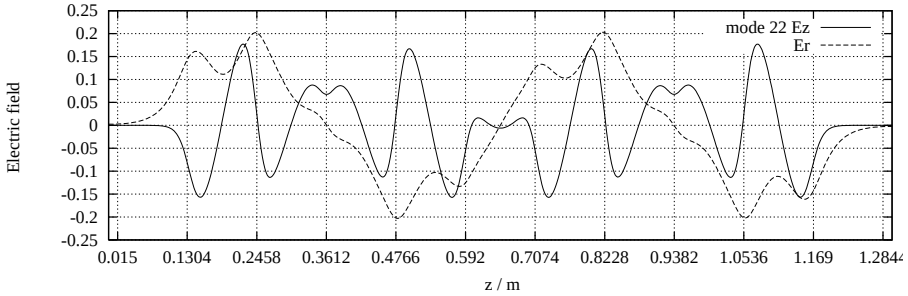

Figure 234: Electric field ($3 \cdot E_z$ and E_r) at $r = 1$ cm versus z of mode: MM-22

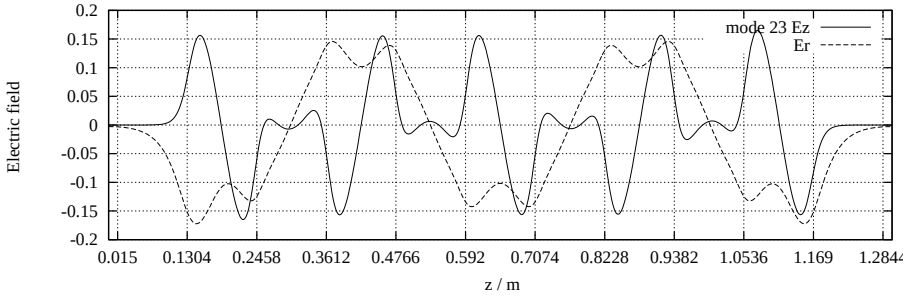

Figure 235: Electric field ($3 \cdot E_z$ and E_r) at $r = 1$ cm versus z of mode: MM-23

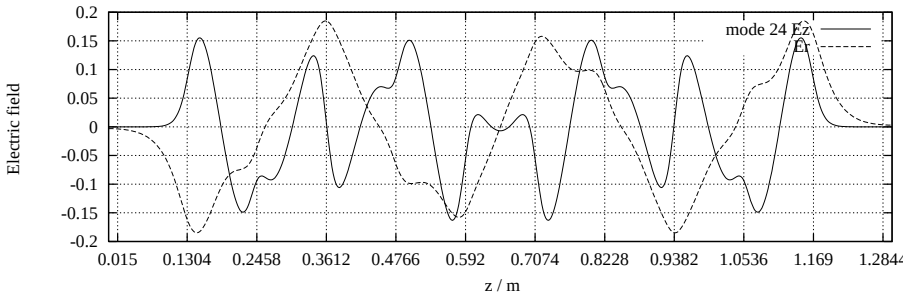

Figure 236: Electric field ($3 \cdot E_z$ and E_r) at $r = 1$ cm versus z of mode: MM-24

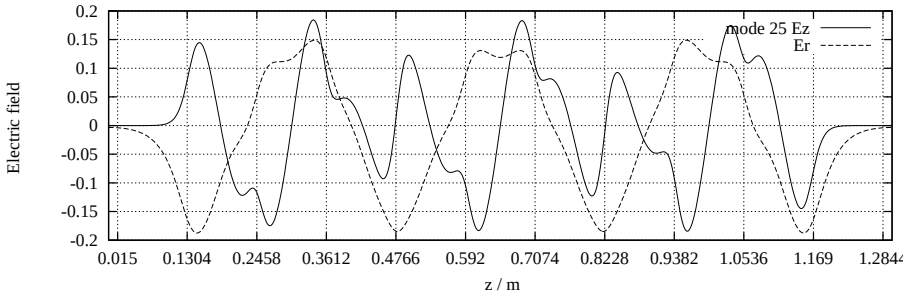

Figure 237: Electric field ($3 \cdot E_z$ and E_r) at $r = 1$ cm versus z of mode: MM-25

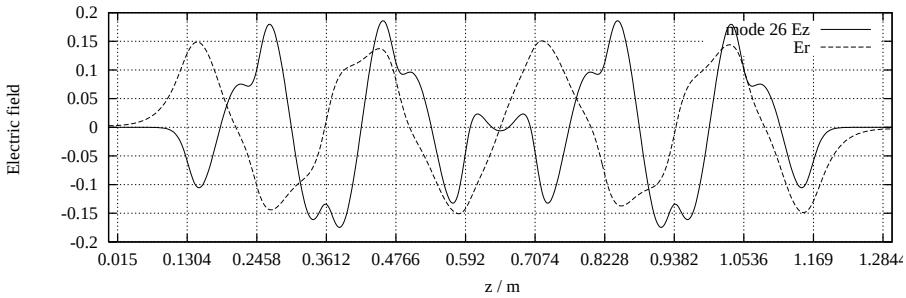

Figure 238: Electric field ($3 \cdot E_z$ and E_r) at $r = 1$ cm versus z of mode: MM-26

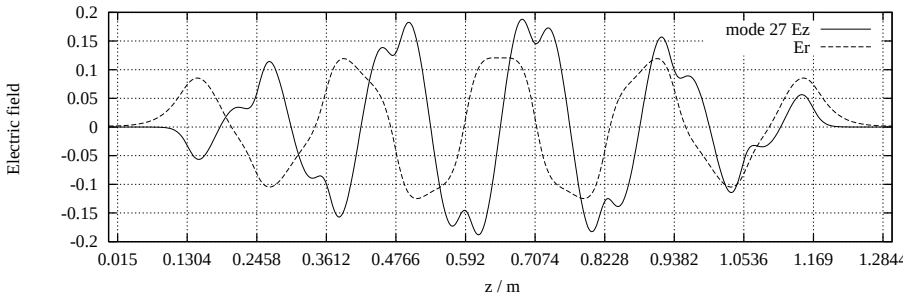

Figure 239: Electric field ($3 \cdot E_z$ and E_r) at $r = 1$ cm versus z of mode: MM-27

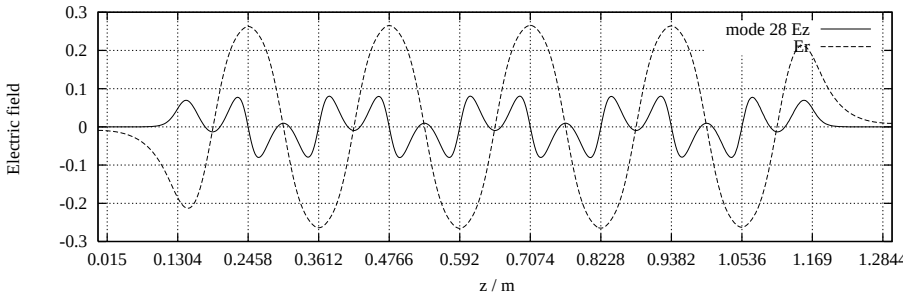

Figure 240: Electric field ($3 \cdot E_z$ and E_r) at $r = 1$ cm versus z of mode: MM-28

C.1.4 Band 4

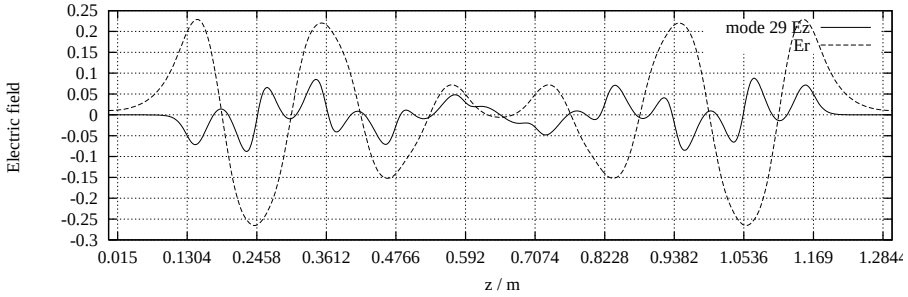

Figure 241: Electric field ($3 \cdot E_z$ and E_r) at $r = 1$ cm versus z of mode: MM-29

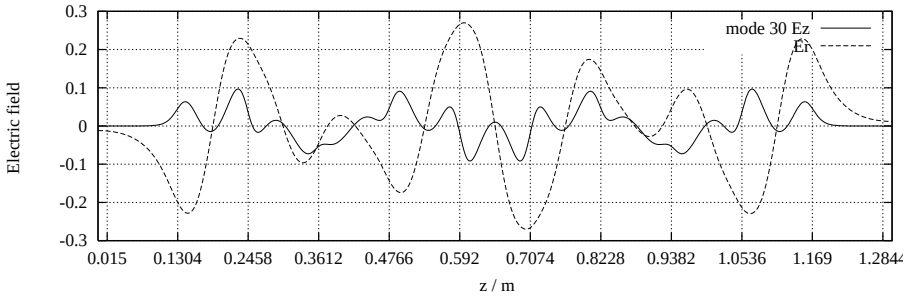

Figure 242: Electric field ($3 \cdot E_z$ and E_r) at $r = 1$ cm versus z of mode: MM-30

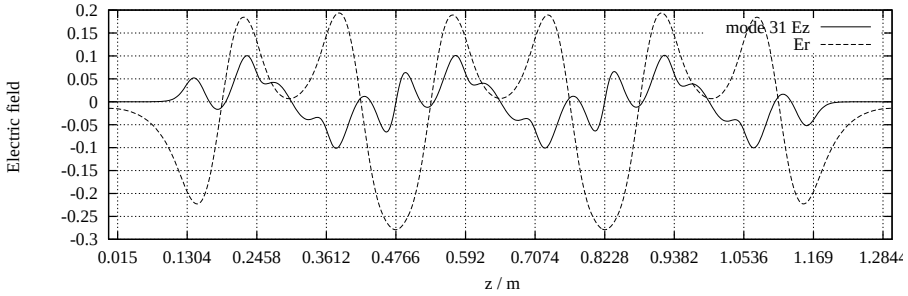

Figure 243: Electric field ($3 \cdot E_z$ and E_r) at $r = 1$ cm versus z of mode: MM-31

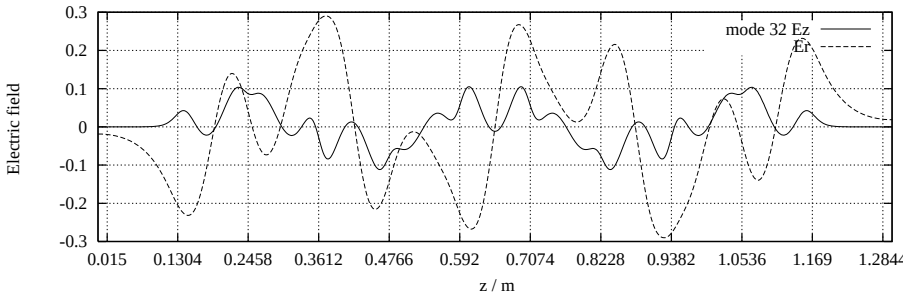

Figure 244: Electric field ($3 \cdot E_z$ and E_r) at $r = 1$ cm versus z of mode: MM-32

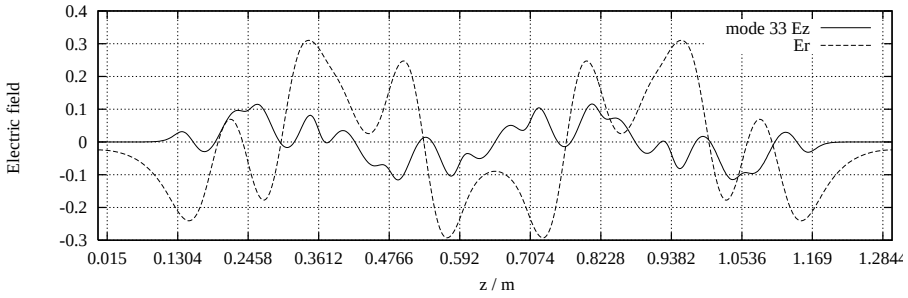

Figure 245: Electric field ($3 \cdot E_z$ and E_r) at $r = 1$ cm versus z of mode: MM-33

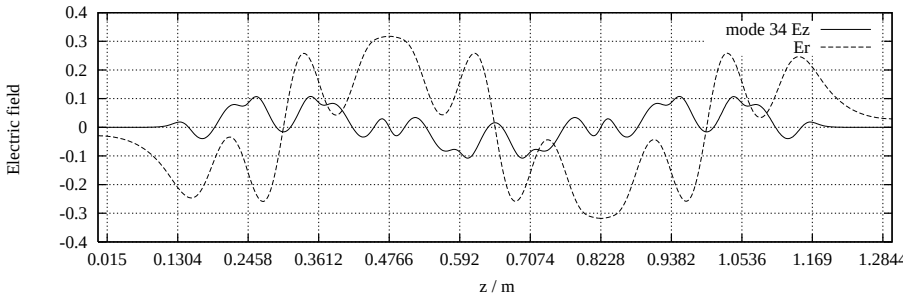

Figure 246: Electric field ($3 \cdot E_z$ and E_r) at $r = 1$ cm versus z of mode: MM-34

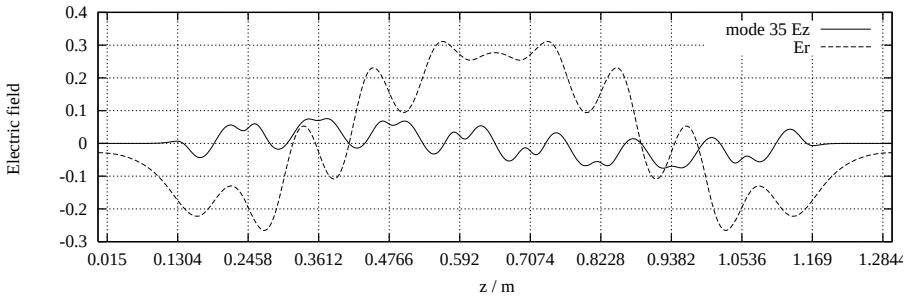

Figure 247: Electric field ($3 \cdot E_z$ and E_r) at $r = 1$ cm versus z of mode: MM-35

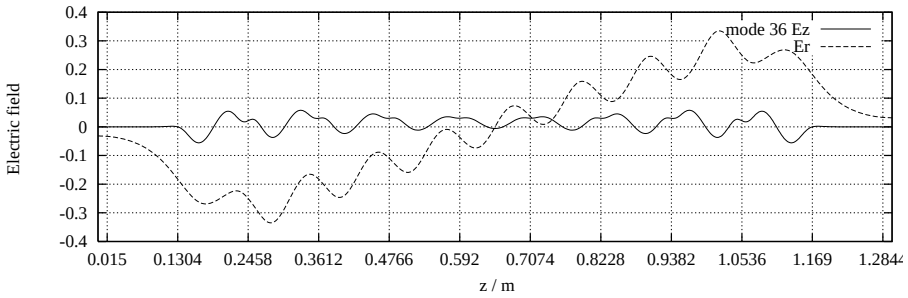

Figure 248: Electric field ($3 \cdot E_z$ and E_r) at $r = 1$ cm versus z of mode: MM-36

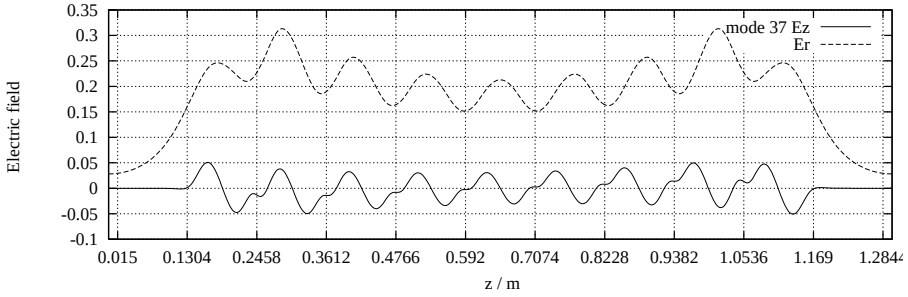

Figure 249: Electric field ($3 \cdot E_z$ and E_r) at $r = 1$ cm versus z of mode: MM-37